5-Axis Additive Manufacturing of Hydrogen Pressure Vessels

With Liquid Crystal Polymers

Berend A. van Leengoed

TU Delft

5-Axis Additive Manufacturing of Hydrogen Pressure Vessels

With Liquid Crystal Polymers

by

Berend A. van Leengoed

to obtain the degree of Master of Science
at the Delft University of Technology,
to be defended publicly on Tuesday July 19th, 2022 at 10:00

Student number: 4439147
Project duration: April, 2021 – June, 2022
Thesis committee:

Prof. Dr. K. Masania,	TU Delft Aerospace AMT, Chair, Daily Supervisor
Dr. B. Atli-Veltin,	TU Delft Aerospace AMT, Co-Supervisor
Prof. Dr. S.G.P. Castro,	TU Delft Aerospace ASCM, Examiner
Prof. Dr. C.D. Rans,	TU Delft Aerospace SI&C, Examiner

This thesis is confidential and cannot be made public until 19-01-2023

TU Delft

Preface

After seven years since I started my bachelor in Aerospace this thesis concludes my time as a student at the TU Delft. The last year working on my thesis has been very enjoyable, for which I would like to thank my supervisor Kunal Masania. You provided a perfect combination of freedom and guidance, allowing me to work efficiently on my own work but provide great insight and advice at just the right time.

Furthermore I would like to thank everyone from the Shaping Matter Lab, without everyone in the team creating such a nice atmosphere to work in, this thesis would not have been what it is today. Nick thanks for introducing me to our good friend Escher, this resulted in a fast running start working with the printer. Thanks Kevin, Ranjan, Lars, Caroline, Vinay, Muhamad, Satya, Sungi, Shashank and everyone else who were in the lab to make babysitting Escher more enjoyable. Furthermore, special thanks to everyone in the LCP team, with whom we had an excellent platform for discussion and problem solving. This also included the great team from NematX, without your help I would not have come as far with printing on the 5 axis printer. I also received great support from the technicians at DASML and TNO, who helped me with my equipment and experiments, for which .

Finally I would like to thank all my friends and family for the great support throughout my studies, especially when I was most preoccupied.

Berend A. van Leengoed
Delft, June 2022

Abstract

In the coming decades the aviation industry, among many others, will be undergoing a massive shift towards cleaner fuel or energy sources. One part in this transition is the use of hydrogen as a fuel source or energy carrier aboard an aircraft or other type of vehicle. To store gaseous hydrogen traditionally, in the aerospace sector, lightweight solutions are used for this to maximise the vehicle's efficiency. Even though gaseous hydrogen has a high energy density, its volumetric density is very low. To counteract this inefficient use of volume, it is commonly stored at 350 or 900 times atmospheric pressure. A state of the art lightweight solutions that can withstand these kind of pressures is the Composite Overwrapped Pressure Vessel (COPV), a cylindrical pressure vessel. Which consists of a composite laminate, usually with high strength carbon fibres, overwrapped on a liner, which is used to impose the internal geometry of the vessel during its manufacturing, and provide a barrier between the stored gas and the composite material. Due to constraints in manufacturing these vessels they are limited to axisymmetric geometries. Placing such cylindrical vessels in any vehicle results in a low packing density that should be further optimised, especially when using hydrogen with its low volumetric density.

This thesis will provide a new manufacturing method for creating pressure vessels. Using 5-axis additive manufacturing allows to step away from the manufacturing constraints imposed on traditional COPVs and furthermore opens up new possibilities in shaping freedom. In this work a 5-axis Fused Deposition Modelling (FDM) printer will be used to develop a one step process for printing pressure vessels. The material used with this manufacturing method are Liquid Crystal Polymers (LCP), when printed a highly anisotropic crystalline polymer that shows excellent hydrogen barrier properties as a bulk material. This high anisotropy, due to its crystalline micro-structure, results in excellent mechanical properties along the print line direction, which can be combined with structurally optimised designs to outperform classical composite laminate materials. Furthermore due to its thermoplastic nature an additively manufactured part can recycled. Something which is not possible at the end of life of a COPV. With this material showing excellent permeability and mechanical properties it can be used serving the roles of both the liner and the composite laminate in COPVs.

Even though the material has excellent bulk hydrogen permeability properties no data is currently available on the permeability of materials in an additively manufactured form. Especially with FDM print lines that fuse together to adjacent lines, the interface between these lines could serve as a zone of increased permeability. In order to asses this uncertainty specimens of LCP were manufactured and tested for hydrogen permeability. Six specimens of 2 mm thickness were printed and annealed, a heat treatment improving the chemical cross linking which unfortunately reduced recyclability, and ultimately tested in a hydrogen permeation setup at 300 bar. The permeability data resultant of these tests shows a small drop in performance compared to the bulk permeation properties, however these specimens outperform polymers, commonly used in liners of COPVs, by 1 to 2 orders of magnitude. Additionally one specimen without annealing was tested, showing a permeability within the same order of magnitude as the annealed specimens.

In order to manufacture pressure vessels with a 5-axis printer in a single process a number of printing sequences were developed. Starting with manufacturing a threaded cylinder as a base point, as well as serving as a pressure connector, followed by an internal wall to impose the geometry, similar to the liner of a COPV. Ultimately topped of by an outer wall that can be built up of layers of any orientation and thickness. A total of 15 cylindrical pressure vessels were eventually printed and loaded until failure with high pressure air to validate the printing procedures. With a wall thickness ranging between 0.8 and 1.2 mm these tanks reached pressures between 4 and 11,5 bar. The lower pressures obtained were related to failure modes governed by low printing quality and low inter-layer adhesion strength. Both of which can be improved in the future by increasing the printing quality monitoring and control and further optimisation of the printing process.

With this one step 5-axis additive manufacturing process using LCPs this thesis provides a springboard for future development of pressure vessels with non-conformal geometries, optimising the packing efficiency. As well as many different options for structural optimisation such as optimised variable angle print lines, stress field aligned print lines, or integrating internal structures such as LCP spun lines.

Contents

Acronyms

AM Additive Manufacturing. 2, 33, 36, 37, 42

ASTM American Society for Testing and Materials. 19

CAD Computer Aided Design. 40

CNC Computer Numerical Control. 37, 42

COPV Composite Overwrapped Pressure Vessels. xiii, 1, 2, 33, 77, 79

DASML Delft Aerospace Structures and Materials Laboratory. 64

FDM Fused Deposition Modelling. 2, 3, 11, 17, 18, 21, 26, 29, 31, 33, 37, 41, 45, 46, 56, 61, 65, 78, 81–84

LCP Liquid Crystal Polymers. xiii, xiv, xvii, 2, 3, 11, 17–19, 21–31, 33, 36, 37, 41, 43, 45, 52, 54, 57, 58, 61, 65, 67, 68, 74, 77–79, 81–84

PLA PolyLactic Acid. 45, 46

SML Shaping Matter Lab. 36, 37

TNO Netherlands Organisation for Applied Scientific Research. 19

List of Figures

List of Tables

1

Introduction

Within many industries and transportation sectors new innovations are investigated in order to facilitate the energy transition towards a zero emissions economy. One such potential innovation is the use of cryogenic liquid hydrogen or high pressure gaseous hydrogen as a fuel source or energy carrier. Cryogenic storage of liquid hydrogen brings many extra requirements for the extremely low temperature and filling systems, whereas for gaseous hydrogen storage the limiting requirements are the required structural performance for a high pressure storage gas. Gaseous hydrogen is stored at high pressures due to its very low volumetric density compared to fuel sources used nowadays, for example for an equivalent amount of energy gaseous hydrogen at atmospheric pressures takes up around 300 times more space than Kerosene. To solve this volume problem, gaseous hydrogen is stored at very high pressures, industry standards are at 350 or 900 times atmospheric pressures.

In order to use hydrogen it will need to be produced, stored and transported. For the latter two of these steps new solutions specific to hydrogen are required, as opposed to already existing storage and transport solutions for other gasses. Hydrogen is the smallest molecule that exists and therefore it has the highest tendency to leak out of storage or transport vessels. Currently in industry several different solutions exist for storing gaseous hydrogen, among which are metallic and composite storage vessels. Both of these solutions require a liner material on the inside that helps to prevent hydrogen from passing through the wall of the vessel. Traditionally Composite Overwrapped Pressure Vessels (COPV) are the common storage solution for hydrogen, as composites, especially with carbon fibres, can withstand the high storage pressures of gaseous hydrogen.

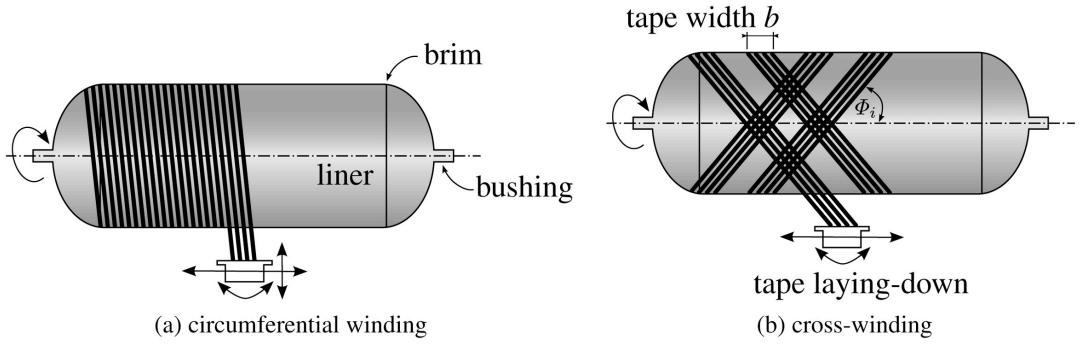

(a) circumferential winding (b) cross-winding

Figure 1.1: The filament winding process [1]

COPV are created with the process of filament winding, shown in Figure 1.1. The internal shape of the pressure vessel is copied to the outer shape of a mandrel, this mandrel is then placed in the winding machine and rotated during the process. While rotating the mandrel fibres are placed on the mandrel and fed from the fibre carriage, which moves along the length of the mandrel. With the combination of rotation speed and carriage speed specific angles of the fibres can be placed on the mandrel. Different layers of specific angles are stacked on top of each other to build up the full pressure vessel laminate. For most COPV designs the liner that is on the inside of the composite wall also serves as the mandrel.

Thus the liner is created in order to serve as an extra barrier against permeation of the stored medium, as well as serving as the mandrel for filament winding.

Several downsides exist with COPV due to their manufacturing methods and material choices. First of all due to the rotational nature of filament winding the mandrel shape is required to have an axis symmetric shape. This ensures that the fibres being put down don't slip off the mandrel while maintaining a constant winding angle. Due to this axis symmetric requirement and the optimal structural design within this space, COPV shapes are either cylindrical or spherical bodies. What really limits the effective usage of this technology for gaseous hydrogen storage is the fact that COPV are always cylindrical or spherical. As this severely limits the effective use of the volume in which the vessel is placed. For example when fitting a passenger aircraft with COPV for hydrogen storage these cylindrical vessels will not take up all the space in the aircraft that can be used. As can be seen in Figure 1.2 these cylindrical vessels are placed in a rectangular frame which is loaded into the cylindrical body of an aircraft. Especially for hydrogen this is inefficient, as hydrogen needs all the volume it can be allocated in a vehicle in order to become an effective fuel source for, amongst others, the aviation sector.

Figure 1.2: Cylindrical COPV mounted in a rectangular frame loaded in a passenger aircraft [2]

As mentioned earlier the filament winding process dictates that the composite laminate of the COPV is built up on top of a mandrel or liner. This imposes an extra step to the manufacturing process for a COPV as the mandrel or liner needs to be created for the specific shape of the COPV.

Finally another downside of using COPV is the commonly used carbon fibres with thermoset resins. Carbon fibres require large amounts of energy to produce inducing a high carbon footprint on the COPV before it is commissioned. Furthermore by using thermoset resins it is not possible to recycle any part of the composite.

This thesis will propose a promising alternative to the manufacturing method, material choice and the future potential structural designs for gaseous hydrogen pressure vessels. This proposed manufacturing method is that of Additive Manufacturing (AM), in the last decades AM has seen large commercial and industrial development, specifically Fused Deposition Modelling (FDM) of polymers. However, one application for which this technique has not yet seen a breakthrough in is the manufacturing of pressure vessels. Two major reasons for this are the relatively low strength materials used with FDM, and its potential for leakage of a high pressure and highly permeable gas through its layered structure. One material and related FDM process that has recently been developed by Gantenbein et al. [3] is the use of Liquid Crystal Polymers (LCP). LCP show high mechanical properties as well as gas barrier properties due to their crystalline nature. When effectively leveraged this crystalline molecular structure can be used to increase its mechanical properties through anisotropy of the print lines. Furthermore as LCP are recyclable this provides a promising opportunity to decrease the waste of these proposed pressure vessels. Of course for this thesis the selected gas to design for could have been selected differently, for example using gasses like oxygen, helium, nitrogen or other commonly used gasses or even liquids

in industry. However one of the main reasons to select hydrogen is that if additively manufactured LCP can withstand hydrogen as a storage gas, it will be able to contain most other gasses in terms of permeability and required design pressures. Due to the small molecular size of hydrogen gas and its aggressive nature in comparison to other gasses, if a specific solution works for hydrogen it will also work for these other gasses.

This LCP anisotropy can be used effectively in a 5-axis FDM process. With this setup several constraints of conventional 3-axis FDM can be removed, while further opening up possibilities of the manufacturing shaping freedom. Print lines can be placed in non planar orientations, which allows for more optimised structures. One specific optimisation that could be possible with 5-axis FDM is producing a linerless pressure vessel in a one-step manufacturing process. If this possibility is realised with LCP 5-axis FDM it could lower manufacturing times and costs significantly. Additionally it removes the axis symmetric constraints from conventional pressure vessels, which means pressure vessels could be manufactured in any geometry, maximising storage volume. The possibility of this 5-axis FDM for pressure vessel manufacturing with LCP shall be investigated in this thesis, providing the basis for future work on the structural design and manufacturing optimisation of pressure vessels.

2 Literature Study

2.1. Hydrogen Storage

One of the potential innovations for the global energy transition is the use of hydrogen as a fuel source or method of energy storage. Due to its molecular size and chemical nature hydrogen is a relatively difficult propellant in terms of storage. In the following chapter the necessity and current solutions of hydrogen storage will be evaluated, starting with an analysis of the need of hydrogen storage in subsection 2.1.1. Followed by subsection 2.1.2 in which an investigation in the current state-of-the-art solutions for hydrogen storage will be presented. Finally the requirements for a new hydrogen storage solutions will be assessed in terms of the barrier properties of a potential material in subsection 2.1.3 and subsection 2.1.4 the and leak rates associated with storing hydrogen in different environments in subsection 2.1.5.

2.1.1. Hydrogen Storage

The world has agreed to move to a net zero green house gas emissions economy by 2050. As part of this transition several different innovations have been proposed in order to move away from fossil fuels in, amongst others, the transport sector. This is an industry run heavily on fossil fuels since its inception, making it a large undertaking to transition away from these energy sources. Furthermore the present scale of this sector poses a high barrier of entry for any new innovation to take its place as a fuel or energy supply. One innovation that can be applied to road, air and potentially maritime transportation is the use of hydrogen as a fuel or energy source. When this hydrogen is sourced from electrolysis ran on green energy this can serve as an emission free energy source for the currently polluting energy sources. Hydrogen fuel cells are being considered for the three previously mentioned transportation sectors. For road transportation hydrogen as a fuel cell source is considered mainly for long range transportation, in the form of trucking [4]. Smaller scale transportation like personal vehicles are already making large steps with fully electric solutions. The aviation sector will also need a complete energy source overhaul on the long term, as battery powered solutions will not be feasible on large scale aircraft. To overcome this again hydrogen fuel cells are being considered to power the aircraft of the future [5]. Finally hydrogen fuel cells are also being considered in the maritime sector [6], which currently accounts for the largest percentage of world trade while still using heavy polluting fuel sources.

For all these sectors and proposed solutions hydrogen fuel cells are implemented in order to generate electricity, which is then used to power the vehicle itself. To supply these fuel cells hydrogen will need to be stored on board of the vehicle in either gaseous or liquid form. In both states high strength materials and structures are required to safely transport the required hydrogen. To effectively transition to a new sustainable economy the solutions necessary for hydrogen storage should be mass and volume efficient while also being recyclable and cost effective.

2.1.2. State of the Art Solutions for Hydrogen Storage

Present day solutions for hydrogen storage can be categorised in two solutions, metallic or composite pressure vessels. Where metallic tanks are large monolithic heavyweight tanks, composite tanks

are lightweight and optimised for high pressures and thus lower volumes. Composites tanks are commonly made in the configuration of composite over-wrapped pressure vessels (COPVs), which means that they contain an internal liner which is over-wrapped with a composite layer, this can be seen in the cross-section in Figure 2.1. The internal liner is present to serve as a permeation barrier for the stored gas or liquid, as well as serving as a mandrel for over-wrapping the composite outer layer. The internal liner does not serve to carry any of the pressure loads, as this is usually a thin polymeric or metallic material. This is where the outer composite layer comes in, which is usually made of a carbon fibre reinforced polymer that is optimised for containing the pressure loads of the tank. [7]

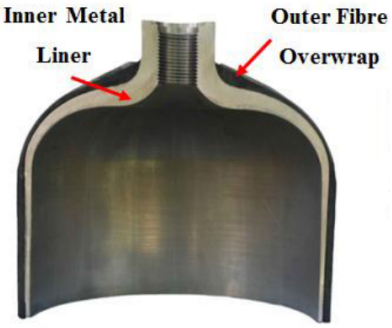

Figure 2.1: Cross section of a traditional COPV [7]

COPV as a solution for hydrogen storage in the energy transition do pose some limitations. The main cause of these limitations is the manufacturing process and possible material choices related to COPV manufacturing. In short COPVs are manufactured in a two step approach, firstly the liner is manufactured which can be a combination of different forming, casting and welding technologies both for a polymer or metallic liner. Finally this liner needs to be over-wrapped with the composite layer, either by filament winding or automated tape laying [7]. This two step approach combined with relatively expensive materials means that the current manufacturing process for COPVs is expensive. Furthermore because of the requirement of having an internal liner to act as mandrel for the over-wrapping process, the geometry of the resultant tank is limited to an axisymmetric geometry. To facilitate the use of hydrogen in the energy transition, solutions are needed of a low cost and with an increasing packing efficiency of pressure vessels in a vehicle. Both these requirements are only marginally obtainable with state of the art COPVs and prospective future improvements. Resulting in the need of completely new manufacturing and material concepts to satisfy the demand for new hydrogen storage solutions.

2.1.3. State of the Art Hydrogen Gas Barrier Materials

In order to find a new solution for storing hydrogen gas, a potential new material should have sufficient gas barrier properties to not let the stored gas escape to the outside of the storage tank. As mentioned previously in COPVs the permeability barrier is created by the liner material. These liner materials can be used to set up a baseline gas barrier performance that will need to be present in novel hydrogen storage solutions. As this research will be focused on applying fused deposition moulding of polymers, only polymeric liner materials will be evaluated in order to compare their permeability performance to a potential new solution. B. Murray [7] has done extensive permeability research on polymeric materials in the context of liner materials. Due to the limitations of the testing facilities Murray evaluated these materials with He gas, the closest proxy for H_2 in permeation experiments. Hydrogen gas is the smallest gas molecule that can be tested for gas permeation, when it is replaced by Helium, which is slightly bigger, the permeation response of a material will change. Murray discusses this effect, and presents data to compare permeation test data with hydrogen and helium. Ultimately the difference between the permeability of the two gasses is comparable and thus helium can be used as a proxy according to Murray.

Furthermore R. Barth et al. [8] summarises hydrogen permeability values of a range of polymers found in other studies and literature. Murray also reports the work of Flaconnèche et al. [9] in which a multitude of polymer materials are tested for permeability of several permeation gasses; He, Ar, N_2, CO_2 and CH_4. Flaconnèche et al. also investigate the effect of different testing conditions, such as applied pressure difference, temperature, and specimen thickness. With these sources combined a good initial analysis can be made of the state of the art permeability of polymeric liner materials, as well as the relation between permeation of different permeation gasses and testing conditions. Table 2.1 gives an overview of the hydrogen permeability values of several polymer materials that can be used as liner materials, from two different sources. The values of the two different sources show some spread for the same materials tested, this could be related to the operating conditions of the individual tests, which are unfortunately not reported. However, the permeability values here presented can be used to compare the order of magnitude of the permeability of other materials.

Sample Material	Permeability	Reference
	[cm^3/m· s· bar]	
HDPE	1.84 - 1.99E-06	R. Barth [8]
PE	2.24 - 6.94E-06	
PA	3.14 - 8.97E-07	
PP	6.95E-06	
PFA	9.20E-05	B. Murray [7]
PEEK	8.70 - 10.20E-06	
PEEK	8.74 - 26.90E-07	R. Barth [8]
PTFE	5.10 - 12.00E-05	B. Murray [7]
PTFE	7.17E-06	R. Barth [8]

Table 2.1: Overview of H2 permeability values for a range of polymers commonly used in liner applications

2.1.4. Permeability

In order to quantify different materials for their use as a barrier against hydrogen gas transport through the barrier material several parameters can be used. The most straightforward measure to look at is the leak rate of a gas through a material, which can also be seen as the pressure loss of the stored gas in a vessel, or the pressure increase on the low pressure side of the barrier material. However, these can change significantly if the thickness of a barrier material is increased, and they are also dependent on the applied pressure difference over the barrier material. Another parameter that is used to classify barrier materials is the permeability coefficient, which is independent of the applied pressure difference and the barrier thickness. The permeability of a barrier material is different for each so called permeate gas, which is the gas that passes through the barrier material. As such the permeability coefficient can be used to compare and classify different materials for their permeability of different permeate gasses. [7], [10]

Modelling Permeability

Several models exist that describe the permeability coefficient P for different materials and environments. Ismail et al. [10] describe several of these models and their applicability to different barrier materials and structures. The driving force behind any of the permeation models is the presence of a pressure differential on two sides of a barrier material. Gasses will be absorbed by the surface of any material, so when the pressures of the gas on two sides of the material is different the concentrations of absorbed gasses on the two surfaces will also vary. This concentration difference causes a gas diffusion flow to occur from the high pressure side to the low pressure side of the barrier material. This phenomena is split up into three process steps. Firstly the permeating gas is absorbed into the barrier on the high pressures side. Followed by the diffusion of the gas through the barrier. Finally desorption, or alternatively called evaporation, of the permeating gas occurs on the low pressure side of the barrier.

For gaseous permeation through polymers the absorption and evaporation occur at higher rates than the diffusion through the polymer. This means that the diffusion is the rate controlling step of permeability. Thomas Graham [11] proposed the solution diffusion model to combine this three step model into one. From the solution diffusion model the permeability is governed by two separate parameters, the diffusion coefficient D and the solubility coefficient S. Multiplying these two coefficients results in the permeability coefficient. The diffusion coefficient describes the rate of a permeating gas molecule moving through the bulk barrier material and the size of this movement. It is governed by the interaction of the specific polymer material and the permeating gas molecule. The polymer will restrict the movement of a gas molecule depending on how flexible the polymer molecules are. The size of the permeating gas molecule also affects the diffusion coefficient, as a larger molecule will move through the polymer at a lower rate than a smaller molecule that can more easily pass between the polymer molecules.

The solubility coefficient describes the ability of the bulk material to store the permeating gas at a specific applied pressure. Multiplying these two parameters results in the permeability coefficient, which describes the amount of gas flowing through a specific surface area of a barrier material over a

recorded time interval for the barrier thickness and applied pressure difference. [7], [10]

Factors affecting permeability

As mentioned previously permeability is greatly dependent on the barrier material, the permeating molecule and their interaction. However, other factors common in all polymer barrier materials may also affect the permeability, and can be useful to determine the optimal conditions for hydrogen permeability. Although the applied pressure differential is taken into account in the calculations for permeability there are sources stating effects of high pressures (> 150 bar) on the solubility and thus permeability of specific polymers [9]. Although extensive research of different polymers on the effects of high pressures on permeability or solubility and diffusion is still lacking. H. Fujiwara et al. [12] developed a permeability test cell capable of pressures up to 1000 bar, with which they tested high density polyethylene for hydrogen permeability. The results of these tests show a decrease of the permeability value by a factor of two when increasing the applied pressure from 100 bar to 900 bar. However, they also report other claims in literature describing different results, related to the specific polymer under consideration. Different polymers will respond differently to high pressure environments with respect to plastification and dissolved gas concentration. For a reliable analysis of the effect of high pressures on the permeability it is necessary to test the specific permeate gas and barrier material together at the operating conditions of interest.

Furthermore with the use of polymers temperature will have an effect on the permeability due to reaction of the polymer molecules to a temperature change. In general polymer molecules will relax at elevated temperatures creating more freedom of movement for a permeate gas molecule to pass through. This results in an increase of permeability for an increasing temperature. Literature reports that this relation follows the Arrhenius equation[7]–[9], [13]. With specific testing the parameters for the Arrhenius equation of a specific polymer and permeate gas combination can be obtained, resulting in an accurate estimation of the temperature dependence through the Arrhenius equation. However, if this temperature dependence is not required for a large temperature range, the permeability tests should be performed at the desired operating temperature to obtain the relevant permeability values directly.

Testing permeability

The ASTM D1434-92 test standard [14] can be used to test a potential barrier material for its permeability coefficient for a specific permeate gas. B. Murray [7] proposes an updated version of this test standard, replacing the measurement of the permeated gas with a pressure transducer instead of a liquid slug indicator, which is also reported by Flaconnèche et al. [15]. Apart from this change the same methodology from the ASTM standard is applied. With this test setup a specimen of the potential barrier material is placed in between two pressure chambers, sealed with two O-rings on each side of the specimen. The upstream chamber will be filled with the permeate gas at the testing pressure and temperature, while the downstream chamber will be evacuated to a vacuum before hand. Once the upstream chamber has reached the desired temperatures and pressures the downstream chamber pressure will be recorded over an extended period of time. The pressure increase on the downstream side can be used to obtain the permeability coefficient. Initially the pressure in the downstream chamber will increase non linearly, which is called the transient region, after a certain amount of time the pressure increase reaches a constant steady state rate. From this steady state pressure increase two time points are taken, one at the start of the steady state region and one at the end. The equivalent volume at standard pressure and temperature is then obtained at both time points, from which the volumetric leak rate is calculated. With the leak rate, pressure difference and sample thickness the permeability coefficient is obtained. [7], [9], [14], [15]

2.1.5. Industry Standard Permeability and Leak Rates

The previous section established how to test for permeability and what affects permeability. However, knowing this is meaningless if the hydrogen safety context of a pressure vessel is unknown. When hydrogen gas leaks from a pressure vessel it accumulates in the surrounding environment, where care should be taken to prevent an explosive air mixture to arise. To prevent this from happening several industry standards have been developed to set a maximum allowable leak rate for specific scenarios of gaseous hydrogen storage.

P. Adams et al. [16] report results from several studies of allowable leak rates in the road vehicle sector. These studies focus on the scenario's of road vehicles leaking small amounts of hydrogen into

improperly ventilated surroundings, e.g. underground parking, garages, tunnels, etc. If a large enough amount of hydrogen leaks into these kind of surroundings the air mixture could reach a critical ratio of hydrogen and oxygen to allow combustion to occur. This report sets the requirement of hydrogen concentration in the air to a maximum of 1% by volume. This results in a maximum allowable leak rate of 6 mL per hour per litre of storage tank volume, or alternatively 15 mL per minute taking into account the pressure vessel volume used in this study.

M. Robinson [17] presents a study in the allowable leak rates for launch vehicles. In this case the critical air mixture for combustion, as mentioned for the road vehicle case, is used as one requirement. However, because of the high efficiency of launch vehicle design, the propellant loss due to permeation is also considered an important requirement, which is set at a total of 0,25% loss of hydrogen measured in total tank volume. This can then be converted to leak rates by dividing this volume by the time from fuel loading to engine cutoff. For lower stages of a launch vehicle this means that quite a large leak rate is allowed. However, for upper stage or spacecraft propellant tanks, which need to store their propellant for long durations, the leak rate requirement becomes much lower.

Similar requirements are reported by S. Mittal et al. [18] for the use of hydrogen in the aviation sector. In this case the requirements are mainly driven by the containment of enough hydrogen in liquid and gaseous form to fulfil the flight of an aircraft. Most commercial flights are in the order of hours and for long distance flights in the order of fifteen hours, which results in leak rate requirements which are dependent on the flight time. Because of this relatively low operation time of a pressure vessel the leak rates can be relatively high compared to what is used for the road vehicle sector. However, the combustion concerns are also present in aviation, if a large enough amount of hydrogen were too leak and mix in the air of the aircraft it could allow combustion to happen. Several solutions for this are presented by S. Mittal et al. one of which is to purge the volume of air surrounding the hydrogen storage tank with nitrogen in order to prevent an explosive mixture to arise.

Although several standards for hydrogen leak rates are presented in literature for specific cases in different industries, there is not one singular requirement that can be applied to any new hydrogen storage solution. For a new storage tank design the use case should be analysed, after which leak rate requirements can be set up to prevent combustive air mixtures to accumulate and to prevent too much stored hydrogen to leak out.

2.2. Liquid Crystal Polymers

Liquid Crystal Polymers (LCP) promises to be a suitable candidate as a high performance material for additive manufacturing, specifically for fused deposition modelling (FDM). In the following chapter the available literature on LCP materials will be reviewed and its application as a material for FDM and hydrogen storage will be further investigated. In subsection 2.2.1 a review of LCPs is presented after which subsection 2.2.2 and subsection 2.2.3 will discuss the application of FDM with LCPs and their mechanical performance. Finally the hydrogen performance of LCPs are considered in subsection 2.2.4.

This literature study has been performed in order to start a thesis topic within the Shaping Matter Lab (SML) of the Aerospace Engineering faculty of the Delft University of Technology. The specific type of LCP Vectra A950 will be considered as candidate material in this literature study.

2.2.1. Introduction to Liquid Crystal Polymers (LCP)

LCPs are a specific group of polymers that are differentiated from other semi-crystalline polymers because of their molecular structure and behaviour. The specific LCP that will be referred to in this literature study is the range of polymers produced by Celanese called Vectra, the LCP of choice for FDM processes within the Shaping Matter Lab. Vectra has a range of different grades of LCP which are all random copolymers made of two monomer units; hydroxybenzoic acid (HBA) and hydroxynaphthoic acid (NHA). The HBA molecules posses strong liquid crystal behaviour, although a polymer of this molecule will have high melting temperatures. By randomly adding NHA molecules, and thereby creating the Vectra copolymer, the melting temperature is reduced as the HBA polymer chain is interrupted, adding more chain flexibility. When effectively tuning the ratio of HBA molecules to HNA molecules the melting temperature can be tailored as well as the mechanical and thermal properties. [3], [19]–[21]

LCPs behave like a liquid above their melting temperature, but within this liquid state they also exhibit crystalline properties. This is what gives them their name of LCP. This means that in the molten state

the material, in this case the polymer, is able to flow while also containing a crystalline molecular order. Within a LCP like Vectra groups within a molecule together form mesogenic units, which are rod like parts of the molecule that can form a liquid crystal phase. HBA as a standalone molecule forms these mesogenic units, However, as mentioned previously a second monomer needs to be added to break the periodicity of the chain and therefor allow smaller mesogenic phases to occur within the molecule. The orientation and arrangement of these mesogenic units in a certain phase can be classified in three distinct phases, nematic, smectic and cholestoric. The state seen in Vectra is the nematic phase. In this state the mesogenic units are aligned together along a certain direction. The alignment is not perfect, as each mesogen varies slightly in orientation around the average nematic direction. In the large scale domain of the entire melt no order exists, However, within a microscopic domain the mesogens are closely aligned. This means that within a melt a large number of nematic domains can exists, all internally aligned with each other but randomly orientated throughout the melt. [21]

In the case of Vectra the liquid crystalline phase is present in a melt when the temperature exceeds the melting temperature, what is also called a thermotropic LCP. As an alternative there also exist LCP for which the liquid crystalline phase is triggered by adding solvents to the system. [20], [21]

2.2.2. Development of LCP Fused Deposition Modelling

As early as the last decades of the previous century developments have been made in the application of LCP as a high performance material. The first steps were made in the application of LCP fibres as a reinforcement in thermoplastic composites [22]–[24]. The aim of these processing techniques was to produce thermoplastic sheets blended with short LCP fibres as reinforcement. The work of Handlos et al. [22], Isayev [23], and Sabol et al. [24] present significant improvements in mechanical properties of the LCP thermoplastic composites over the neat thermoplastic and other short fibre reinforcements. The limitations of these works is with the use of short LCP fibres, as the processing techniques at the time were not yet ready for longer length scales of LCP material. However, this ongoing research and development on LCP laid the ground work for the application of long LCP fibres.

Gray et al. [25] recognized the potential of the LCP fibres used in the the thermoplastic composites mentioned previously for the use in fused deposition modelling (FDM). The small diameter that could be achieved with extruded LCP fibres in these composites could be used for creating prototypes with higher dimensional precision as compared to extrusion processes with conventional glass and carbon fibres. The process used by Sabol et al. [24] used a dual extrusion approach where the LCP fibres and thermoplastic matrix were melted and extruded separately. This approach was used to make sure that both materials were processed at their respective melting temperature, without the thermoplastic matrix degrading at the higher melting temperature of the LCP. After extrusion of the LCP it was cooled and mixed in with the extruded thermoplastic polymer to form a reinforced blend of thermoplastic matrix with LCP fibres. This blend can then be used for extrusion purposes. This dual extrusion method was used as a starting point of the work of Gray et al. [25], [26].

With the dual extrusion method, Gray et al. [25], [26] developed LCP reinforced polypropylene mono filament for use in a FDM printer. Short fibres of LCP are extruded and mixed into the molten polypropylene which is then extruded at the polypropylene processing temperatures to form a mono filament. This mono filament is then fed into the the FDM printer with which different samples were manufactured. These samples showed a significant increase, of 150%, in tensile modulus with respect to samples manufactured from only polypropylene. Furthermore the samples showed an increase of 100% of the tensile modulus with respect to ABS samples, where ABS was the highest performing FDM material in terms of mechanical properties at the time.

Additionally Gray et al. [25], [26] also manufactured samples made from neat LCP. Using the same FDM setup and design of the samples neat LCP filament was fed into the FDM printer. The results of the mechanical tests on these samples showed that the neat LCP samples outperformed the ABS samples by roughly four times on tensile modulus and strength. These results indicate the possibility of producing parts with FDM with higher tensile properties than previously possible. Gray et al. theorise that the limited temperature of the FDM printer used in their work to be a part of the cause of delaminations which occurred in their samples, as their temperature was limited to $300°$C. After a print line has been laid down it would cool to quickly to a solid state before an adjacent line or layer is placed next to or on it. The LCP material used in this work is Vectra A900 [26], with a proposed processing temperature of $320°$C and a melting temperature of $280°$C [25]. If the material can only

be heated to 300°C and solidifies at 280°C then there is indeed only a small range of temperature before the material cools down below the melting temperature. Improving the temperature range of the FDM setup could therefor decrease the delamination problems for this material.

Gantenbein et al. [3] further explored the possibilities of using LCP in an FDM printer in recent years. Recognising the potential and limitations of LCP additive manufacturing a new study was performed on LCP FDM. With a modern desktop FDM printer modified for higher temperatures, up to 400°C, the temperature limitations of the FDM printer of Gray et al. could be resolved. Furthermore a new grade of Vectra was also used, Vectra A950 instead of A900. With this setup the molecular orientation of LCP can be effectively leveraged to increase the mechanical properties of a printed part. In this study Gantenbein et al. recognized from microscopy that the printed filaments form a core and shell micro-structure, an image of this can be seen in Figure 2.2. This micro-structure is formed upon cooling of a print line, where the temperature gradient between the center of the printed line and the ambient temperatures dictates the ratio of the thicknesses of the shell to the core. The longer it takes for the material to cool the more time the material has for its orientated domains to return to their isotropic orientation. When the cooling happens fast, in essence what happens in the shell of a printed line, the print line orientated domains formed by the shear forces in the nozzle of the printer are frozen in. And thus the shell of the print line will have nematic domains orientated with the print line direction, whereas the core of the print line has isotropically orientated domains.

Figure 2.2: An electron microscopy image of a printed filament presenting the core and shell structure [3]

Furthermore Gantenbein et al. [3] have shown that recycled LCP can be reused with FDM printing without the loss of processability. This provides enormous potential for reusability of the material in a pressure vessel. Especially if the entire part consists of only LCP, then the entire part can be recycled in a single process. The recycling process consists only of mechanically shredding the material into small pieces, which are of the same size as the original pellets that are used to manufacture the FDM filament. These recycled pieces can then be just as easily used to form filaments as the original pellets. If the LCP is annealed the recyclability is reduced significantly due to the increase of the molecular weight of individual LCP molecules, this increased is caused by the annealing reaction.

2.2.3. Enhancing LCP Performance with Fused Deposition Modelling

As described before when printing LCPs with FDM the microscopic domains of the molten material are aligned with the flow in the nozzle, resulting in anisotropic print lines with microscopic domains aligned with the print line direction. There are several factors that can be altered in the FDM processes, which ultimately play a role in the anisotropy of the print line and its overall mechanical performance.

Gantenbein et al. [3] performed a study on several of these factors in order to assess the mechanical properties of the specific LCP Vectra. The main conclusion from this study was that the ratio of the print line aligned shell to the isotropic core has a major contribution to the mechanical properties of a print line. The parameters that affect this ratio are printing temperature, print line height and nozzle width. All these factors influence the rate and duration of cooling of the print line from the nozzle temperature to below its melting temperature. The quicker the print line cools down to below the melting temperature, the higher the ratio of shell to core within the print line. If a low temperature is used in the nozzle then the print line will cool quickly and freeze in the aligned domains. However, if the printing temperature is too close to the melting temperature then flow issues will arise in the nozzle and just after leaving the nozzle, as well as poor adhesion between print lines as the material is already solidified when being placed next to a previous print line. The optimal temperature for maximum mechanical properties is found to be around 295°C, although this value is also influenced by the environmental conditions and the specific

printer setup used. Furthermore if the print lines are printed with a thin nozzle and low layer height the cross sectional area of the print line is small enough that the center of the print line also cools quickly enough such that its aligned domains are frozen in. Maximum mechanical properties were reported at a nozzle diameter of 0.15 mm and a layer height of 0.05 mm. With these optimal processing conditions the mechanical properties of single print lines are comparable to composite materials, furthermore considering the possibility of tailoring the print lines for maximum mechanical performance of the final part with FDM the mechanical performance of resulting parts can rival those of high end composites.

Another improvement of the mechanical performance of printed Vectra is to anneal the part after it has finished printing. Annealing the part at a temperature just below its melting temperature will initiate a post condensation reaction between the LCP molecules which results in chemical cross linking between molecules. This cross linking also occurs between molecules of adjacent print lines, such that cross links are established over the interface between these print lines. An increase of 50 to 100% of the bending strength has been reported depending on the orientation of the print lines in the tested samples. [3]

Another method to improve the mechanical performance of Vectra A950 manufactured with FDM has been investigated by C. Houriet [20]. This research was focused on evaluating the mechanical interlocking of print lines with overextrusion. These print lines will have a small amount of additional material that coalesces on top of the print line, when another print line is laid down on top of this the material flows around the additional material of the first print line. These interactions between the print lines cause mechanical interlocking and when this is effectively used it can increase the shear performance of a sample by roughly 100%.

2.2.4. LCP Performance as a Hydrogen Gas Barrier

With LCPs being a strong candidate in terms of mechanical properties and manufacturing capabilities, the most important factor to evaluate is its performance as a hydrogen gas barrier material. In section 2.1 the permeability of several commonly used liners has been presented, to which LCP permeability can be compared. The LCP Vectra A950, which is used in the Shaping Matter Lab, has excellent barrier properties as presented in the data sheet by its manufacturer Celanese [19]. Their data presented in the data sheet show that their LCP range performs more than an order of magnitude better in oxygen permeability, as compared to other commonly used polymers. Next to that they also present several values for hydrogen permeability at different temperatures, which are tabulated in Table 2.2.

B. Smith et al. [27] performed a study on the hydrogen permeability of a range of commonly used liner materials and also a thermotropic LCP, specifically DuPont HX 3000. Although a different LCP is evaluated here, the permeability value obtained is within the range of values reported by Celanese.

Furthermore S. Ando et al. [28] present permeability values for a large range of polymers tested for O_2, CO_2 and N_2 permeability. For all three gasses the LCP specimens showed the lowest permeability values compared to all other polymers used. The LCP used in this test is labelled as HBA/HNA, which are the same monomers used in Vectra A950. Although the exact ratio of HBA/HNA is not given in this study, it can be assumed that it is a close relative to Vectra A950 and that although exact values might differ the same permeability trend holds.

Finally B. Grimsley et al. [29] researched several candidate materials to serve as a liner in a COPV for cryogenic liquid hydrogen storage. Among these materials they tested Vectra A950 as a candidate next to several polymer materials and metal and polymer stacked composites. As a replacement for hydrogen gas the permeability tests in this research was performed with argon gas, with a similar molecular diameter as hydrogen. In this case the results showed that the Vectra specimens performed on average with the other materials, However, it was one of the better performing specimens of the monolithic specimens. The specimens that performed better than Vectra were composite or hybrid samples consisting of different polymeric materials and or metals.

The results of these four different LCP permeability sources are tabulated in Table 2.2. All these permeability values have been established with solid specimens of bulk LCP manufactured in one piece. A big unknown for the permeability of an additively manufactured specimen with FDM is what the effect is of the interface between two print lines on the overall permeability. As a starting point the assumption can be made that the permeability values of an individual print line are within the same range as what is expected from the data presented here. To the author's knowledge no research has been performed on the effect of FDM printed parts on the permeability of such a part with respect to the bulk material. However, some research has been carried out on the leak tightness of parts manufactured with FDM

Permeate Gas	Testing Temperature	Sample Thickness	Permeability	Reference
[-]	[deg C]	[mm]	[cm^3/m·s·bar]	[-]
Hydrogen	40	0,05	4.51E-08	Celanese [19]
Hydrogen	150	2,5	2.84E-06	Celanese [19]
Hydrogen*	~50	unknown	1.57E-07	B. Smith et al. [27]
Oxygen	23	0,025	2.60E-10	Celanese [19]
Oxygen	unknown	unknown	3.75E-11	S. Ando et al. [28]
Argon	20	0.04	4.67E-12	B. Grimsley et al. [29]

Table 2.2: LCP permeability values from literature, for a variety of gasses. All materials tested are Vectra A950, except * which is DuPont HX 3000.

from commonly used FDM polymers. [30], [31]

2.2.5. Liquid Crystal Polymer Spin Printing

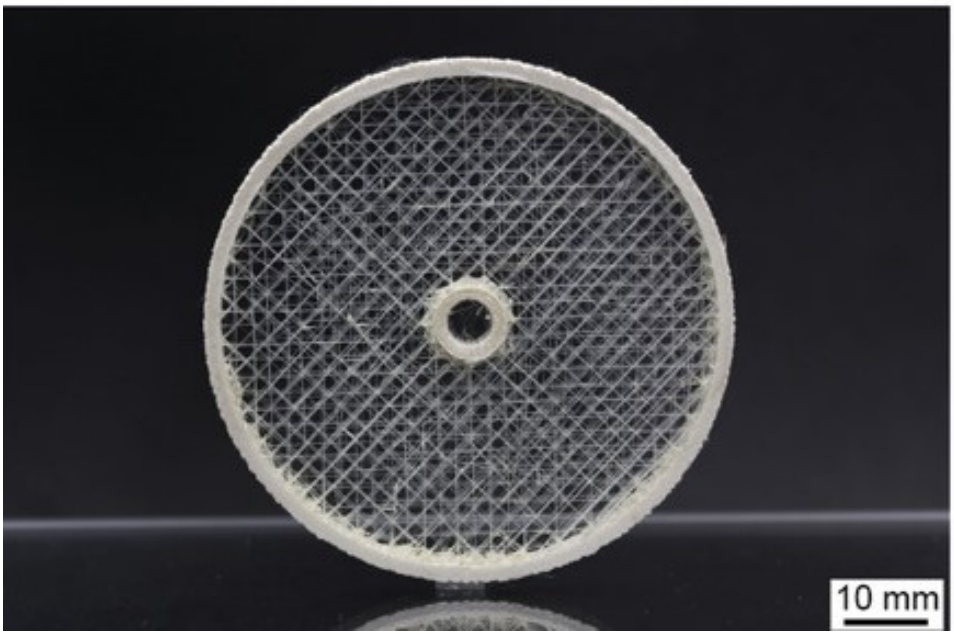

Figure 2.3: A wheel printed with internal LCP spun fibres [32]

With the use of LCP FDM as material manufacturing method a structural reinforcing method is possible to be added internally in the pressure vessel. S. Gantenbein et al. [32] developed a method of spin-printing thin LCP fibres with desktop FDM printers. The thickness of these fibres can reach values as low as 20 μm, which results in the microscopic print line aligned orientation being frozen in for a larger percentage of the cross section than thicker fibres. The tensile properties of these spun fibres are greatly increased with respect to conventional diameter print lines manufactured with conventional FDM parameters, with the thinnest spun fibres obtaining about a 10 fold increase in tensile modulus and strength.

The work of Gantenbein et al. present several use cases for these spun fibres. The first being embedding these spun fibres in LCP laminates printed with conventional print parameters, in this case the spun fibres are used to enhance the stiffness of the laminate in the directions they are laid down. Furthermore other possibilities of the spun fibres are structures where the spun fibres are designed to be loaded in tension in order alleviate stress in other regions of the part. An example can be seen in Figure 2.3.

One possibility of implementing these spun fibres internally in a pressure vessel is to add spun fibres from one side of the wall to the opposite side. Similar as to how the spun fibres were used in Figure 2.3, but without the central circular structure. These fibres will then be loaded in tension as the internal pressure loads the walls of the pressure vessel. When these fibres are being loaded in tension stresses in the wall itself will be taken up by the fibres, which means the wall thickness can be reduced.

2.3. 5-axis Fused Deposition Modelling (FDM)

Adding two axes to a conventional fused deposition modelling setup allows several issues inherent to FDM to be solved while also greatly increasing the shaping freedom of FDM. The following sections will present the limitations of conventional 3-axis FDM (subsection 2.3.1), and the solutions (subsection 2.3.2) and possibilities that a 5-axis setup will bring (subsection 2.3.3).

2.3.1. The Limitations of Conventional FDM

In a conventional FDM setup 3 axes are used to control the motion of the nozzle with respect to the part or vice versa. These motion axes can be orientated in a Cartesian or delta setup, which in both cases cause the nozzle to move in the x,y and z directions with respect to the part. Due to the nature of printing parts in this 3 axis setup the material is always deposited from the bottom up. Without this sequence material would be deposited in mid air, which would not result in a working setup. Therefor conventional FDM printers always print from the bottom up in a planer manner, a part is sliced into planar layers that are deposited in order from bottom to the top. This sequence is also known as 2,5D FDM to indicate the loss of the full 3D motion.

With the planar 2,5D sequence the resolution of the final part geometry is limited to the layer height of the individual print layers. When printing a specific geometry the digital file will have a continuous contour, however when this is sliced into the printing layers the continuous geometry is discretised into steps based on the layer height of the print. This means that for diagonal contours with respect to the horizontal and vertical directions of the part staircase type steps will be present. [33]–[37]

Furthermore because of the 2,5D style printing it is not possible to print sections of a part that have an overhang with respect to the build plate. These sections will always need extra material below it to support the new layer being deposited. Otherwise the first overhanging layers will be deposited in mid air, failing to put down the material in the correct place. This means certain geometries with internal overhangs can not be printed with removable supports. Additionally the use of support material means that more material is used and a longer manufacturing time is needed, both increasing the manufacturing costs. Finally the surface finish of the overhanging sections of a part are of lower quality due to the initial attachment and subsequent removal of the support material. [33]–[37]

2.3.2. The Solutions of 5-axis FDM

By adding two rotational axes to the base-plate or print-head of a FDM printer several of the limitations presented in subsection 2.3.1 can be resolved. The foremost reason for this is that with a 5-axis setup the orientation of the nozzle with respect to the base-plate, and consequently also the part, can take on different angles that are no longer limited to the single 3-axis perpendicular orientation. In a 3-axis FDM printer the nozzle is always orientated perpendicular to the base-plate, However, with the two extra rotation axes of a 5-axis FDM printer the nozzle can be orientated in many different orientations with respect to the base-plate, only limited by the range of motion that is possible with the chosen new rotation axes. [34]–[38]

As previously mentioned a 5-axis FDM printer can be constructed with the two additional axes mounted on the base-plate or on the nozzle, or a combination of these two options. All three of these combinations are presented in Figure 2.4. Both the base-plate and nozzle configuration have their advantages and disadvantages. However, in all cases the main advantage of the 5-axis control is that the nozzle can be orientated, with respect to the part, in such a way that the previously printed lines are directly inline with the nozzle. Which means that the next line to be deposited is targeted at a piece of the part which has already been printed. This will remove the necessity of support material in a majority of the cases. There are some situations were support material is inevitable, due to high angles between subsequent print lines or when a very flexible structure is printed that can not support its own weight and momentum while being moved around in a 5-axis base-plate setup. Additionally support material will be necessary for parts that do not have geometry that is fully connected to the base-plate on the

lower side. In essence this means that if the bottom faces of the part with respect to the base-plate are not touching the base-plate the negative space will need to be filled up with support material to hold up the first layers of the part. But once this has been completed no further support material will be needed for overhanging structures. [34]–[38]

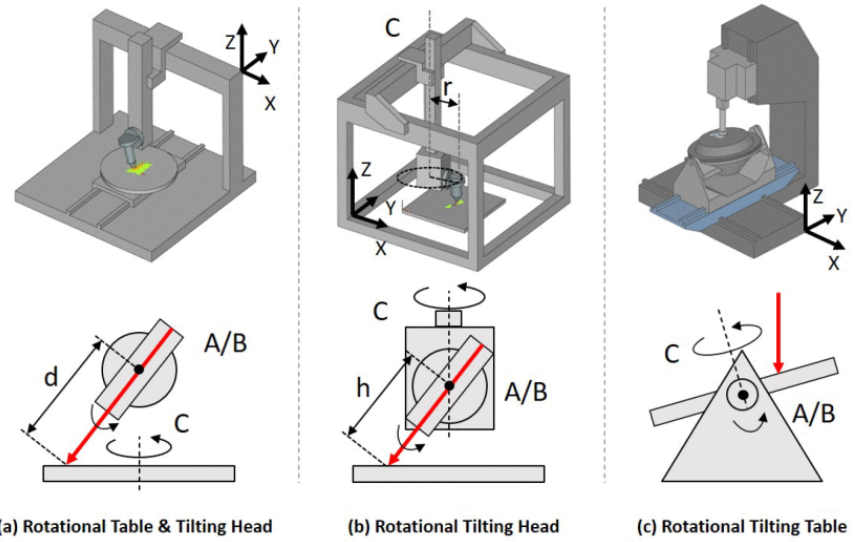

Figure 2.4: The three different configurations of the two addition rotational axes of a 5-axis FDM printer [39]

One of the main differences between the 5-axis base-plate or nozzle setup is the orientation of the nozzle with respect to gravity. In the 5-axis nozzle configuration the nozzle is free to move around with two additional axes, meaning that it can rotate away from the vertical axis with respect to gravity. Conventional 3-axis FDM printers will always have the nozzle orientated along this gravity direction. In a 5-axis base-plate setup the nozzle is also kept orientated along the gravity direction. Aligning the nozzle with gravity means that a print line being deposited is always pulled down the gravity direction and thus in line with the nozzle. If the nozzle is not orientated along the gravity direction, then a print line which is being deposited will be pushed out of the nozzle along a different vector than the one along which gravity is acting. Depending on the material and processing conditions this can have a large effect on the quality of the print line and final part. [34]–[38]

Furthermore, one of the other limitations of conventional 3-axis FDM can also be solved by adding two additional rotation axes. As presented in subsection 2.3.1 3-axis FDM printers work with the 2,5D deposition principle, which means that a part is built up from the bottom to the top with planar layers of material. With 5-axis FDM non-planar layers can be designed and manufactured. In practice this is also possible with 3-axis FDM setups [40], However, 5-axis non-planar geometry opens up a lot more possibilities in terms of non-planar geometry. More importantly this always allows the nozzle to be perpendicular to the current point of the print line for any geometry, whereas this is only possible with 3-axis FDM if planar layers parallel to the base-plate are used. By carefully designing non-planar print layers with 5-axis FDM in mind the outer contours of a part can be printed as complete enclosing layers, which will greatly increase the surface finish with respect to the staircase type surface finish that is present on planar 3-axis FDM parts.

2.3.3. Further Possibilities of 5-axis FDM

Another interesting possibility of 5-axis FDM, which does not exist as a solution to a 3-axis FDM limitation, is to align the print lines and layers in a specific way to improve the mechanical properties of the part. This could be to improve the strength, stiffness or damage resistance. Especially when using a material that shows anisotropic properties in the printed lines this can be used for a highly mechanically optimized design.

G. Fang et al. [34] present a method of aligning non-planar layers and print lines with a strength-aware design. From a finite element analysis an optimized field is created based on the boundary and

loading conditions of the desired part. This is further optimized to account for collision prevention during printing. From this optimization field the individual print line paths on the curved layers. For parts that do not have a final optimized geometry that is touching the base plate in all locations support material is used. This supporting material is water soluble such that it can be easily removed. Furthermore the supporting material serves as a basis to create the non-planar print layers.

T. Zhang et al. [39] take this work further by improving the print quality of the parts with improved motion control. Issues can arise when creating Gcode for the 5-axis printer where large motions in the rotation axes are used for only a small rotation movement of the nozzle. Generally this happens close to singularities of the printer which occur when the nozzle vector is close to perpendicular to the plane of the base-plate.

3

Research Definition

3.1. Knowledge Gaps

The literature reviewed in chapter 2 has exposed several knowledge gaps in the application of 5-axis Fused Deposition Modelling (FDM) with Liquid Crystal Polymers (LCP) for hydrogen pressure vessels. Three distinct knowledge gaps can be identified related to the selected material, the manufacturing method and the potential structural optimisations. The main knowledge gap for the use of additively manufactured LCPs as a pressure vessel material is how the permeability of the material changes from its bulk properties to its additive manufactured form. The bulk properties are generally tested by the manufacturer or separate researchers, however no research has yet been performed on the permeability of FDM printed samples. The interface between adjacent print lines can significantly reduce the permeability if voids are present in this interface. This effect should first be investigated in order to assess if LCPs can be used with FDM to manufacture pressure vessels.

Furthermore, the application of 5-axis FDM for the production of pressure vessels has not been investigated. In particular the concept of the one step process of printing a linerless pressure vessel, in which the structural wall of the vessel also acts as permeation barrier to the stored gas, is an untried concept in additive manufacturing. This concept should be tested in order to assess its adoption as manufacturing method for pressure vessels, additionally the limitations of the system can also be determined.

Finally, if the previous two knowledge gaps are filled, and the conclusion is that the material will suffice as permeation barrier and 5-axis FDM is a working candidate for pressure vessel manufacturing, then the possibilities of structurally improving the state of the art pressure vessel designs can be investigated. The shaping freedom obtained with the combination of LCP with 5-axis FDM, has not been extensively researched. This synergy should be leveraged to experiment with different novel structural concepts that are as of yet unexplored in the state of the art pressure vessels, such as shape optimisation, variable angle filament paths in the wall and adding internal structures in the vessel.

3.2. Research Question

The main research question of this proposal aims to fill the knowledge gaps identified in the previous section, and is presented below:

"How can 5-axis FDM with LCP be utilised to manufacture gaseous hydrogen pressure vessels, while providing a strong barrier against hydrogen permeation and improving the structural efficiency in comparison to state-of-the-art pressure vessels?"

The main research question is broken down into three sub research questions listed below, each focusing on one of the three main research areas of this project.

1. How can additively manufactured liquid crystal polymers provide sufficient hydrogen gas permeability for the use in a hydrogen gas pressure vessel?

2. How can 5 axis fused deposition modelling be used with liquid crystal polymers in order to manufacture linerless pressure vessels in a one step process?

3. Is it possible to manufacture novel pressure vessel geometries, including new structural strengthening elements, that have a higher structural performance than conventional pressure vessels?

Sub-question one is aimed at investigating the hydrogen gas permeability behaviour of additively manufactured LCP, as this is currently the largest unknown that needs to be answered if additively manufactured LCP are to be used for hydrogen pressure vessels. The second sub-question aims to provide a proof-of-concept manufacturing method for linerless LCP pressure vessels, and will identify any problems in the setup and process that will need to be solved. Finally, the third sub-question can be split into two improvements to be investigated, the first related to the pressure vessel geometry. And the second being the structural concepts used, such as different structural optimisation methods and novel internal and external strengthening concepts that are only possible with the use 5-axis FDM.

3.3. Research Scope

The scope of this thesis is split up into three parts. First of all the most important knowledge gap defined will be investigated, the permeability properties of additively manufactured LCP. The focus will be on validating the use of additively manufactured LCP as a hydrogen barrier material, within the resources available of this thesis.

Secondly the scope of this research will focus on developing the methods and processes for printing a linerless pressure vessel. For this part of the thesis the main goal is to setup these processes and improve or solve any issues that arise during this process. Once this has been achieved it can provide a proof of concept as a new manufacturing method for pressure vessels.

To further validate this proof of concept the third part of the research scope will be to manufacture several pressure vessels with varying parameters and included concept. These pressure vessels will be pressure tested to validate their basic use as a pressure vessel and assess if any effects of the variables in the designs are present. The goal here is to test relatively simple structural designs in order to validate the manufacturing process. This work will pave the way for future research to manufacture optimised structures and geometries that reach the full potential of pressure vessels manufactured with 5-axis FDM with LCP.

3.4. Research Plan

The research questions proposed in the section 3.2 will be used as a starting point of the subsequent master thesis. A first research plan proposal is presented here in order to answer these research questions.

The first step will be to investigate the hydrogen permeability of LCP samples manufactured with FDM to answer the first research sub-question, as it is currently unknown how manufacturing LCP parts with FDM will change the permeability of the bulk material. Hydrogen gas permeability tests will be performed with FDM manufactured LCP samples. These samples are to be designed with the best estimated parameters, these optimal parameters can be obtained from a microscopic investigation on the cross section of different samples with varying FDM processing parameters and overall design. From this microscopic investigation the optimal cross section can be designed and implemented in the samples to be tested for permeability. The results of the permeability tests will decide if LCPs manufactured with FDM are a suitable candidate for hydrogen pressure vessels, and if they are the results will also govern the required thickness of the designs of pressure vessels that will be manufactured with the 5-axis FDM printer.

In order to manufacture these pressure vessels on an 5-axis FDM printer it will need to be assembled and the necessary software for generating Gcodes will need to be written. Currently a 5-axis FDM setup is present and operating in the Shaping Matter Lab, where the thesis will be performed. However, it will need to be modified with a rotating base plate instead of having a rotating print head. Once this is integrated into the current 5-axis setup the 5-axis Gcode software will be written and tested on the printer. Then the linerless pressure vessel manufacturing will be built up step by step, starting with simple cylinders and ending with a threaded pressure vessel with multi angled overwrap layers. Once this process is worked out, several specimens shall be manufactured with varying parameters, and improvements like adding internal spun lines, in order to test them with applied internal pressure.

4

Hydrogen Permeability Testing of Additively Manufactured Liquid Crystal Polymers

In order to quantify Liquid Crystal Polymers (LCP) for their use as a barrier against hydrogen gas the permeability coefficient should be evaluated. As presented in subsection 2.2.4 the hydrogen gas permeability of the specific LCP Vectra is known from the supplier [19]. However this value has been obtained from test samples that were procured from solid pieces of Vectra. The current unknown is how the permeability is altered by additively manufacturing a specimen from the bottom up. By the layer-wise deposition of individual print lines many interfaces between the solid print lines are introduced in the material, which could each serve as a possible gas transmission path. Thus it is inevitable that additively manufactured Vectra is tested against hydrogen permeability.

Furthermore the results of this test allows this material to be compared to the permeability of other common polymer liner materials in pressure vessel applications. From this comparison the material can be classified as a potential candidate for linerless pressure vessels if the permeability is of a sufficiently comparable level with respect to other state of the art liner materials. Furthermore from the results of the permeability tests certain requirements can be set up for designing pressure vessels with the goal of storing gaseous hydrogen.

The testing method that will be used for testing the permeability of additively manufactured LCP is presented in section 4.1. Following the explanation of the testing method is the design of the specimens in section 4.2. The results of the permeability tests are presented in section 4.3 and discussed in section 4.4, following this discussions the implications for pressure vessel designs are considered in section 4.5.

4.1. Permeability Test Method

The ASTM D1434-92 test standard [14] can be used to test a potential barrier material for its permeability coefficient for a specific permeate gas. B. Murray [7] proposes an updated version of this test standard, replacing the measurement of the permeated gas with a pressure transducer instead of a liquid slug indicator, which is also reported by Flaconnèche et al. [15]. Apart from this change the same methodology from the ASTM standard is applied. The tests are performed by the Netherlands Organisation for Applied Scientific Research (TNO), the test setup is shown in Figure 4.1. The screw, on to which a specimen is placed, will be fitted inside the top section of the large cylindrical pressure vessel.

With this test setup a flat specimen is placed in between two pressure chambers, sealed with two O-rings on each side of the specimen. The upstream chamber, the large cylinder at the bottom of Figure 4.1, will be filled with the testing gas at the testing pressure and temperature, while the downstream chamber, labelled as permeate vessel in Figure 4.1, will be evacuated to a vacuum before hand. Once the upstream chamber has reached the desired temperatures and pressures the downstream chamber

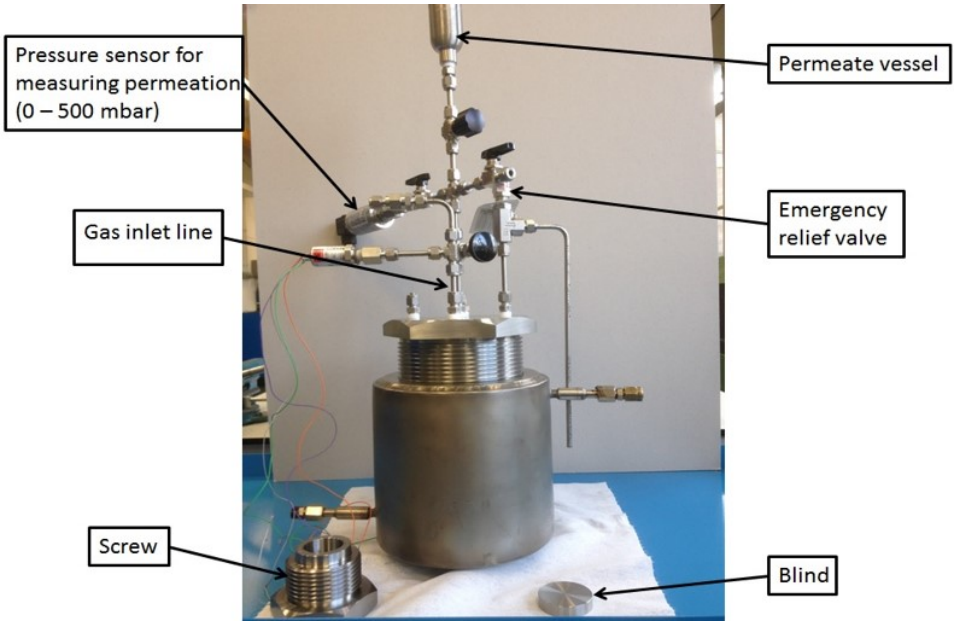

Figure 4.1: The permeability testing setup of TNO [41]

pressure and temperature will be recorded over an extended period of time. The pressure increase on the downstream side can be used to obtain the permeability coefficient. Initially the pressure in the downstream chamber will increase non linearly, which is called the transient region, after a certain amount of time the pressure increase reaches a constant steady state rate. From this steady state pressure increase two time points are taken, one at the start of the steady state region and one at the end, labelled time point one and two. The equivalent volume at standard pressure and temperature is then obtained at both time points, from which the volumetric leak rate is calculated. With the leak rate, pressure difference and specimen thickness the permeability coefficient $[scc \cdot m/m^2 \cdot s \cdot bar]$ is obtained, following Equation 4.1. With Δp indicating the pressure difference $[bar]$ applied over the specimen, and x representing the average specimen thickness $[m]$. [7], [9], [14], [15]

$$P = \frac{LR}{\Delta p} \cdot x \tag{4.1}$$

Where $LR =$ Leak Rate $scc/s \cdot m^2$, as defined by the difference in equivalent volume $[scc]$ at time point one and two per unit time and area, following Equation 4.2. Where p_{STP} and T_{STP} indicate the standard temperature $[K]$ and pressures $[bar]$, furthermore the pressures $[bar]$ and temperatures $[K]$ at the specific time points $[s]$ t_1 and t_2 are indicated by p_1,p_2,T_1 and T_2, V represents the volume $[m^3]$ of the permeate chamber and A is the working area $[m^2]$ of the specimen in the test setup.

$$LR = \frac{V_{eq,2} - V_{eq,1}}{(t_2 - t_1) \cdot A} = \frac{\left(\frac{p_2 V T_{STP}}{P_{STP} T_2}\right) - \left(\frac{p_1 V T_{STP}}{P_{STP} T_1}\right)}{(t_2 - t_1) \cdot A} \tag{4.2}$$

The tests will be performed with pure gaseous hydrogen at a pressure difference of 300 bar. This pressure was chosen as it is close to the industry standard of 350 bar, as well as being within range of the possible testing pressures of the test setup. The specimens will remain in the test setup for several days, depending on technician availability and if the permeability of the specimen is low enough to prevent large amounts of gas too flow through. If the specimen allows gas to leak through the pressure in the vacuum side of the test setup will increase very quickly, in the order of minutes, resulting in the test being halted. However if the specimen provides a sufficient barrier against the gas the test can run for days until enough gas has leaked through to take measurements.

4.2. Design of Specimens

The testing method outlined in the previous section requires flat specimens for testing. For the current investigation these specimens will be manufactured from additively manufactured LCP. Due to the layered line-wise build up of these specimens the configuration of the layers, in terms of thickness, orientation, line width etc. will have an effect on the macro and microscopic properties of the specimens. With the limited resources for testing with this permeability testing method an effective preselection of these aforementioned printing variables should be made to efficiently utilise the available permeability testing resources. The following section will delve deeper in the preselection of the manufacturing variables of these specimens and the resulting designs to be tested.

4.2.1. Fused Deposition Modelling Manufacturing Variables

Several variables of Fused Deposition Modelling (FDM) can be changed and altered in order to affect the layer-wise architecture of an additively manufactured specimen. These variables are investigated in order to find the optimal combination of variables to maximise the barrier properties of a specimen. The variables which are investigated are:

- Layer height - The height of the print layers
- Extrusion multiplier - This multiplier changes the amount being extruded, to account for over- and under- extrusion
- Printing temperature - The temperature of the heating block and nozzle on the extruder
- Print line orientation - The orientations of the print lines in the different print layers
- Print layer stacking sequence - The stacking of the different print layers
- Annealing - A post treatment option to increase the chemical bonding between adjacent print lines

Layer height

As presented in section 2.2 and in the work of Gantenbein et al. [3] the layer height has a substantial effect on the mechanical properties of the print lines. With the mechanically optimal layer height, feasible on the Ultimaker 2+ FDM printer to be used for these specimens, being 0.05mm. Furthermore to prevent the passage of molecules, lowering the layer height means that more layers will be present in a specimen of a specific thickness. With more layers more barriers for a gas passage can be created, combined with the other variables discussed next. On the other hand, decreasing the layer thickness means that printing will be increased, something that is not limiting for these relatively small specimens but needs to be kept in mind for long term applicability and development of this technology.

Extrusion multiplier

The extrusion multiplier of a printing sequence is a multiplier added on top of the standard calculations made to find the amount of material that is extruded per print move. In a nominal situation this multiplier is set to 1.0, then the amount of material being multiplied is equal to the cross sectional area of the print line and the length of line being printed for a move, which is finally also adjusted for the amount of filament coming into the nozzle. However in some cases this value might cause over- or under-extrusion of a print line. One way to mitigate these phenomenons is to adjust the extrusion multiplier. Furthermore this multiplier can also be used intentionally to create a over- or under- extrusion print. As presented in the work of C. Houriet [20] intentionally over extruding can lead to an interlocking swirl pattern. This swirl pattern could be a very strong candidate to prevent gas molecules from passing between and around print lines, as adjacent print lines are mechanically interlocked with a complex swirling pattern resulting in a very complex path for gas molecules to pass through.

Printing temperature

With the printing temperature many things can change in the resulting print quality. If the printing temperature is too low, the material barely melts or in extreme cases doesn't even melt. This will prevent extrusion from occurring. With a too high printing temperature the material will degrade and not maintain is desirable mechanical properties. In between too cold and too hot there is also the possibility to affect the mechanical properties of individual print lines and the adhesion between print

lines. The hotter the print line being printed the better it will adhere to adjacent lines as the interface could still be above the melting temperature. With lower printing temperature, but of course still above melting temperature, faster cooling of individual print lines is achieved, resulting in more anisotropic mechanical properties as the aligned micro structure is frozen in. [3]

Print line orientation and stacking sequence

Apart from affecting the large scale structural properties of a part or specimen by varying the print line orientations in a part, it is allows to complicate the gas molecule path through the specimen. Alternating print line orientation in subsequent layers will decrease the locations where the interfaces between print lines build up above each other in subsequent layers. However if adjacent layers have the same print line orientations, this can also be achieved by offsetting the print lines of one layer with half a print line width with respect to the other layer, resulting in a brick and mortar type cross section. This will also greatly impede gas molecule movement, as above every interface between two print lines the centre of the print line in the subsequent layer is located.

Annealing

With annealing a post condensation reaction occurs in the LCP, which increases the bonding between adjacent print lines. As has been shown by the work of Gantenbein et al. [3], this increases the transverse tensile strength transverse of specimens printed with straight parallel lines and tested in tension 90 degrees with respect to the print line direction. Which indicates increased print line and layer bonding and interlocking. This is hypothesised to also increase the barrier properties of a printed specimen, as it reduces the possibilities of gas molecules passing between print lines.

4.2.2. Fused Deposition Modelling Manufacturing Variables Investigation

The variables presented above were individually investigated by making rectangular specimens, Figure 4.2, that were cut in half and prepared for microscopy, Figure 4.3, in order to observe the variable under investigation in the cross section of the specimen. The variable investigations are further detailed below. The most important aim of this investigation is to make the paths for gas molecules to pass through the material as difficult as possible. In section 2.2 the LCP bulk material itself is classified with excellent barrier properties, which means the main focus is to prevent passage of the molecules between and around print lines.

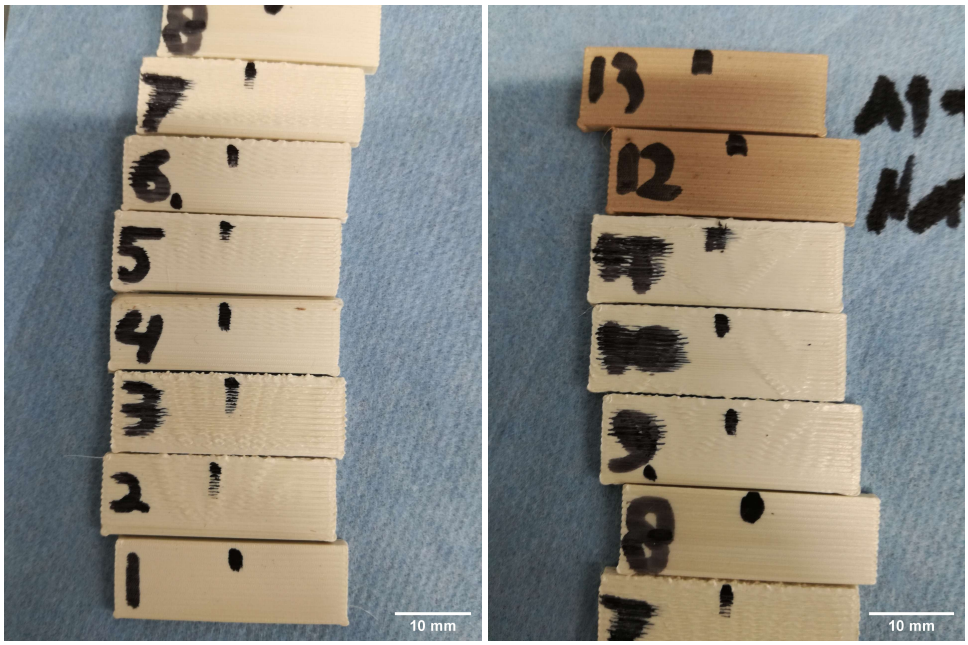

Figure 4.2: One set of LCP microscopy specimens. Each specimen was cut in half along the length direction, potted in epoxy and polished for microscopy cross section observation. Number 12 and 13 are annealed.

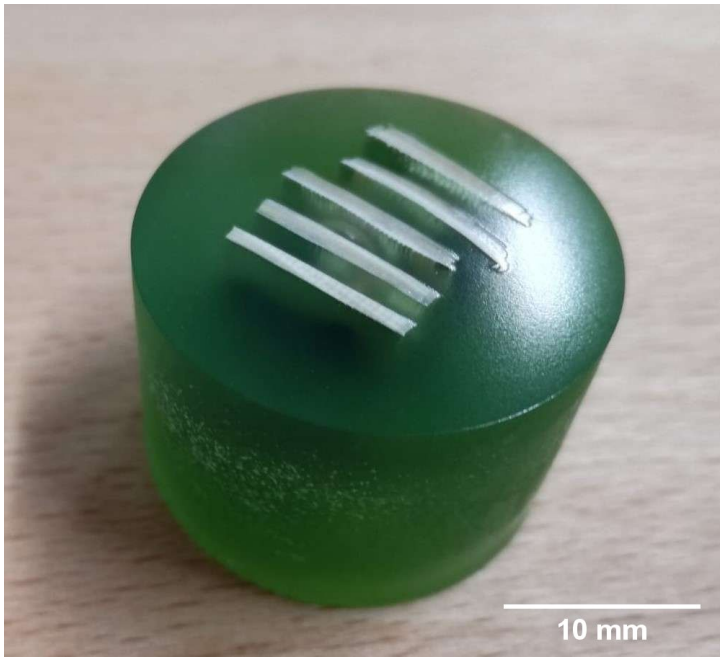

Figure 4.3: LCP samples have been potted in epoxy and polished for microscopy observation.

Layer height

Microscopy specimens were manufactured with different layer heights to observe the effects of the layer height on the cross section. In an example is shown of two cross sections with varying layer height, Figure 4.4a having a layer height of $0.05mm$ and Figure 4.4 having a layer height of $0.15mm$. From these cross sections the observation can be made that the choice of layer height does not affect the cross section in any other way than defining the number of layers in a sample. However in some specimens delamination occurs, this occurs more often in samples with a higher layer height than with samples with a lower layer height. This can not be directly correlated as also other variables were changed in these sample. From these specimens the conclusion can be made that the lowest layer height used of 0.05mm provides consolidated specimens that can be readily used for further testing. Coupled with the fact that a low layer height provides more potential for introducing barriers for gas molecules to pass through, this leads to the conclusion that a low layer height of 0.05mm shall be used for the permeability specimens.

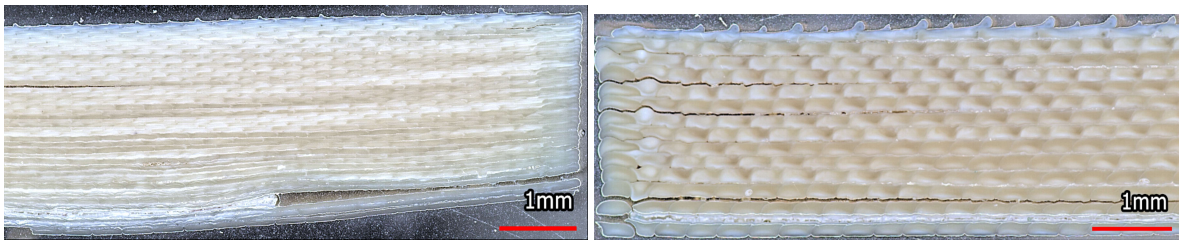

(a) Specimen B1, layer height of 0.05mm (b) Specimen B3, layer height of 0.15mm

Figure 4.4: Microscopy images of LCP cross sections, 40x magnification

Extrusion multiplier

Various different extrusion multipliers were used in the microscopy specimens, the main goal of these settings was to investigate the overextrusion swirling pattern observed in the cross sections. Ideally this pattern should be stable throughout the cross section and not escalate through the thickness. In the specimens of Figure 4.5 the effect of the extrusion multiplier can clearly be seen, with higher values a large escalating overextrusion effect is present, whereas with lower extrusion values the cross section

shows a stable layer pattern without overextrusion. Unfortunately it was not possible to calibrate this setting to consistently obtain a stable overextrusion pattern. The threshold where these swirls are present without escalating through the thickness is very small. With the varying external factor of the filament diameter the actual volumes being extruded are not consistently following the volume set in the Gcode. With the current setup this can not be accounted for, as such it is not possible to create the permeability specimens with consistent stable overextrusion swirls. This feature could potentially be obtained if the filament diameter is very accurately measured over the entire length of filament being used for extrusion and fed back into the printer to adjust the extrusion volume in real time.

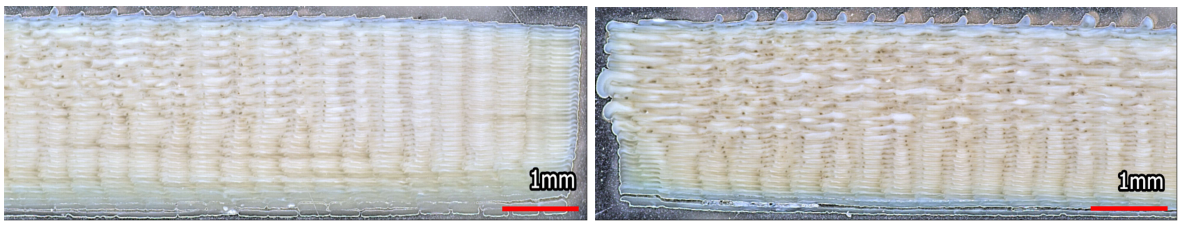

(a) Specimen B4, 105% extrusion (b) Specimen B5, 110% extrusion

Figure 4.5: Microscopy images of LCP cross sections, 40x magnification

Printing temperature

The printing temperature was not varied and tested in the microscopy samples. The choice was made to print all samples at 295 °C, because at this temperature the maximum mechanical properties are obtained [3]. If sufficient permeability can be obtained at this temperature this also means that this can still be combined with maximum mechanical properties.

Print line orientation and stacking sequence

Due to the fact that the microscopy specimens were manufactured with perpendicular cross sections of the printed specimens different print line orientations were not tested in the specimens. As with different orientations it would not be possible to inspect the cross sections of all the print lines, as the lines not perpendicular to the cross sectional cut will not have a visible cross section. However specimens were manufactured and analysed with the brick-and-mortar type cross section, Figure 4.4b. These specimens show the effective nature of the brick-and-mortar cross section and the stable presence of this feature in the cross section. With this feature a potential gap between two print line is immediately blocked by the next layer on top. Whereas if this feature was not present potential gaps between print lines will stack above each other and leave a clear path for gas molecules to penetrate through. From this investigation it is clear that these features can be implemented consistently in manufactured specimens, and will theoretically help the barrier properties of a specimen, as such it is included in the permeability specimens.

Annealing

Finally some microscopy specimens were annealed for 60 hours at 270 °C, Figure 4.6. These specimens underwent a colour change from annealing, colouring brown from the original yellowish LCP colour. From the cross sections of these specimen it can be seen that the colour change only penetrated 0.05mm inwards from the surface of the specimen. As the colourisation is theorised to be from the post condensation reaction [3], the further inward material requires more time to undergo the annealing reaction due to the diffusion of gasses away from the material. Any increase in inter print line adhesion can not be obtained from the cross sectional investigation.

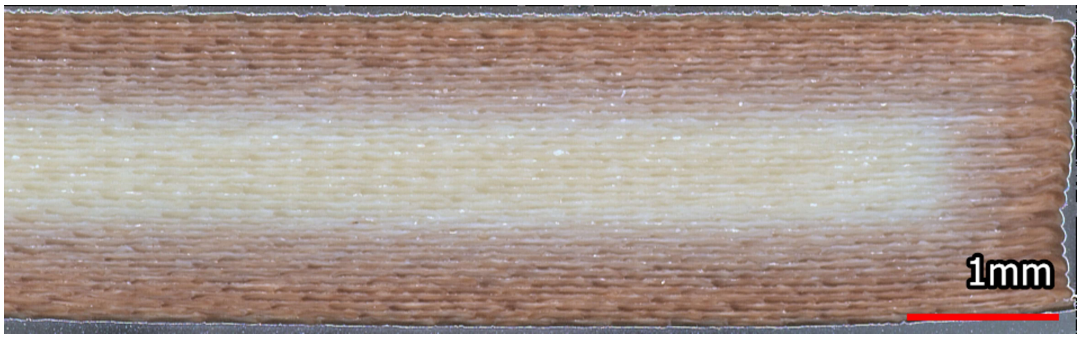

Figure 4.6: Microscopy images of LCP cross sections, 40x magnification. This sample has been annealed, where the darker colour in the cross section indicates the area to which the post condensation reaction has penetrated from the outside.

From this hypothesis the decision has been made to anneal the permeability specimens to maximise the barrier properties of the specimens. However some un-annealed samples will also be manufactured to have them ready to test if extra availability of the testing setup is present after the nominal testing campaign. In order to also test the feasibility of un-annealed LCP as a barrier material. With the driving reason being that larger complex pressure vessels will require more effort to anneal, mainly to guarantee the geometrical stability, furthermore it will require large amounts of energy to heat and anneal the pressure vessels. And lastly annealing reduces the recyclability of the pressure vessels, which is a very unique feature of the proposed LCP pressure vessels. In conclusion, the nominal test campaign is performed with annealed specimens to maximise barrier properties, with extra un-annealed specimens to test if possible in order to asses the difference in permeability between un-annealed and annealed specimens.

4.2.3. Manufacturing Variables Specimen Design

From the investigation in the previous subsection the following manufacturing variables are selected for the specimen manufacturing:

- Layer height - 0.05 mm
- Line orientation - [0/0/90/90]
- Layer stacking - brick and mortar
- Annealing - 270°C for 110 hours

Six specimens shall be tested with the same manufacturing variables in order to find statistically significant results. However nine specimens will be manufactured, from which the six with the best surface finish will be selected for testing. This is to maximise the sealing potential of the -ring in the test setup with the surface of the specimen. If the interface between the O-ring and the surface of the specimen starts to leak this will adversely affect the measured leak rate by increasing the leak rate to above what would be present if only the leakage through the specimen was measured. This selection of the best six specimens from the nine manufactures specimens is thus only present to remove specimens that would show a worse than ideal interface between the specimen and the test setup, while not selecting on the quality of the specimens themselves.

Furthermore several extra specimens shall be manufactured without annealing at a such that if at the end of the nominal test campaign there is still the possibility of testing extra un-annealed specimens. The results of these small amount of tests could indicate the effect of annealing, however most likely not enough specimens can be tested to show this effect with any statistical significance.

4.2.4. Geometry Requirements for Test Method

The specimens to be manufactured will have to fit tightly into the testing apparatus, and as such have to adhere to the following requirements:

- Diameter: 49.95 ±0.05 mm
- Thickness: 1-20 mm
- Surface finish: As flat as possible

As the thickness can be adjusted for within the test setup it has a range of between 1 and 20 mm. However the specimen should have a constant thickness and be as flat as possible to seal the specimen between the two O-rings. As specimen thickness is taken into account in the permeability coefficient equation, Equation 4.1, the choice for specimen thickness will be made for manufacturing, handling and testing reasons. First of all making a thicker specimen will increase the manufacturing time, as well as increase the testing time as it will lower the leak rate with increasing thickness. On the other hand if the specimen is made too thin it will not be stiff enough for proper handling and it will have a higher leak rate. After evaluating the stiffness and handling of several different thickness parts additively manufactured from LCP by hand the specimen thickness was chosen to be 2.0 mm. This thickness will provide sufficient stiffness for the specimen to be handled and clamped in the testing setup, as well as not too increase the manufacturing and testing time to very high durations.

The surface finish of a flat specimen manufactured with FDM will have one side facing the build and one side facing the air above the part. The side facing the build plate will have the same surface finish as the build plate, which in the case of these specimens is an Ultimaker 2+. The build plate of this printer is a very flat glass plate, therefore the side of the specimen facing the glass plate will have the same flatness as the glass plate. The surface finish of the other side of the specimen will be dependent on the quality of printing. However if this side is placed in the test setup facing the vacuum chamber and the build plate side of the specimen is placed against the high pressure chamber then the more critical O-ring interface will be placed on the build plate side of the specimen. As the O-ring on the side of the high pressure side will have a more significant effect on sealing the specimen than the other side, because it will prevent any of the high pressure gas from flowing around the specimen.

4.2.5. Summary of Specimen Design

The following list summarises the design of the LCP specimens to be tested for hydrogen permeability

- Printing temperature = 275 $^{\circ}C$
- Nozzle diameter = 0.4 mm (Which equals to the print width of the print lines)
- Layer height = 0.05mm
- Layers = 40 (sample thickness = 2.0mm)
- Stacking = $[0/0/90/90]_N$, with every second layer of the same orientation offset perpendicular to the print line direction by half a print width
- Diameter = 49.95mm

With this design nine specimens will be manufactured for permeability testing that will be annealed, from these nine the six specimens that have the best sealing in the test setup will be tested. Additionally two specimens will be manufactured that are not annealed, such that they can be tested if there is remaining testing capacity after the first six tests are completed.

4.3. Permeability Test Results

After the test concluded for a specimen a data set with applied pressure (P vessel), temperature of test vessel (T vessel) and the pressure of the permeated hydrogen (P permeate) were recorded and extracted. In Figure 4.7 this data set for specimen two has been plotted, the remainder of the specimen data is presented in Appendix A. Note that the units for the Y-axis value of each curve on the plot are labelled in the legend on the right.

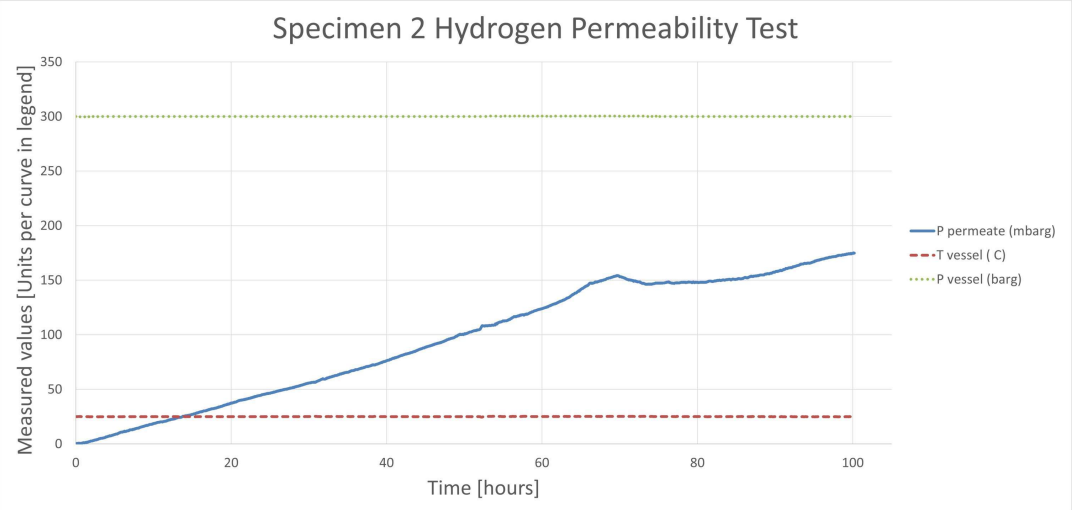

Figure 4.7: Unprocessed Results of Gaseous Hydrogen Permeability Test of Specimen 2

In Table 4.1 the processed results of all the tested specimens are presented. The data gathered from each test was processed following the method described in section 4.1. As is clearly visible in the table all specimens except specimen number three show permeability values in the range of 10^{-7}. Specimen three can be identified as an outlier, which will be confirmed by visual examination of the specimens after testing. The specimen numbers in the table reflect the fact that the six best specimens from a set of nine were tested. Furthermore the last specimen, specimen "B", was the only un-annealed specimen successfully tested. Another un-annealed specimen, specimen A, was also tried in the test setup, but it did not seal or it had a leak in the specimen. This test showed that the applied pressure was rapidly decreasing, indicating a leak in the specimen or test setup with the specimen included, ultimately resulting in the test being terminated.

Specimen 2 after testing is presented in Figure 4.8. First of all on the front side an indentation is present that coincides with the location of the O-ring in the test setup. Because of the large applied

Specimen number:	Permeability: $[cm^3/m \cdot s \cdot bar]$
2	$2.04 \cdot 10^{-07}$
3	$3.22 \cdot 10^{-05}$
5	$1.79 \cdot 10^{-07}$
6	$2.07 \cdot 10^{-07}$
8	$1.02 \cdot 10^{-07}$
9	$1.50 \cdot 10^{-07}$
B	$1.03 \cdot 10^{-07}$

Table 4.1: Permeability testing results of additively manufactured LCP specimens. With outlier number 3, and un-annealed specimen B.

pressure differential on the specimen the O-ring formed an indentation in the material. On the back side a similar pattern is visible, however this is also coinciding with the silicone ring that sits against the O-ring on this side of the specimen. Furthermore on the back side in the very centre of the specimen a circular indentation is present, this coincides with the centre hole of the support disk in the test setup. This support disk is filled with holes of the same diameter as the indentation on this specimen. Because of the large pressure difference acting on the material the steel of the test setup caused a deformation on the specimen. Pictures of the remainder of the specimens are presented in Appendix A.

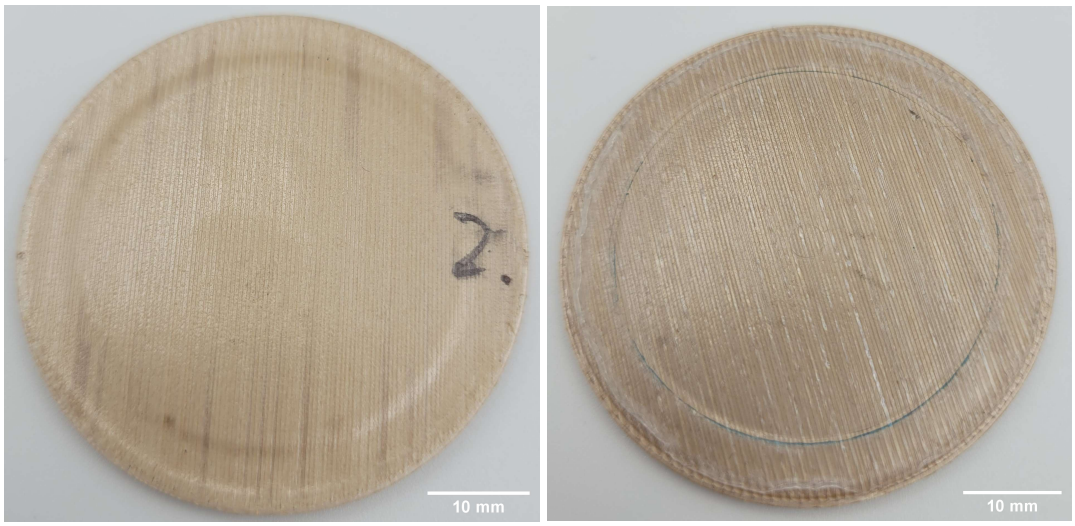

(a) Front side (b) Back side

Figure 4.8: Permeability specimen number 2

Specimen 3 was indicated to be an outlier due to the large difference in permeability value as compared to the other six results. However when looking at the specimens in their state after the test, Figure 4.9, no difference in the surface of the top and bottom of the specimen can be seen as compared to the other specimens presented in Figure 4.8 and Appendix A. This could mean that either the specimen showed leakage around the O-rings in the test setup or it had a insufficient printing quality inside the specimen resulting in fast permeation though the sample.

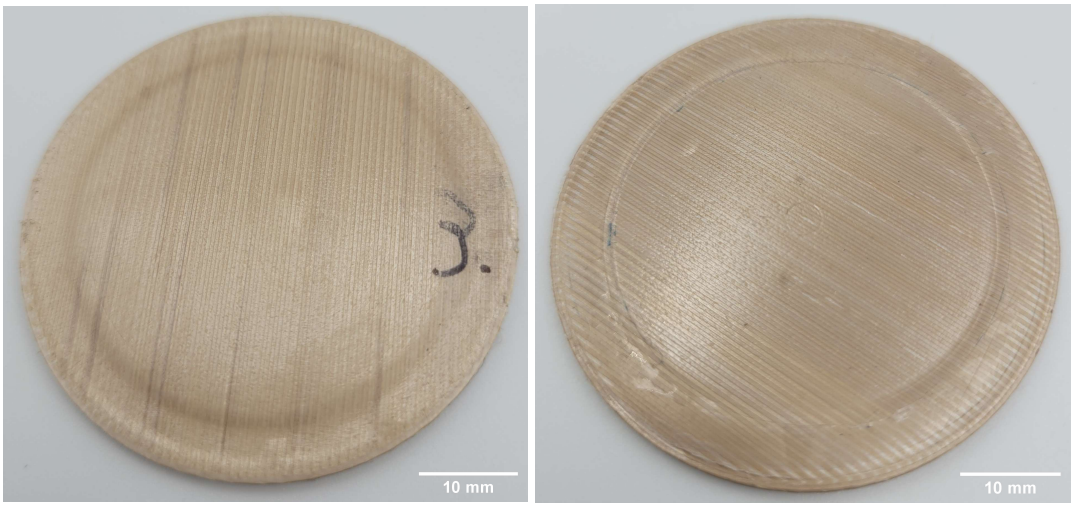

(a) Front side (b) Back side

Figure 4.9: Permeability specimen number 3, picture taken after hydrogen permeability testing

4.4. Discussion of Permeability Testing Results

With the results presented in the previous section LCP manufactured with a FDM printer can now be classified in its hydrogen permeability properties and compared against other common polymer liner materials. First of all the additively manufactured LCP can be compared against its permeability performance as a bulk material. From the LCP Vectra datasheet of Celanese [19] the hydrogen permeability of the bulk material is presented as $4.51 \cdot 10^{-08}$, which is between 2.0 and 4.5 times lower as the values presented in Table 4.1, excluding outlier specimen number three. For a processed material, and especially an additively manufactured material, this is a reduction in permeability properties that can be accepted. It still remains within one order of magnitude of the bulk properties, and especially when comparing to similar polymer liner materials the permeability values reported in Table 4.1 are still competitive. To effectively compare additively manufactured LCP to other common polymer liner materials it is also of interest to include the mechanical and density properties of all the materials. In Figure 4.10 the data from Table 4.1 and other common polymer liner materials are compared to each in permeability and specific stiffness.

When looking at the data presented in Figure 4.10 it is clear that the hydrogen permeability values of additively manufactured LCP are within the low end of the range of common liner polymers. Furthermore, when also considering specific stiffness, LCP in it's additively manufactured form outperforms all of the common liner polymers. Further validating the strength of this material as a candidate material for linerless pressure vessels. As the specific stiffens of the LCP reported in the graph is that of additively manufactured LCP lines, taken from the work of Gantenbein et al. [3], and not complete parts as a whole, it also remains possible to greatly improve the total structural efficiency of an additively manufactured part through structural optimisation. Whereas this is not possible with any of the other materials presented in the graph, as these do not present the anisotropy in the print lines that additively manufactured LCP shows.

Finally the one test results of an un-annealed specimen shows a permeability value within the range of the annealed specimens. This indicates that not annealing additively manufactured LCP could still produce parts that have sufficient hydrogen permeability. Although only specimen without annealing has been tested it is not yet possible to have a strong conclusion on this phenomenon, to fully conclude that this would be the case more un-annealed samples should be tested.

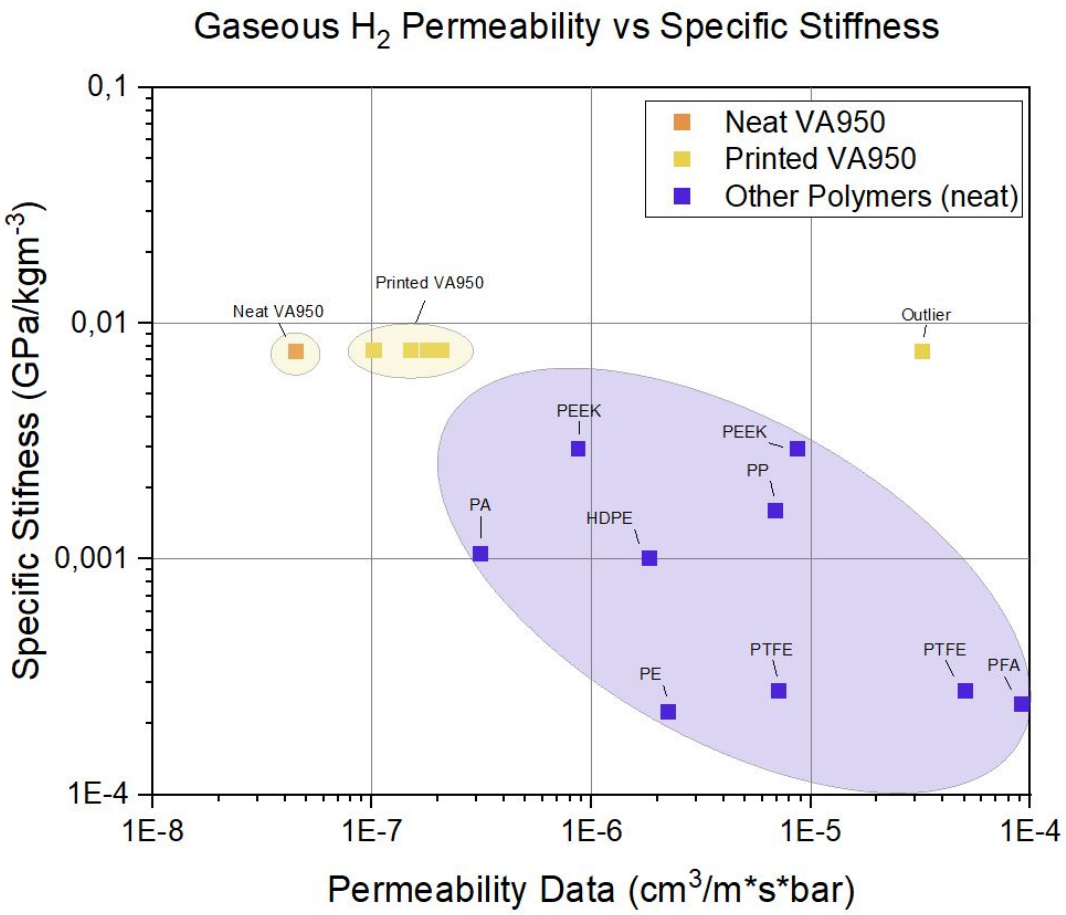

Figure 4.10: Ashby graph of hydrogen permeability samples and common liner polymer materials, comparing permeability and specific stiffness. References of data[1]

4.5. Implications for Designing Additively Manufactured Pressure Vessels

With the results presented in section 4.3 and section 4.4 it is evident that additively manufactured LCP can be used as a hydrogen barrier material. Furthermore with the excellent anisotropic mechanical properties present in the additively manufactured form, the potential for structural optimisation can lead to efficient pressure vessel design. Some key takeaways from the present investigation of hydrogen permeability of additively manufactured LCP for the design of pressure vessels are presented below.

First of all taking the mean hydrogen permeability value of the specimens tested from Table 4.1 will be a good starting point for the the design of a hydrogen pressure vessel. This mean value of $1.68 \cdot 10^{-07} [cm^3/m \cdot s \cdot bar]$, excluding outliers and annealed specimens, can be used to calculate the required wall thickness for the applied pressure differential of gaseous hydrogen in the pressure vessel for an allowable leak rate requirement. This leak rate requirement can be governed by the mission requirements of a pressure vessel, like required time to hold a certain mass of gaseous hydrogen without it leaking out. Or for example environmental requirements regulating the maximum amount of gaseous hydrogen leaking out and mixing with the air, in order to prevent a combustive mixture from occurring in the surrounding enclosed volume of air around the pressure vessel.

[1] H2 Permeability values: HPDE,PE,PA,PEEk,PP,PTFE [8], PFA, PEEK, PTFE [7], also presented in Table 2.1.
All values for specific stiffness of the reference polymers are obtained from MatWeb.
H2 Permeability and specific stiffness of Celanese LCP is obtained from [19]. H2 Permeability of printed LCP are obtained from the experimental results of Table 4.1, specific stiffnesses are obtained from classical laminate theory calculations of the layup sequence of the LCP specimens.

Furthermore, from the permeability specimens tested, some other takeaways regarding the design can be proposed for the design of a hydrogen pressure vessel. The key design parameters for maximising the hydrogen gas barrier properties of a part are:

- A low layer thickness, preferably as low as 0.05mm, to maximise the amount of layers a potential gas molecule has to pass through.
- A brick-and-mortar cross section, to prevent any inter print line gaps from stacking on top of each other through the thickness of a wall.
- Using a cross ply orientation in the wall, resulting in perpendicular lines being stacked on top of each other to prevent potential gaps from stacking on top of each other through the thickness.
- Annealing can be used if the geometry of the pressure vessel allows for annealing without compromising the geometric stability of the part. However not annealing a pressure vessel could also result in a sufficient permeability. Although only one un-annealed specimen has been tested and thus the results regarding the effect on permeability are not conclusive, this sample did not show detrimental effects on the permeability.

Finally, from the testing campaign it was still evident that some outliers exist within the specimen range, also considering the specimens that there were not tested because of their poorer sealing capabilities as compared to the tested specimens. This leads to the conclusion that LCP pressure vessels manufactured with FDM will need careful quality control in order to identify vessels posses detrimental defects greatly lowering the hydrogen barrier properties of the overall vessel.

5

Additive Manufacturing of Liquid Crystal Polymer Pressure Vessels

As has been explained in section 2.3, the reasons for applying a five axis printer are quite extensive. In short parts can be manufactured without support material and with print line optimisation with anisotropic material, as well as the fact that pressure vessels can be printed without a separate liner material. The following chapter will detail the development of the 5-axis printer used for this project, and the design and development of the printing process itself.

5.1. 5-Axis Additive Manufacturing of Pressure Vessels: Process Design

Traditionally 3-axis Additive Manufacturing (AM) is focused on creating the geometry of a part in a layerwise fashion, where the only structural optimisation is possible inside the flat print lines of planar layers. However with 5-axis AM print lines can be positioned in 3D space, and thus effectively be optimised in all directions. The one limitation is that these print lines will need a support in order to be placed in the location intended, otherwise the material is extruded in mid air and will fall to the ground. So a process should be designed that both allows for any shape to be printed, while also allowing for the structure to be designed with optimised print lines. The following section will describe the designed manufacturing process for pressure vessels.

5.1.1. Separating the Pressure Vessel Liner and Overwrap

The manufacturing process design chosen for the pressure vessels in this thesis is to break up the pressure vessel in a liner and overwrap. Where the liner is used to build up the geometry of the part and provide a supporting function for all subsequent print lines. The overwrap is then printed on top of the liner with structurally optimised print lines. Earlier in this thesis the aim was put forward to produce linerless pressure vessels, and now a liner is introduced back into the design. The main difference between the liner in this process and a liner in a state of the art Composite Overwrapped Pressure Vessels (COPV) is that a state of the art liner is made from a different material than the pressure vessel and thus also manufactured in a separate process. In both cases though they provide the same function, which is to support the subsequent layers of the pressure vessel while it is being manufactured.

In the case of state of the art COPVs the liner also functions as a barrier for the fluid inside the vessel to permeate out through the pressure vessel. In the case of LCP the entire material can serve as a permeation barrier as has been presented in chapter 4. Furthermore due to the manufacturing constraints of the state of the art COPVs and their liners, they are constrained to axis-symmetric geometries. However by manufacturing the liner from the same material (LCP) and within the same freeform manufacturing process (5-axis FDM) a non axis-symmetric pressure vessel geometry can be manufactured.

In Figure 5.1 a schematic is presented of the liner and overwrap split in the printing process. Initially the liner is printed in a continuous spiral from the baseplate to the top of the liner, following the tangent

vector of the liner to allow the new material being printed to have support on the layer below it. When this is finished the printing will shift to a surface normal printing mode, where the subsequent print layers are supported by the liner or any layers deposited on the liner. In this mode any design of the overwrap layer can be printed. For example with lines orientated like filament winding fibres, or variable angle print lines that follow a structurally optimised pattern precisely following the stress field. The possibilities for the optimisation of this overwrap are many and can be a very promising technology.

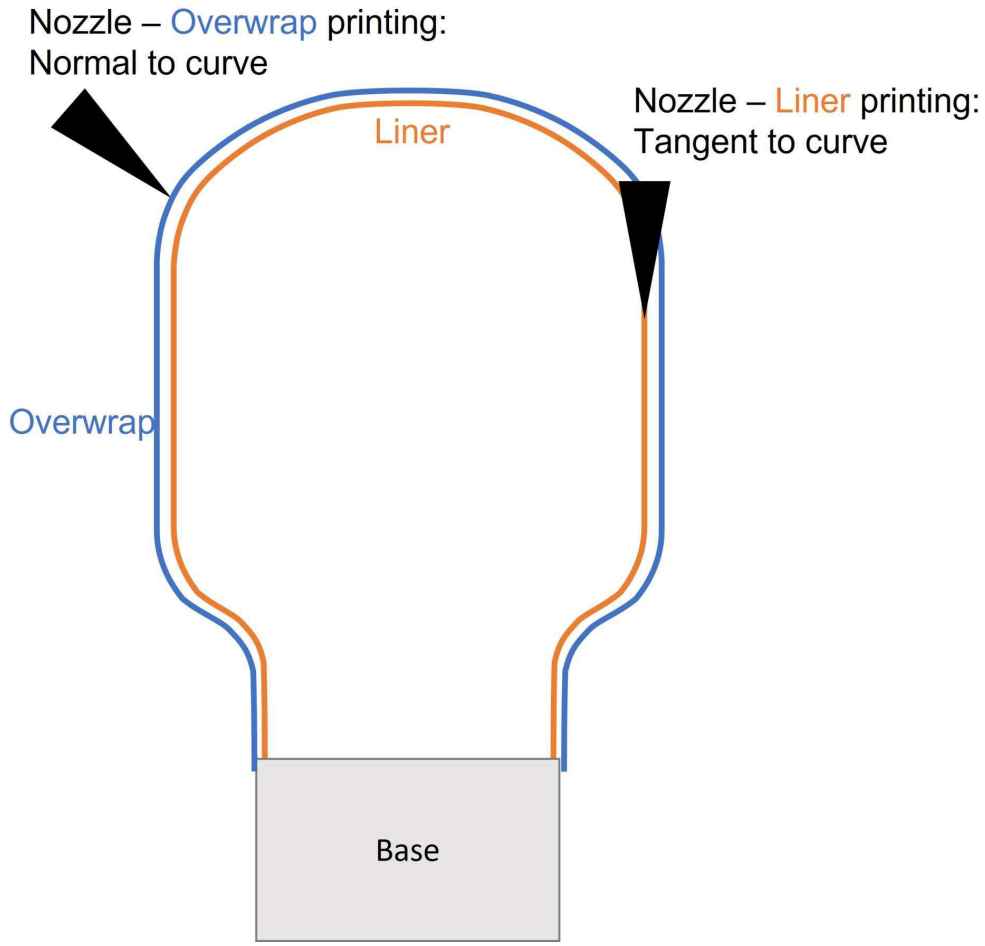

Figure 5.1: Diagram of the split between liner printing mode and overwrap printing mode. When printing the liner the nozzle is tangent to the liner curve in order to deposit the material on the previous liner layer, while for the overwrap the nozzle is normal to the liner and overwrap layers in order to deposit the material on the previous layer.

5.1.2. Integrated Threaded Base

Ultimately these pressure vessels will need to be connected to a pressurised system if they are to be tested or even used in service. This means that in some form a gas tight pressure connection must be integrated into the vessel or be able to connect to the vessel. The solution developed for this thesis is to integrate a female thread into the printed pressure vessels. This was combined with the support feature on which the print would be started and connected to the baseplate, by integrating a male thread into a metal rod fitted in the rotating baseplate, as shown in Figure 5.2. The thread used on this rod was manufactured to be the same thread as the gas connection threads commonly used in the laboratory of the TU Delft Aerospace faculty, which is the 1/4” thread. This threaded rod can then be used to serve as a mould for the female thread of the pressure vessel while also supporting the workpiece for the remainder of the print. As can be seen in Figure 5.2 the thread is located on the end of an aluminium rod with some clearance between the baseplate vice and the threaded section. This clearance has been included to prevent collisions between the print head assembly and the rotating baseplate while

printing in the orientation presented in Figure 5.3.

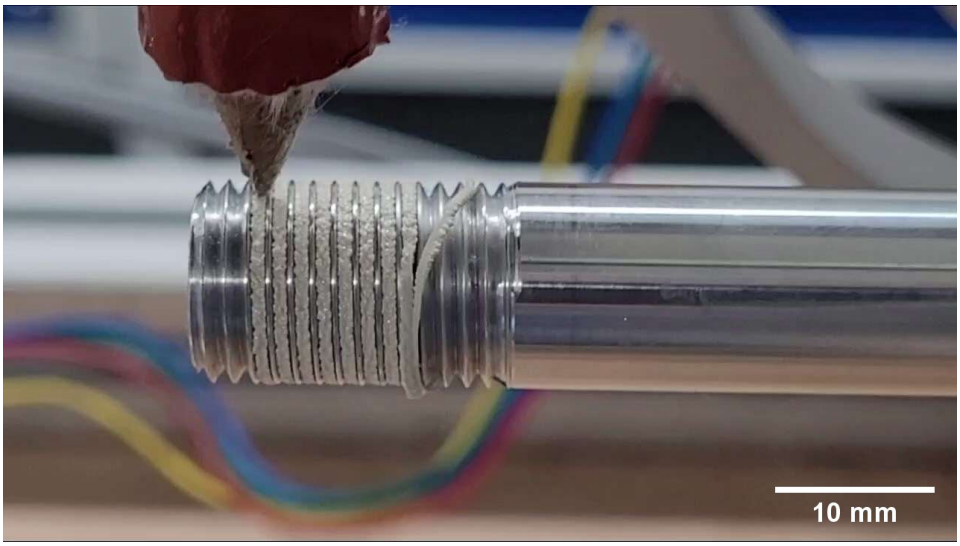

Figure 5.2: Threaded rod as a base for printing

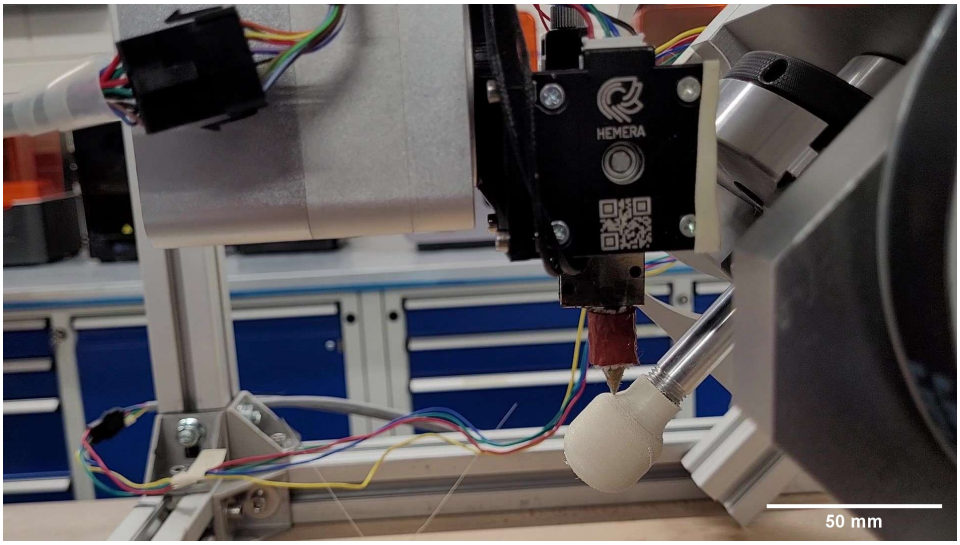

Figure 5.3: Threaded rod length is required to create clearance between the printhead and 3 chuck vice in the printing orientation shown in this figure.

5.1.3. Internal Structures: Spin Printing

Another major advantage of a one step 5-axis AM process is that internal features can be added to the pressure vessels. As has been presented in the literature study in subsection 2.2.5 a promising application of LCP is spin printing, creating very thin fibres with print line direction aligned microscopic crystalline domains [32]. These fibres have shown excellent mechanical properties in tensile loading, and could thus be very effectively used as an internal strengthening mechanism for a pressure loaded structured. As in such a scenario the spun fibres will be perfectly loaded in tension by the applied pressure, as shown in Figure 5.4.

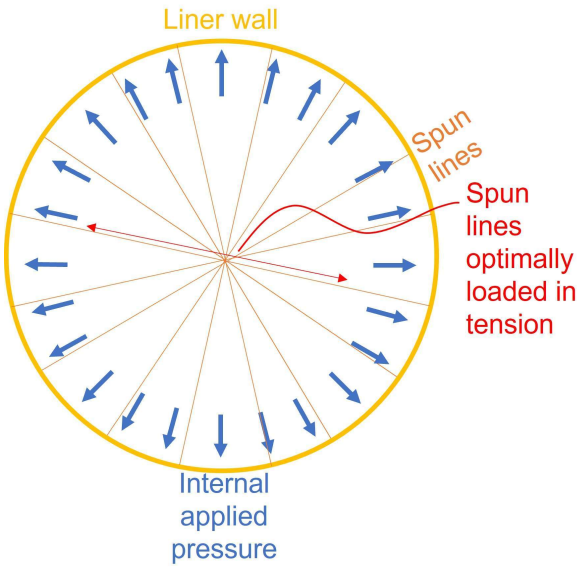

Figure 5.4: Diagram of tensile loading of spun lines when placed as internal structure in a pressure vessel

For this thesis these spun lines have been chosen to showcase the posibilities of adding internal structures to the pressure vessel. Apart from this many other internal structures can be integrated. Adding sections of these spun lines inside the liner could theoretically increase the structural efficiency greatly, as has been shown in a similar case like shown in Figure 2.3 [32]. As these tests have been performed with the same LCP Vectra A950 as is used in the Shaping Matter Lab it can be integrated into the same printing process as the liner and overwrap of the printed pressure vessels. A layer of these spun lines is added between two layers of the liner with a later to be chosen interval along the liner wall.

5.2. 5-Axis Additive Manufacturing Setup Development

In order to manufacture the proposed pressure vessel geometries presented in the previous section a 5-axis FDM printer is required, that has the freedom of movement to create these pressure vessels with nozzle orientations both tangent and normal to the surface of the geometry. This setup consists of a commercially available 5-axis printer which is shortly described in subsection 5.2.1. The modification of this printer with regards to the extruder, nozzle and rotation axes are discussed in subsection 5.2.2 to subsection 5.2.4 respectively. All these modifications allow for the printer to be used for printing the proposed pressure vessel geometries.

5.2.1. 5-Axis Printer

In order to reach the potentials of 5-axis AM mentioned above a printer is required that has two additional rotational axes on top of the three common linear axes, X, Y and Z. One such setup commercially available is the 5axismaker, Figure 5.5. This machine consists of a simple frame built up of aluminium profiles, on this frame three linear Cartesian axes and actuators are provided. With the two additional rotation axes, B and C, being placed on the end of the Z-axis. On the end of the B axis a mounting point for the toolhead is provided. The stock toolheads available are both for subtractive and additive manufacturing. With the machine originally designed for 5-axis Computer Numerical Control (CNC) milling, the subtractive toolhead consists of a spindle with various milling tools. The stock print head consists of a Fused Deposition Modelling (FDM) hotend and extruder for 1.75mm filament and a stock 0.6mm nozzle.

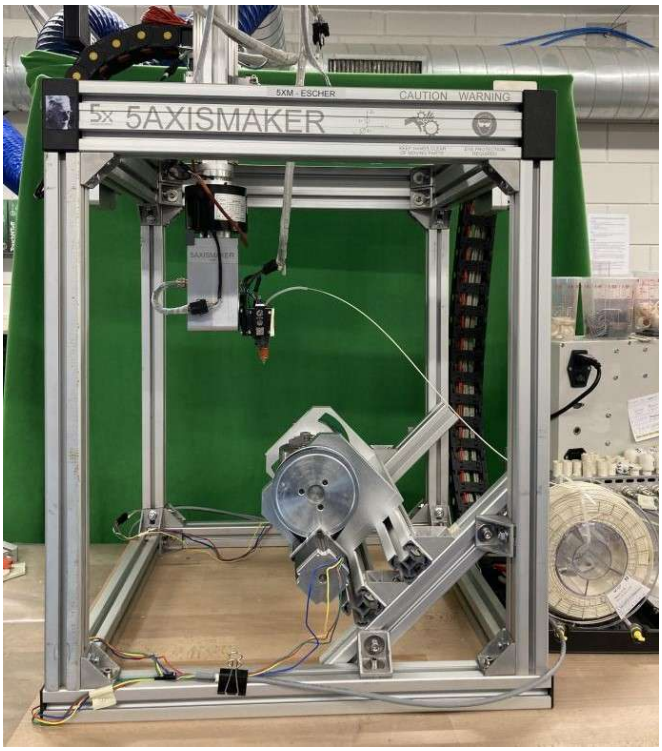

Figure 5.5: The 5Axismaker printer. (Rotating base plate is further detailed in subsection 5.2.4)

5.2.2. Extruder Modification

Within the Shaping Matter Lab (SML), in which this thesis has been performed, there is a lot of experience with FDM of LCP. This experience has mainly been focused on standard 3-axis FDM printers, which showed that using direct drive systems and high temperature hot ends are important for high LCP part quality. The direct drive system means that the extruder motor on the filament is as close to the hotend as possible, whereas other systems have the extruder motor on the frame of the printer and guide the filament through a long bowden tube towards the hotend. With a direct drive there is virtually no lag between the extruder motor moving the filament and that move perpetuating forward to the hot end. Furthermore for LCP printing a high printing temperature is required, of at least 295°C but as high as 340°C. Standard hotends do not allow for such high printing temperatures, which means a special hotend should be selected that does go to these printing temperatures. This is why the 5-axis printer has been fitted with a Hemera extruder, from E3D [42], a direct drive extruder with a hotend capable of print temperatures of up too 400°C.

5.2.3. Nozzle Modification

Another modification made to the printer is the addition of a different nozzle. The stock nozzle and heater block that are part of the Hemera hotend are the E3D V6 Volcano nozzle and heat block. However this combination of nozzle and heatblock have a very large profile in terms of angular clearance, considering the high angle between the nozzle tip and the sides of the extruder assembly. Especially in full 5-axis motion this can lead to a collision between the hotend assembly and a already printed section of the workpiece. The original E3D V6 nozzle can be seen on the top of Figure 5.6.

A way of overcoming this issue is by adding an extended nozzle with a sharper tip angle, supplied

by Non-planar XYZ [43]. As can be seen on the bottom of Figure 5.6, this nozzle has a substantially longer length and thus a lower angular profile as measured from the tip of the nozzle to the sides of the extruder body. This leads to a larger movement space without creating collisions with the workpiece. This nozzle also includes a thin insulation sock to prevent too much heat from escaping on the surface of the nozzle.

Figure 5.6: Comparison of short and long nozzle, top is standard E3D Volcano V6 0.4mm nozzle, bottom is extended 0.4mm nozzle [43].

5.2.4. Rotational Axes Modification

As described previously, the B and C rotational axes of the 5-axis printer are placed on the end of the Z-axis arm, on the print head side. Which is shown on the right side in Figure 5.7. However with the proposed printing process, creating supportless cylindrical pressure vessels in a single production step, it will be necessary to modify this B and C axis configuration. Another possible configuration is to place the B and C axis on the baseplate instead of the print head. Which is shown on the left side in Figure 5.7. This would allow the workpiece to move in two rotation axes instead of the print head. First of all this means that the nozzle is always orientated with the gravity vector. With the original configuration the B axis could turn the print head and thus the nozzle upside down, facing away from the gravity vector. Secondly with the new configuration the workpiece is allowed to rotate infinitely around the baseplate centre axis, the C axis. Whereas with the old configuration this was theoretically also possible, but with the required cabling and filament feeding requirements on the print head this was practically not feasible.

A side by side comparison of the two configuration is shown in Figure 5.7. Here it is clearly visible that, when using the rotating baseplate instead of rotating nozzle, all possible orientations of the nozzle with respect to the workpiece are possible without counteracting gravity, and thus keeping a constant gravity force on the molten material inside the nozzle. Of course the material is ultimately extruded through the pressure build up due to the cold filament being fed into the nozzle and increasing the pressure on the melt, however removing a non constant gravity force from this mix results in a more consistent flow field in the nozzle allowing for a more constant print quality.

The new baseplate axes were mounted inside the frame of the 5-axis printer at a 45 degree angle, as can be seen in Figure 5.8. The reason for this is twofold, rotating in both the positive and negative direction, as indicated in the figure, is required for print moves. The negative direction will be used when printing the top endcap of liner prints, where the nozzle will need to be tangent to the liner curve. This will be described in subsection 5.3.5. Furthermore the positive side will need to be used further than a rotation of 90 degrees to be able to print normal to the fillet surface when printing overwrap layers, which will be described in subsection 5.3.6 and shown in Figure 5.21a. A compromise between these

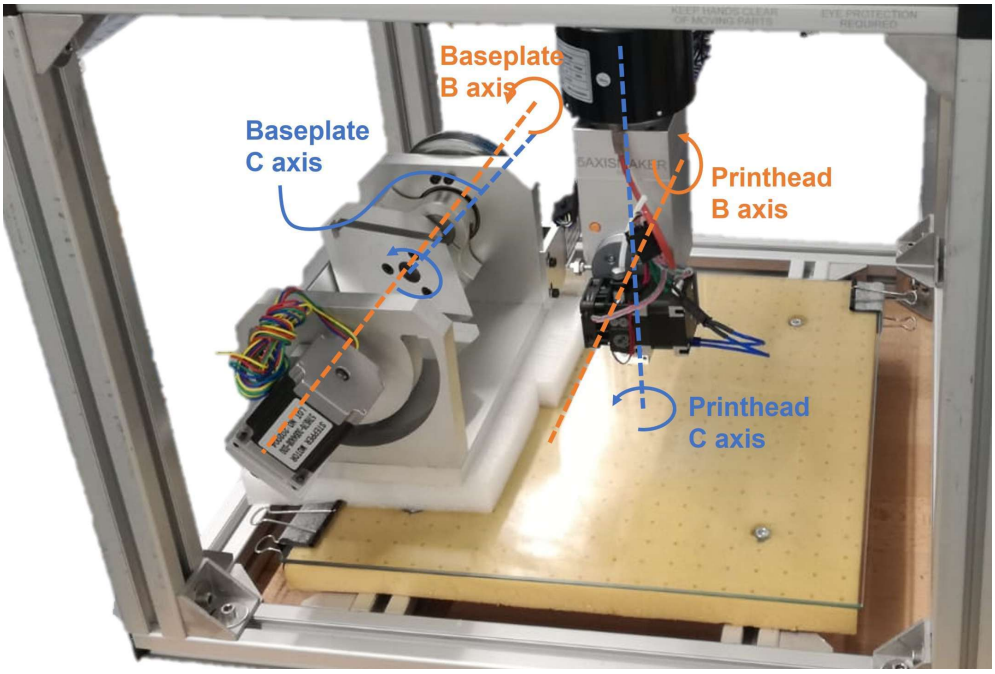

Figure 5.7: The two option for the rotational axes in the 5-axis printer. The stock option has the B and C axis mounted on the Z-axis gantry and thus on the print head side. The new option has the B and C axis mounted on a rotating baseplate.

two requirements was chosen, on both sides the B-axis range is capped, at 135 degrees for printing normal to the fillet, and at -45 degrees for when printing the top endcap of the liner. In both cases the nozzle will not be able to follow the ideal path anymore, but in both cases this deviation is not bigger than 45 degrees. This means that it will still be possible to print all possible print lines without support material requirements.

The electronic actuation of these axis from the 5-axis printer control unit has been taken away from the original B and C axis in the print head. This means that the B and C axis actuators on the print head side are not powered anymore and are thus free to move, although with the internal friction of the motors. This means that the print head can rotate freely even when the 5-axis printer is powered, and thus has the drawback of being able to move after its position has been zeroed in. After swapping the electronic control from the original B and C axes to the new baseplate axes only their actuation settings had to be altered. A calibration routine was performed to dial in the correct steps per minute settings for these particular axes.

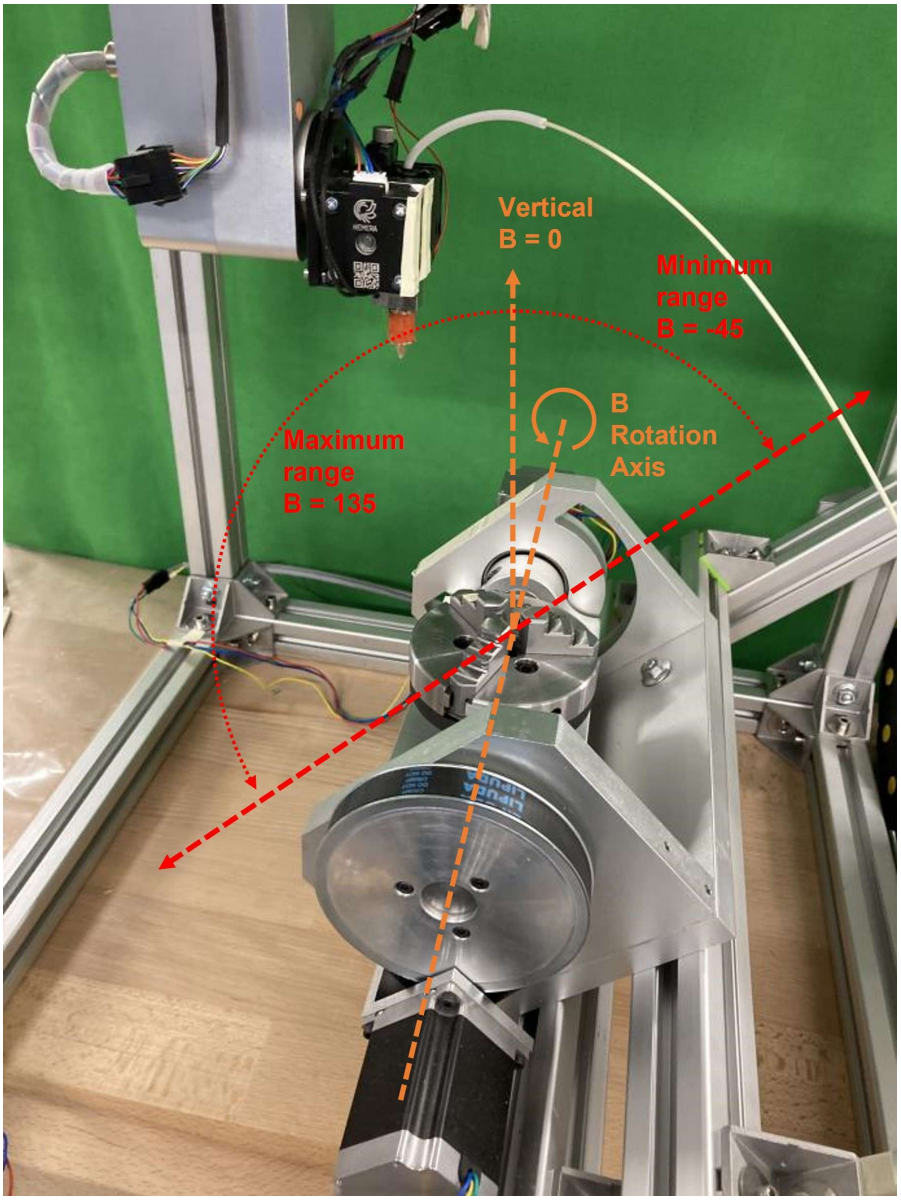

Figure 5.8: Range of motion of the B-axis in the rotating baseplate setup.

5.3. 5-Axis Additive Manufacturing of Pressure Vessels: Process Development

The following section will describe the process of realising the proposed printing process explained in section 5.1. Furthermore the required software development for this transition is explained, as well as a discussion of the development of the printing process for the pressure vessels of this thesis. Starting with printing simple cylinders and building up step by step towards the complete threaded pressure vessel prints. The software used to generate the digital geometry of the parts for printing and to generate the 5-axis Gcode for printing these geometries is the Grashopper package of Rhino 7. Which is a visual node base programming language inside the Computer Aided Design (CAD) program Rhino.

5.3.1. High Level Overview of the Printing Process

In section 5.1 the process of printing a pressure vessel with the 5-axis printer is described. The print starts on the threaded rod by printing a threaded cylinder on this rod. After which the liner is printed

on top of this base cylinder, which is shown in Figure 5.9a. In this printing mode the nozzle follows the tangent of the liner curve, as has been explained in Figure 5.1. The overwrap layers are then printed on top of the liner to complete the desired wall of the pressure vessel, one instanced of overwrap printing is presented in Figure 5.9b. In this image a 90 degree layer is printed on top of a 0 degree layer. In this sequence the nozzle is always orientated normal to the pressure vessel surface at that specific layer.

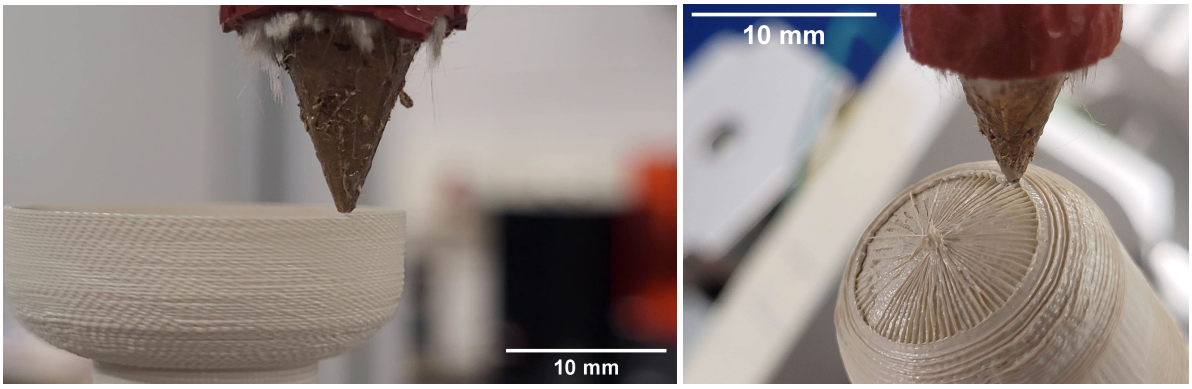

(a) The internal liner layers is being printed, with the nozzle following the tangent of the liner curve.

(b) One overwrap layer is being printed, with the nozzle normal to the vessel surface.

Figure 5.9: Printing of a pressure vessel

While developing the printing process of these geometries many issues and errors occurred, which had to be solved in order to arrive at a working process that ultimately delivers additively manufactured pressure vessels made of LCP. In the following subsection each printing sub sequence and its development will be detailed, ultimately resulting in a successful printing process for pressure vessels.

5.3.2. Generating 5-Axis FDM Gcode

To start the printing process first the digital geometry will need to be transformed into Gcode to be able to be manufactured with a FDM printer. Gcode is the machine language used by most machines for manufacturing, in the case of this thesis this is the 5 axis printer.

3-axis Gcode

The Gcode consists of commands for either moving the axes of the printer or change a setting or parameter. The basic print move for standard Cartesian 3-axis printers consists of a single line of code indicating either the amount of units each axis has to move, or to what coordinate each axes has to move. The units used for this are arbitrary for the machine itself, however in practice these are usually set to mm, inches, degrees etc. Each Gcode line starts with either a G or M command, these commands are a combination of the letter G or M and a subsequent number code. Where G0 and G1 are simple commands indicating that this line is for a print move, whereas other numbers for G and M refer to an operation or setting specific to the machine being used. For example in the Gcode line used for a move from A to B of the print head in a printer G1 would be used, followed by commands for each individual axis and the overall speed. Each individual axes is moved by a command starting with a letter indicating the specific axis, like X, Y or Z, followed by a number indicating the distance to be moved or the coordinate to move. The difference between interpreting a move as a distance or a coordinate is set by another command indicating if it is in relative or absolute mode respectively. The units of an axis move, like X, Y or Z, are usually set in mm or inches. But a user can change these to be interpreted differently by the printer, as long as the Gcode is also the same units as intended. For this thesis all linear axes units are set to mm, whereas rotational axes are set to degrees. After or before the X, Y or Z values a speed is usually also given, this speed is indicated by the letter F in the Gcode line. F is then followed by a number indicating the speed for the move in an arbitrary unit, usually for 3-axis printers this is mm/min. A printer will remember the last value of each axis or speed given and keep it stored until a new value is given. As such a speed value can be given once at the start of a set of moves, while all moves after this will use the same speed value. Apart from the X,Y and Z axes, and the speed F, also a move for the extruder is given in the case of a FDM printer. This is indicated by the

letter E, and is also followed by a number indicating the amount of filament the extruder should move in terms of mm.

5-axis Gcode

In the case of the setup for this thesis, the 5-axis printer will have additional axes to be controlled by the Gcode. These extra axes are the rotational axes on the baseplate or print head, depending on what setup is being used. In both cases these are the B and C axis shown in Figure 5.7. In the Gcode commands these axes are quite simply indicated by a B or C letter followed by the number it should be moved in degrees. Another difference with respect to the standard 3-axis printer Gcode is that the extruder axis is not called by the letter E but by the letter A. This is due to the interpreter software, Mach3 from ArtSoft, using a 6-axis CNC routine to interpret the Gcode. Which use, X,Y,Z,A,B, and C for all the possible axes. As there was no A axis in the 5-axis printer, the A axis was left open to be interpreted as the extruder axes.

Generating 5-axis Gcode: Inverse Kinematics

Gcodes are generated with a digital geometry as input, either as a geometry file, like an .stl, or as a point cloud. With 3-axis AM the Gcode coordinates are easily generated by taking the input geometry, slicing it into layers and taking the points in the print lines of these layers as coordinates for the machine. Possibly some transformation occurs to put the workpiece in the correct location of the printer with respect to the range of the printer axes.

However for a 5-axis printer this process becomes more complicated. The digital geometry coordinates can similarly be translated to the 3 linear axes coordinates, but once either of the rotation axes moves the workpiece coordinate system does no longer align with the Cartesian linear axes of the 5-axis printer. This requires for a 5-axis printer to have additional digital processing steps in order to translate and transform the digital geometry into real world moves of the printer axes. This processing step is called inverse kinematics in the machine motion world, which indicates the transformation of a digital machine move and tool orientation in the workpiece reference frame to the machine axes reference frame.

For each move, coupled to one line of Gcode, this step will be performed. The process starts with the input geometry. Which consists of the digital position data, P_x,P_y,P_z coordinates, of the next digital point of the geometry to be printed. And it includes the tool, in this case printer nozzle, orientation with respect to the digital print geometry. This tool orientation is indicated with the K vector, consisting of K_x, K_y, and K_z, which indicates the orientation of the tool with respect to the digital print geometry. Additionally the inverse kinematics step requires inputs from the machine setup, indicating offsets between the workpiece zero point and the coordinates of the rotation centres of the B and C axis. These are defined by D_y and D_z, indicating the y and z values of these offsets.

The process starts by calculating the orientations of the B and C axes, which are then used to transform the motion of the X,Y and Z axes. These rotations axes are calculated through Equation 5.1 and Equation 5.2. Once the angles of the rotation axes are known these are used together with the point coordinates in the digital workpiece reference frame, P_x,P_y and P_z, and the machine offsets, D_y and D_z to calculate the machine linear axes positions X, Y, and Z through Equation 5.3 to 5.5.

$$\theta_B = \cos^{-1}(K_z) \tag{5.1}$$

$$\theta_C = \tan 2^{-1}\left(\frac{K_x}{K_y}\right) \tag{5.2}$$

$$X = P_x\cos(\theta_C) - P_y\sin(\theta_C) \tag{5.3}$$

$$Y = P_x\cos(\theta_B)\sin(\theta_C) + P_y\cos(\theta_B)\cos(\theta_C) - P_z\sin(\theta_B) - D_y\cos(\theta_B) + D_z\sin(\theta_B) + D_y \tag{5.4}$$

$$Z = P_x\sin(\theta_B)\sin(\theta_C) + P_y\sin(\theta_B)\cos(\theta_C) + P_z\cos(\theta_B) - D_y\sin(\theta_B) - D_z\cos(\theta_B) + Dz \tag{5.5}$$

These equation were adapted for from the work of LinuxCNC[44] for the inverse kinematics for this particular printer.

Generating 5-axis Gcode: Post-Processing

With all the motion axes defined for a given move there is still a few parameters that need to be defined for the full Gcode line to be completed. First of all a value must be calculated for the extrusion motor, in order to deposit the correct amount of molten filament within the move. Furthermore, the speed value for the specific move must be calculated. And finally some post processing is required on the B and C axis values due to the specific setup of these axis in the current machine.

The extrusion value for a specific print move is obtained by calculating the desired cross sectional area of the print line being deposited and multiplying this by the print line length. (Equation 5.6 and Equation 5.7.) This results in a volume of material to be deposited. However the extruder motor takes in filament of a certain cross sectional diameter for a specified amount of length as defined by the Gcode value. By taking the amount of material to be deposited in the print line and dividing it by the cross sectional area of the filament (Equation 5.8) the resulting value indicates the amount of length units the filament has to be moved to provide the correct amount of material to the print move (Equation 5.9.)

$$A_{print\_line}[mm^2] = Width_{print\_line}[mm] * Height_{print\_line}[mm] \tag{5.6}$$

$$V_{print\_line}[mm^3] = A_{print\_line}[mm^2] * L_{print\_line}[mm] \tag{5.7}$$

$$A_{filament}[mm^2] = \pi * Radius^2_{filament}[mm] \tag{5.8}$$

$$L_{filament\_extruded}[mm] = \frac{V_{print\_line}[mm^3]}{A_{filament}[mm^2]} \tag{5.9}$$

The speed of a print move is defined by the desired printing speed, which is usually in the range of 20 to 40 mm/s for LCP printing [3]. Because the 5-axis printer interprets speeds in terms of unit per minute, the desired print speed is converted from mm/s to either mm/min for linear axes, $deg/mins$ for rotational axes or a combination of these two. For a simple linear motion with only linear axes, this means the desired print speed is multiplied by 60 to obtain the required F speed for the printer. The other two motion modes and associated speed calculations will be detailed in subsection 5.3.3 for circular motion, and subsection 5.3.7 for combined linear and circular motion.

With the inverse kinematics calculations presented above the θ_B axis values can end up with values between -180 and 180 degrees, or similarly $-\pi$ to π in radians. However in reality the B axis in the printer setup is limited to only a 180 degrees range of motion, furthermore it is mounted at a 45 degree angle with the horizontal of the 5-axis printer frame, as discussed in subsection 5.2.4 and shown in Figure 5.8. This means that any value of the B axis outside of the range 135 to -45 degrees is physically not possible by the printer. The post processing for these calculations means that θ_B axis values outside of the earlier mentioned range are clipped and set at the limit value of 135 or -45. This change must then also be reflected in the values for X, Y, and Z by using the filtered θ_B values in Equation 5.3, 5.4 and 5.5.

Finally, similar as to the θ_B values, the θ_C values coming from the inverse kinematics calculations are within the range of -180 to 180 degrees. However for this C axis, the possible range of motion is infinite. This must also be reflected for continuous print moves going beyond one single revolution, as the θ_C values will clip from 180 degrees to -180 from one point to the next in a continuous rotational move. The post processing step for θ_C takes all θ_C values of a complete print line or print layer, depending on what kind of layer is printed which will be discussed where relevant in the following sections. The difference between these values are then cumulatively added starting from 0 or a specific starting angular position. For spiralling print moves this could lead to θ_C values starting at 0 degrees and running into the ten thousands of degrees.

5.3.3. 5-Axis FDM of Cylinders

To validate the Gcode generation that was explained in the previous subsection a cylindrical printing sequence is chosen as a first step. These cylinders would be printed by rotating the C axis and moving only the Z axis, and with that creating a helical print. This method was also chosen to be used for the eventual printing of liners, thus starting with cylinders was a good starting point for working out the initial issues with the printer.

The Gcode was generated by creating a cylindrical surface in Grashopper of the desired final printed geometry. From this 3D surface, the line of revolution was taken. Meaning the line that will form the cylinder if it is revolved around the centre axis of the cylinder. This line is the split up into points

separated from each other by one layer height. These points are then used to generate the helical path for the printer to follow. Each point is revolved around the centre axis of the cylinder a predefined amount, which is called the circular resolution. And each new point in this revolution is moved up in the z-direction by the layer height divided by the circular resolution. This will result in a helical path spanning the entire cylinder. This helical path, made up of points, is then fed into the inverse kinematics routine in Grashopper resulting in a Gcode.

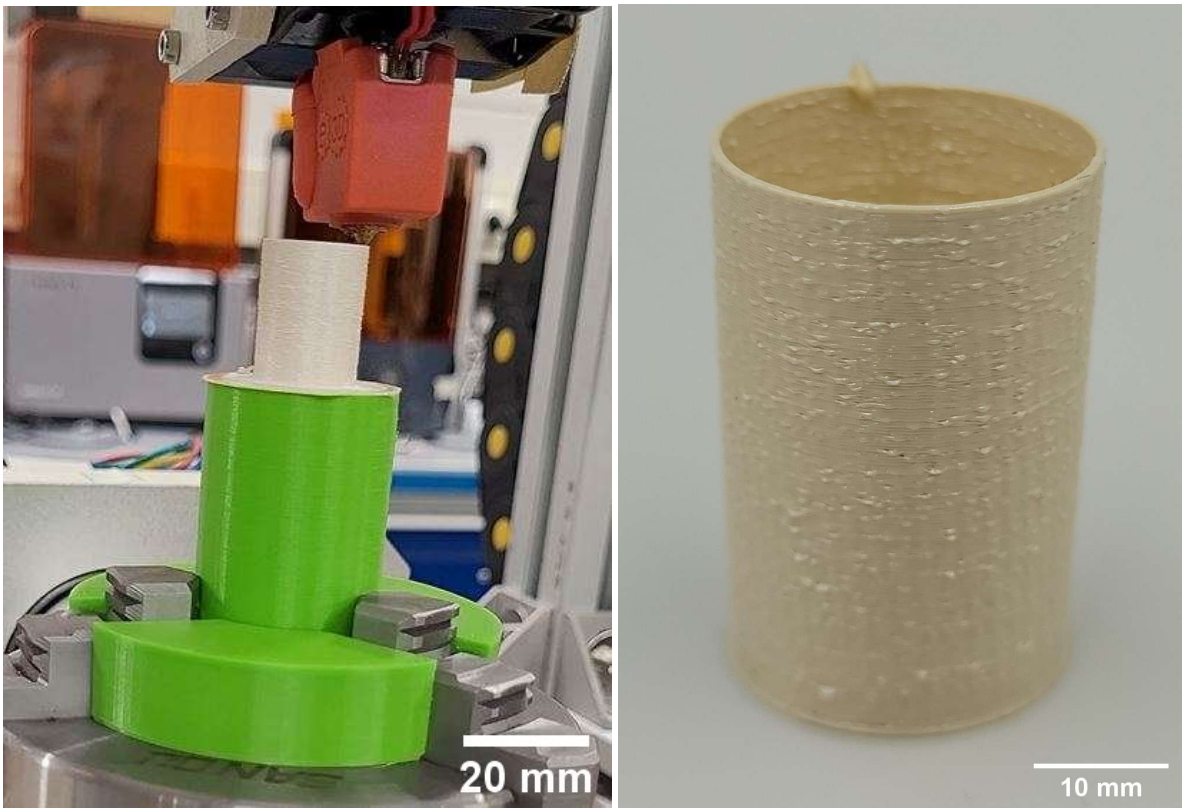

(a) Cylinder being printed, with only the C-axis rotating and the Z-axis slowly moving up to form a helical cylinder.

(b) Resulting printed cylinder

Figure 5.10: Straight cylinders printed with the modified 5-axis printer

In the printing mode for this cylinder, with only the C axis, Z axis and extruder moving, the speed values are interpreted in a combined linear and rotational motion. However because the linear moves are extremely small compared to the rotational moves, for example a $0.1mm$ layer height Z axis move for every 360 degrees C axis move, the speed value will be effectively interpreted as a rotational deg/min value. Because what Mach3 does for combined motions is that, for a move the required motion for each axis is calculated and the axis with the most movement to make will be the main axis move with the associated input speed. Then all the other axis moves are scaled in speed to match the time required for the main axis move to be completed. Thus in the case of this cylinder printing the speed value will have to be tailored for the rotational speed of the C axis in order to arrive at the desired print speed of the print line. Equation 5.10 to 5.13 shows the calculations in order to obtain the desired F value in deg/min.

$$F[deg/min] = \frac{\theta_{move}[deg]}{t_{required}[min]} \tag{5.10}$$

$$\theta_{move}[deg] = \frac{360[deg]}{resolution_{circular}} \tag{5.11}$$

$$t_{required}[min] = \frac{length_{move\_arc}[mm]}{V_{desired}[mm/sec] * 60} \tag{5.12}$$

$$length_{movearc}[mm] = radius_{move}[mm] * \theta_{move}[rad] \tag{5.13}$$

In order to print these cylinders on the 5-axis printer a support structure was designed and printed out of PLA to fit in the three chuck vice of the C axis and provide a flat base to print on. After some trial and error, the best interface between this PLA surface and the printed LCP was to cover the PLA surface in masking tape and rubbing a standard glue stick on this. There are adhesives specifically designed for FDM which also work well with LCP on standard 3 axis printers. However these are designed with a heating bed in mind, where the adhesive only activates above a certain temperature. Which is unfortunately not possible in the current printer setup.

5.3.4. 5-Axis FDM of Overwrap Layers on Cylinders

The next step in the printing development was adding overwrap layers to the cylindrical prints. These overwraps were split up into three distinct modes. Overwrap layers in the hoop direction, also indicated as 90 degrees from the cylinder axis, overwrap layers in the cylinder axis, 0 degrees, or thirdly any angle in between, θ degrees from the cylinder axis. These three different modes can also be applied to the eventual pressure vessel printing and are therefor important to validate on cylinders first. Any issues that are present in the cylinder overwrap printing can then be solved for pressure vessel overwraps as well.

The first iteration tested was the 90 degree overwrap, where a layer is added on top of the cylinder in a similar helical pattern as the cylinder itself. However in this configuration the spacing between each revolution in the helical is not a layer height, as it was for the base cylinder, but the spacing is the print line width. In this mode the nozzle is orientated normal to the cylinder and prints the lines next to each other instead of on top of each other. Similar as the helical printing of the cylinder wall the F value is interpreted as a rotational deg/min value and should thus also be calculated following the same Equation 5.10 to 5.13. Furthermore the same calculation steps are used to generate the E values for the extruder axis, Equation 5.6 to 5.9.

In the 0 deg print line orientation lines in the cylindrical axis direction of the cylinder are printed next to each other on the surface of the cylinder. Print lines are spaced with a print width apart from each other. In this orientation only the Y axis is moving during the printing of the line, so the F value is interpreted as linear mm/min values, which are calculated by converting the desires print speed from mm/s to mm/min. Then the moves between two print lines are a short hop in the Z direction to get clearance between the nozzle and the workpiece and a rotation of the C axis to align the nozzle with the location of the next print line on the cylinder.

The remaining overwrap printing mode is the printing of lines at any angle excluding 0 and 90 degrees from the cylindrical axis. This is a particularly interesting printing mode as it both incorporates the linear and rotational axes to print the print lines. For example, printing a 45 degree line would require both the C axis and Y axis to be engaged at an equal proportion. Figure 5.11 presents two printed cylinders with a 45 and -45 degree overwrap. As can be seen a portion of the cylinder is left uncovered by the overwrap layers, this is due to the nozzle not being able to reach these sections when printing normal to the cylinder surface. In this mode the B axis is angled at 90 degrees and this causes a clash between the extruder on the print head and the 3 chuck vice holding the PLA bracket on which the cylinder is printed when printing normal to the bottom section of the cylinder.

5.3.5. 5-Axis FDM of a Pressure Vessel Liner

The next step in the printing development is printing a liner wall that is not a constant shape like the cylinder previously printed. But which shape is a fully enclosed pressure vessel. The chosen shape for the pressure vessel is a cylinder in the base, with elliptical endcaps on both ends. The bottom end cap has a cylindrical section extruding from the centre which will serve as a starting point of the print and

Figure 5.11: Cylinder with -45 (left) and 45 (right) degrees overwrap, the bottom section of the cylinder cannot be reached by the nozzle when printing normal to the cylinder

eventually be the cylinder in which the threaded connection is placed. This cylinder is printed on top of a PLA bracket printed on a standard 3-axis FDM printer. This base is mounted in the 3 chuck vice of the C axis.

The main process of generating the Gcode for this liner is similar as the straight cylinder. Where a cross sectional line of revolution is taken and split up into points separated by the chosen layer height. These are then turned into a helical print path enclosing the entire surface of the liner. The nozzle vector follows the tangent of the liner at every point, however at the top of the liner the angle of this tangent exceeds the range that would be required on the B-axis. As mentioned in subsection 5.3.2 B axis values are clipped at -45 degrees, which occurs in the top endcap of the liner. Fortunately it is possible to print overhangs of maximum 45 degrees, meaning that the remainder of the top endcap can be printed without the nozzle following the tangent of the endcap. In Figure 5.12a the last part of the printing sequence is shown where the nozzle is not tangent to the workpiece, which itself is angled at -45 degrees by the B axis. Figure 5.12b shows the finished liner with the inside visible through the bottom cylinder.

For these F and E calculations the same processes are used as described in subsection 5.3.2. However as the radius of the workpiece as measured from the centre axis of revolution of the liner decreases towards zero in the top endcap the F value will increase towards infinity due to the equations used. An extra filter is added to the F speed calculation to clip it at a set maximum speed, which is dependent on the possible rotational speeds of the stepper motor, rotating baseplate and gearing between the two.

5.3.6. 5-Axis FDM of 90 Degree Overwrap Layer on Pressure Vessel Liner

After printing a complete liner it can be covered with overwrap layers like the cylinders from subsection 5.3.4. Like the cylinder the overwrap layers were split up into three modes, 90 deg lines, 0 degree lines and any angle (θ) in between, where the angle is measured against the centre axis of the liner. This section will cover the 90 degree layers, whereas the following two sections, 5.3.7 and 5.3.8, will cover the 0 and θ degree layers respectively.

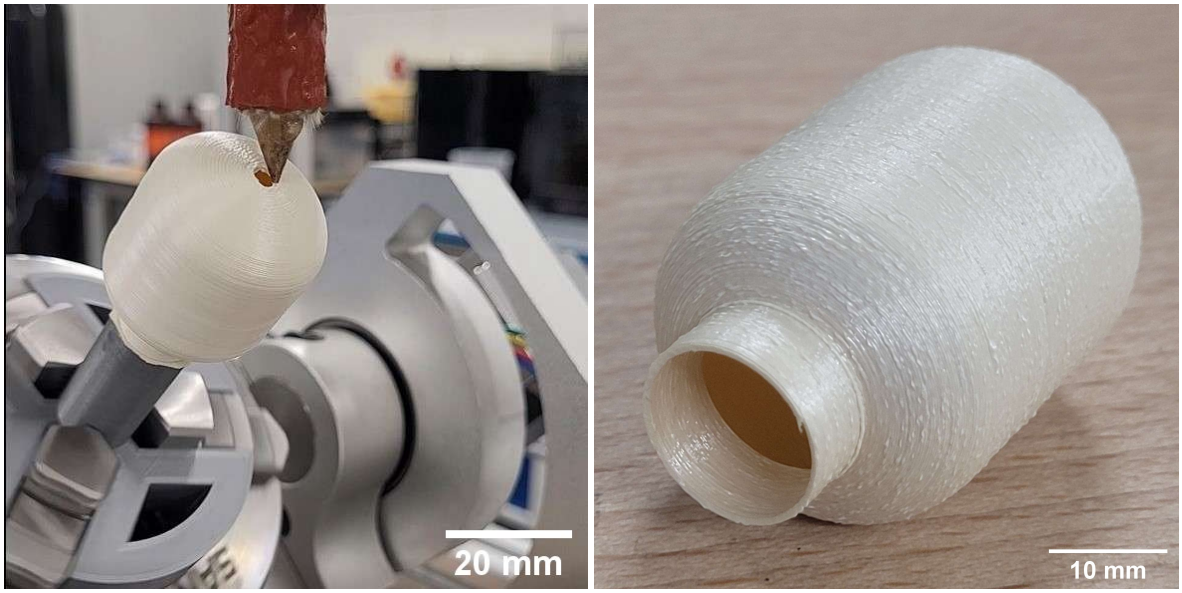

(a) Last lines of the liner being printed, at an B axis angle of 45 degrees the nozzle can not remain tangent to the liner for the last part of the top endcap.

(b) Finished Liner, the cylinder at which the print starts is visible at the bottom

Figure 5.12: First prints of a liner on the modified 5-axis printer

First of all the 90 degree overwrap can be printed by orientating the nozzle normal to the surface of the liner and offsetting the nozzle tip one layer height from the surface of the liner. The digital geometry to create the Gcode is created similarly to the liner method, the curve used to generate the liner geometry is offset by one layer height to create the curve for the 90 deg overwrap. This curve is then split up into points separated by one layer width from each other. Between two adjacent points a helical curve is created which lines up with the adjacent helical curves to form a helical path completely covering the surface of the liner. Each point is then projected back to the surface of the liner where the projected point is used to find the normal vector of the liner surface at this point. This normal vector is then used as the nozzle vector for the 90 deg overwrap. This overwrap mode is also shown in Figure 5.1

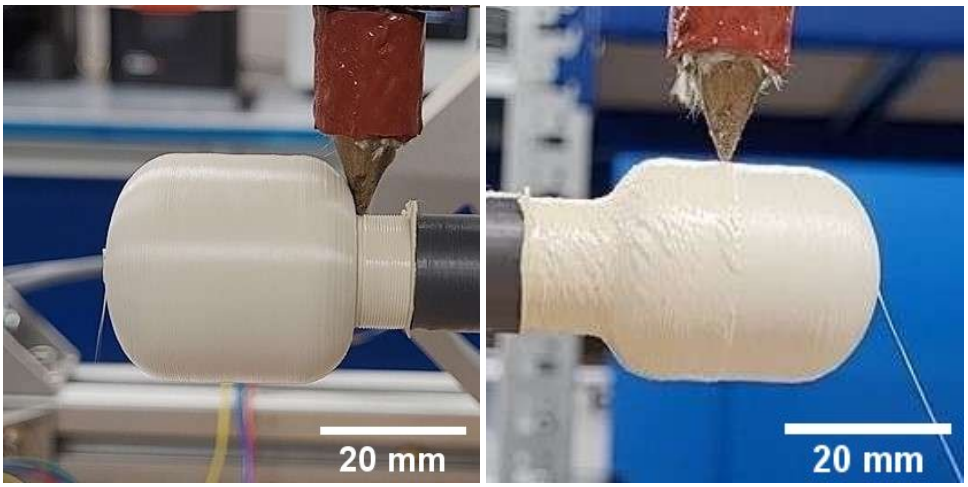

(a) Without a fillet the nozzle clashes with the liner wall at the corner between the cylinder and the bottom endcap

(b) Successful 90 degree overwrap printing with an added fillet in the liner geometry.

Figure 5.13: Adding a fillet in the liner curve prevents the nozzle from clashing into the liner wall when transitioning from the base cylinder to the liner wall.

Adding a fillet to the liner

Figure 5.13a shows a liner on which a 90 deg overwrap is being printed. The cylindrical base section has already been covered by the overwrap in this image, as can be seen by the different line spacing between the uncovered and covered liner section. Where the covered section shows the line spacing of the print line width, with this nozzle that is set to $0.4mm$ and the uncovered section shows a line spacing of the layer height, which was set at $0.1mm$. One issue that arises with this particular print, and the printing process in general at the time of printing this piece, is that just after this picture has been taken the nozzle will clash with the bottom endcap of the liner. Because there is a sharp corner between the base cylinder and the bottom endcap of the liner, the nozzle does not have the clearance to turn and follow the normal vector at each point before and after this corner. This results in the nozzle first cutting into the bottom endcap with its side, which will quickly lead to too much force for the liner to withstand. This will cause the liner to split at the sharp corner and detach from the base cylinder.

A way to solve this issue is by adding a fillet in this sharp corner. This fillet can already be integrated in the liner printing itself, replacing the sharp corner with a smooth fillet curve connecting the base cylinder curve to the bottom endcap curve. When this new liner curve is then used to create the offset 90 degree overwrap curve it will ensure a smooth 90 degree printing without cutting into the liner. Figure 5.13b depicts a 90 degree overwrap layer successfully being printed on top of a liner with an integrated fillet.

Top endcap geometry adjustment for overwrap layers

Continuing the 90 deg overwrap layer to the end of the top endcap uncovered another problem in the printing of overwrap layers. This is presented in Figure 5.14a, where the 90 deg overwrap has been printed on the top endcap of the liner. However as can be seen in the figure it has severely under-extruded and in some locations the print lines have completely detached. This was caused by the gap between the liner and the nozzle for this area of the overwrap being much larger than the intended height of this layer. Coincidentally the area where this detaching and underextrusion occurred was roughly the same area of the liner where the nozzle does not follow the tangent of the liner curve anymore, due to the end of the B axis range being reached, as was explained in subsection 5.3.5. When the nozzle in the liner printing mode does not follow the tangent of the liner curve anymore, it means that the nozzle is angled to one of the two sides of the print line. In this case it points away from the liner towards the outside, as can be seen in Figure 5.12a. This causes the molten material exiting the nozzle to have more room to go inwards with respect to the liner geometry than outwards, because the outward direction is covered by the nozzle. A diagram of this proposed phenomenon is shown in Figure 5.15b. This could cause the discrepancy between the digital liner geometry and the printed liner geometry, which causes the detachment and underextrusion of the 90 degree overwrap layer. The difference between the printed liner geometry and the expected location of the overwrap layer is also present in Figure 5.15a, although the figure shows a 0 deg liner the same holds for a 90 degree layer.

This issue can be solved by changing the geometry used as a basis for the overwrap layers. Each overwrap layers is an offset of the original liner geometry. So if this original liner geometry is adjusted to account for the height difference in the top dome, it will be reflected in these overwrap layers. The top endcap curve can independently be changed from the rest of the liner curve. The end point of this curve, at the top of the liner, is lowered by a certain amount. The starting point of this curve remains at the same location. This gradually lowers the curve from the start point of the top endcap to the end point. The amount by which the top point is lowered was estimated by measuring the height difference between the expected top point and the real top point. This was measured on a printed liner by gradually lowering the nozzle in small steps towards the top point, until the nozzle started touching the printed liner, which caused visible melting of the liner. This distance was then used as a starting point for the offset, which was then further calibrated by trial and error on several prints. After the correct value had been obtained the 90 degree layer could be fully printed without detaching or under extruding on the top endcap. As can be seen in Figure 5.14b.

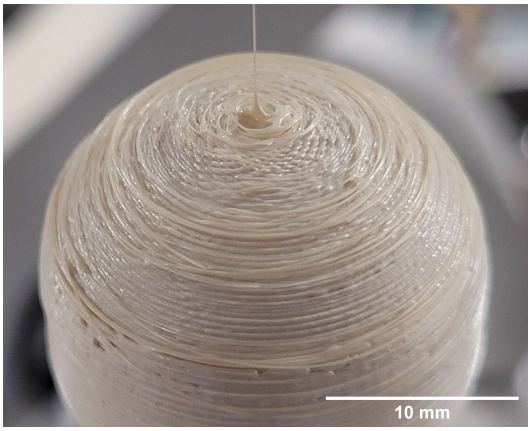

(a) A 90 degree overwrap layer that does not include the adjusted base curve

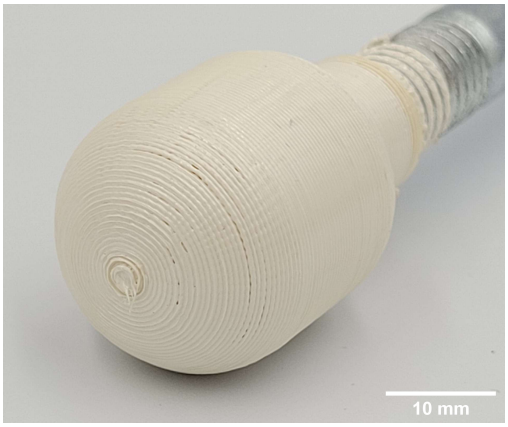

(b) A 90 degree overwrap layer printed including the adjusted base curve

Figure 5.14: The top endcap shape of the liner does not match the digital geometry. Lines printed on top of this section show major under extrusion and detachment. This is fixed by adjusting the digital base curve.

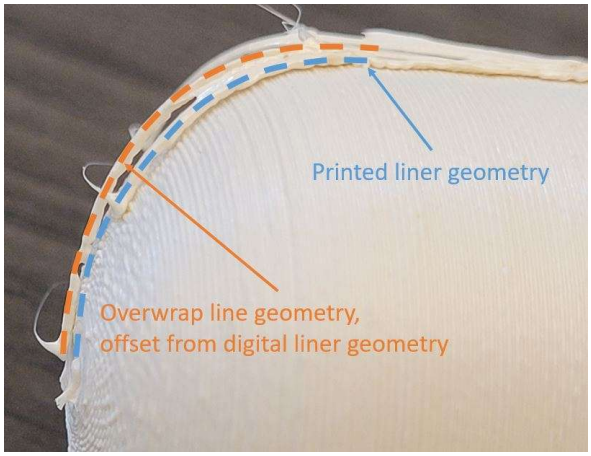

(a) A large gap is present between the printed overwrap line and the underlying printed overwrap layer, the printed overwrap layer assumes a different underlying liner geometry.

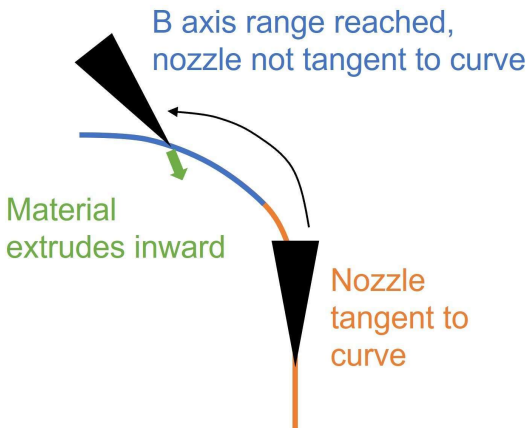

(b) Diagram of proposed phenomenon occurring during non tangential liner printing, causing the gap between the overwrap layers

Figure 5.15: Large gaps occur between the overwrap and the underlying print.

5.3.7. 5-Axis FDM of 0 Degree Overwrap Layer on Pressure Vessel Liner

In 0 degree overwrap printing layers the print lines cover the underlying surface with lines parallel to the centre axis of the liner. The amount of lines placed on the surface is based on the largest circumference present in the liner, in this case in the middle of the liner. The circumference is covered by enough lines of the specified print line width to fully cover the liner. The digital geometry of these lines is created by taking one half of the cross sectional curve of this layer and copying it rotationally around the centre axis with the number of required print lines for the current layer. However when this amount of print lines are placed on a piece of the liner geometry with a smaller circumference, for example the base cylinder on the bottom endcap, this means the line spacing will be smaller than the specified print line width. This is solved by running the set of lines of a 0 degree layer through a filter that will cut lines short that have a lower than specified print line spacing with its two adjacent print lines. Each line is checked from start to end on the distance between its adjacent lines and then cut short at its ends where the line spacing is lower than the specified print width. This process is run iteratively across all print lines in a layer. An example of the resulting print lines is presented in Figure 5.16. With this filter in place

the entire surface can be covered in 0 degree lines without adjacent lines interfering when they are too close.

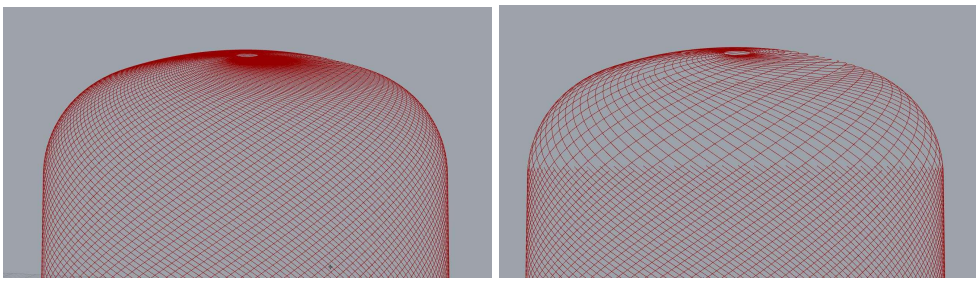

(a) Before applying the filter, lines extend all the way to the top of the shape

(b) After applying the filter, some lines are cut short.

Figure 5.16: Visualisation of the print lines of a 55 degree layer, before and after filtering the individual lines that are too close to each other. The filter functions the same for 0 degree lines.

In Figure 5.17a a print is shown with 0 degree lines printed over a portion of the surface. On this print there is quite some overextrusion visible towards the top endcap, combined with severe stringing in this same area. The stringing occurs when the extruder does not retract a small amount of filament with the required speed and amount. Initially high speeds for this retraction were given in the Gcode, however the printer extruder was limited by the settings in Mach3 in its acceleration settings. The allowable acceleration on the extruder axes was increased in Mach3 and this allowed the retraction to happen fast enough, eliminating the major stringing.

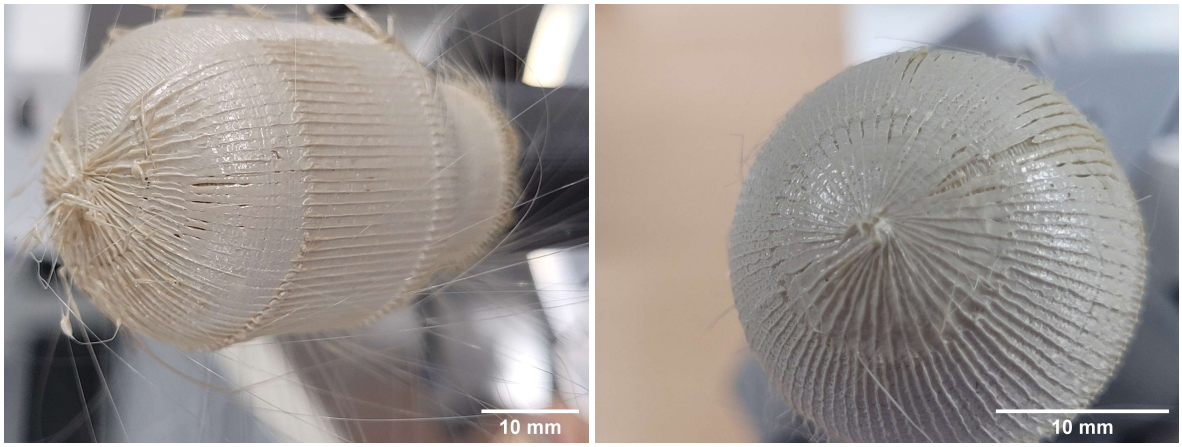

(a) 0 Degree lines printed on a liner before calibration, lots of overextrusion and stringing visible.

(b) 0 Degree lines printed on a liner after calibration, the overextrusion and stringing has been reduced.

Figure 5.17: Calibrating the 0 degree print lines

Variable width printing

Furthermore the over extrusion towards the top of the endcap is caused by the spacing between adjacent print lines reducing as the print line nears the top of the endcap. As was mentioned in the first paragraph of this subsection the print lines are filtered when the spacing drops below the specified print width. However this means that there is still an uneven distribution of line spacing between the discretely filtered lines. Another filter was added that measured the distance between adjacent lines for each Gcode point, these distances are then used for the calculation of the extrusion values. Which follow the equations of 5.6 to 5.9, where $Width_{print\_line}$ is replaced by the variable distances measured from the new filter. After applying both this variable width filter and the increased retraction acceleration the 0 degree print lines showed much better quality, as can be seen in Figure 5.17b.

Variable speed control modes

Finally an important additional feature that is required for the 0 degree print lines are the speed value calculations. The speed calculations thus far were intended for printing helical cylinders, pressure vessels or 90 degree overwraps. Which were all guided by the circular printing speed of the C axis as the main speed driver. Any of the other axes moved comparatively small amounts to the move required by the C axis. However in the 0 degree printing mode the B axis and Z axis are also engaged in the curved areas of the fillet, bottom endcap and top endcap. In these curved areas the B and Z axis moves are of comparative order of magnitude as the Y axis moves of the straight lines on the base cylinder and straight piece of the liner. In Figure 5.18 a liner print is shown where the different speed interpretation modes are indicated. Blue straight lines indicate moves where only the Y axis moves, whereas the curved orange lines indicate moves where the B and Z axes are also engaged. In the curved areas the Mach3 interpretation of the F speed value will be limited to not the Y axis maximum speed and acceleration, as is the case for the linear moves, but those of the B and Z axis. In the case of the curves in the fillet, bottom and top endcap the Z axis is closest to its maximum value compared to the B or Y axis. This means that the Y axis speed in these moves is greatly reduced as compared to the Y axis speed in the straight pieces of the 0 deg line. Ultimately this translates to a reduced speed of the nozzle with respect to the surface it is printing on. And because the B and Z axis start to be engaged from one Gcode point to the next, this shift in nozzle speed is very sudden and causes inconsistent print line quality.

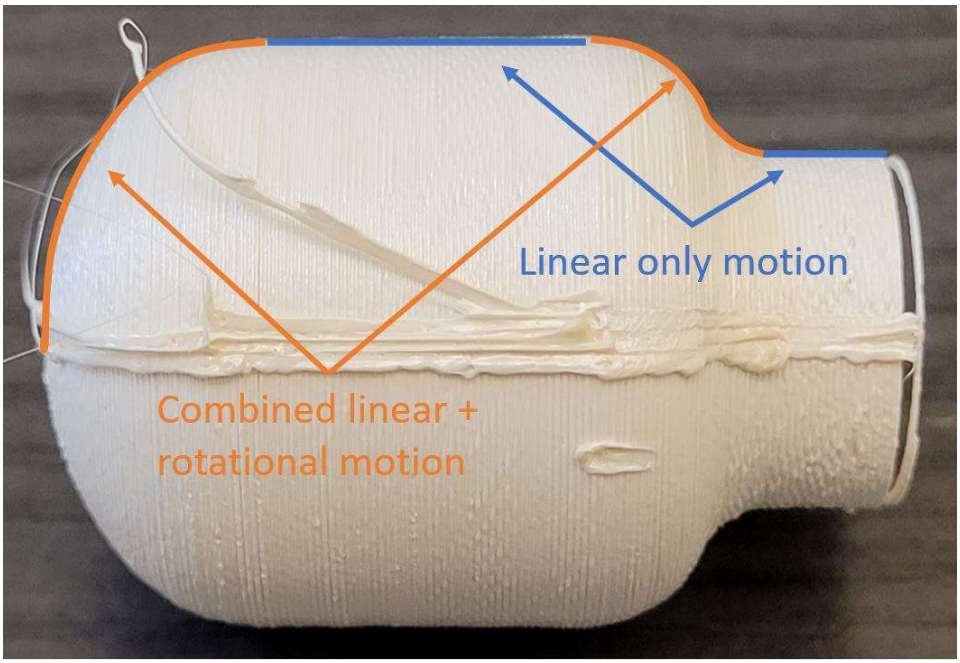

Figure 5.18: The different speed value interpretation modes are indicated, the blue straight lines indicate linear moves where only the Y axis are moving, whereas the orange lines indicated moves where the B and Z axes are used as well.

One method to get these nozzle speeds more consistent in a single print line is to used a different F value interpretation method in Mach3. As mentioned in subsection 5.3.2 the F value is interpreted as mm/min or deg/min, however there is a different mode called the inverse time method. The inverse time method can be turned on from within the Gcode. It interprets the F value as the inverse of the time required for the move of that Gcode line, thus the units of F in the inverse time method are $1/min$. This allows for Mach3 to calculate all the required speeds and accelerations of all the axes while still allowing for a constant nozzle speed throughout a 0 degree print line. The nozzle speed is maintained constant if the F value for the inverse time method is constant between all Gcode points as long as the Gcode points are spaced with a constant distance. Essentially the F value is calculated by dividing the printing speeds mm/min by the length of the move mm.

Unfortunately the desired print speed can not be maintained in the curved areas, as the maximum

acceleration and velocity of the Z axis are exceeded by at least a factor of 10 when printing at printing speeds of 20 to $30mm/sec$. Increasing the maximum velocity of the Z axis in any reasonable amount is not possible within the current setup of the 5-axis printer. Increasing the maximum acceleration above the standard setting causes excessive vibrations on the nozzle, which degrade the print line quality. A process is added to the Grashopper file for smoothly transitioning the print speeds from the desired print speeds in the linear regions to the throttles print speeds in the curved areas. This process takes the original F values, in inverse time units, for an entire print line and lowers these values in the areas where the Z axis reaches its maximum velocity to a value which will result in the Z axis being moved at its maximum speed. The print moves that are not clipping the Z axis at its maximum velocity remain at their original levels. The transition regions between these two different modes are smoothly joined by transitioning from the original F values in the linear region to the clipped F values in the curved region over several Gcode points. This results in the print lines printing at a continuous speed in the linear regions, while also smoothly transitioning to lower speeds for the curved regions.

5.3.8. 5-Axis FDM of θ Degree Overwrap Layer on Pressure Vessel Liner

The remainder of the possible printing directions for overwrap layers are a combination of the 0 degree print lines and 90 degree print lines, which were discussed in subsection 5.3.6 and 5.3.7. This section will discuss the process for generating the Gcode and printing overwrap layers of ± 45 degrees as an example.

The individual print lines are generated starting with one single line that follows the contour of the underlying geometry at a 45 degree angle on the surface with respect to the centre axis of the liner geometry. These lines are then, similarly to the 0 degree lines, rotationally copied to cover the surface of the underlying geometry. These lines are also run through a filter to trim lines short when the distance between their neighbours is below the desired print line width. All the lessons taken from the printing of the 0 degree lines are applied to 45 degree layers, including the variable width printing and the variable speed control.

Figure 5.19a shows the first print of a 45 degree overwrap layer on a small liner with a 90 degree overwrap layer on it. This print shows good coverage along the length of single print lines, showing that the top endcap height is effectively adjusted. Furthermore the print lines reduce in width towards the top of the part, indicating that the variable width printing is active accordingly. However a major issue with this print is the radial spacing of the print lines. In the process of sequencing the print lines in the Gcode generation and cumulative C axis calculations discussed subsection 5.3.2 an error was made when including the starting C values of each print line. This error in the post processing code was resolved by taking the C values of the starting Gcode point of each print line, and carrying these through to the cumulative C axis calculations as starting value for each print line. With this change implemented the 45 degree lines are now nicely positioned next to each other, as can be seen in Figure 5.19b. This print does show underextrusion, however this occurred due to an un-calibrated extrusion multiplier.

5.3.9. 5-Axis FDM of Threaded Base

For the pressure vessels that are to be tested a pressure connection is needed, as explained in subsection 5.1.2. As mentioned in that section a threaded rod will be used as a base to print on and serve as a mould for the internal thread of the printed pressure vessels. Printing the thread has been split up into two helical lines to form the threads and several overwrap layers to connect the threads and build up a cylinder around them. The first of the two helical lines matches the troughs of the threaded rod, and extrudes enough material to fill these troughs. The second helical line is offset by half a thread pitch and extrudes only the material for a $0.4mm$ wide $0.05mm$ high layer. This second helical serves to connect the threads of the first helical before the overwrap is printed. Figure 5.20a shows a print where the first helical has already been printed and the nozzle is printing the second helical in between.

After the two helical lines of the internal thread are printed they are covered with a cylindrical overwrap. This cylindrical overwrap functions as a base to print the liner on. In order to get a sufficiently consolidated structure around the internal thread the design of the overwrap layers consists of four layers, each $0.1mm$ in height, and with a stacking sequence of: [90/0/90/0]. section 4.5 lists a cross ply laminate as one measure to increase permeability of a LCP additively manufactured part. This is why the 0 and 90 degree layers are chosen on the cylindrical overwrap of the internal thread. Figure 5.20b shows a print that has a cylindrical overwrap on top of the internal thread.

The helical lines of the internal thread are the first layer to be deposited on the threaded rod. In

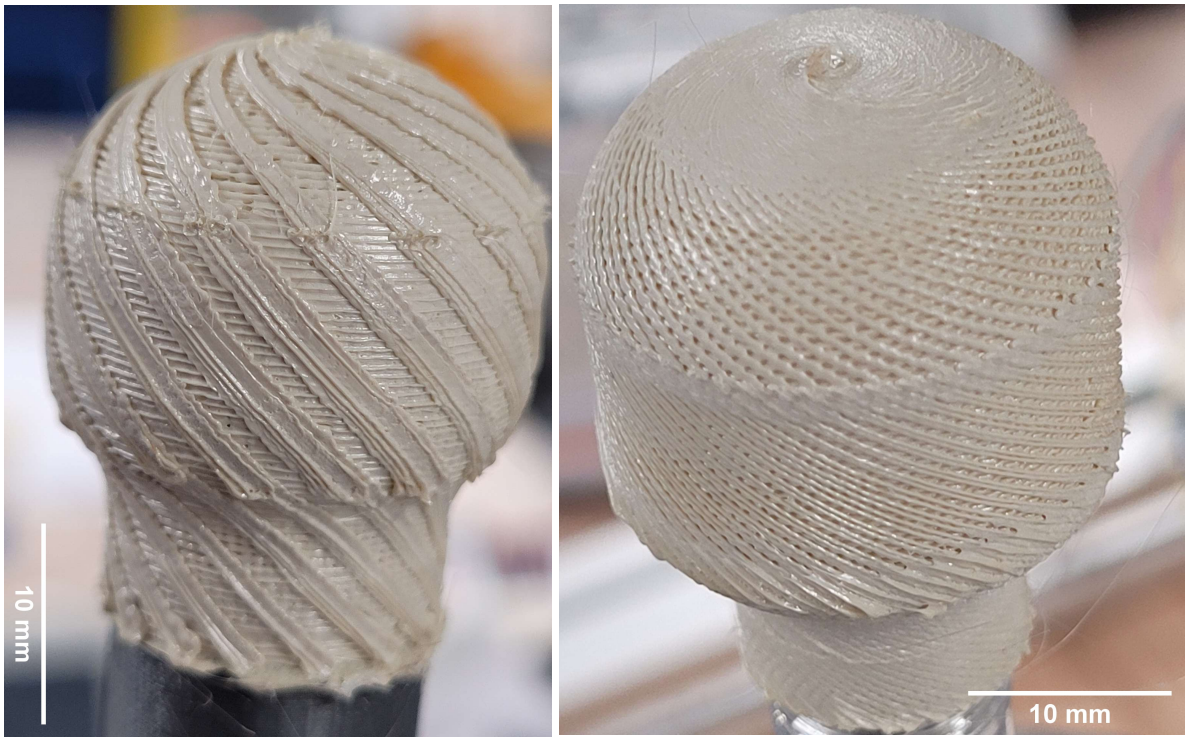

(a) 45 Degree lines printed on a liner, the rotational spacing of the lines is incorrect causing lines to be printed on top of each other instead of next to each other

(b) 45 Degree lines printed on a liner, the rotational spacing has been corrected. Some underextrusion is present, due to un-calibrated extrusion multiplier.

Figure 5.19: Correcting the 45 degree print sequence

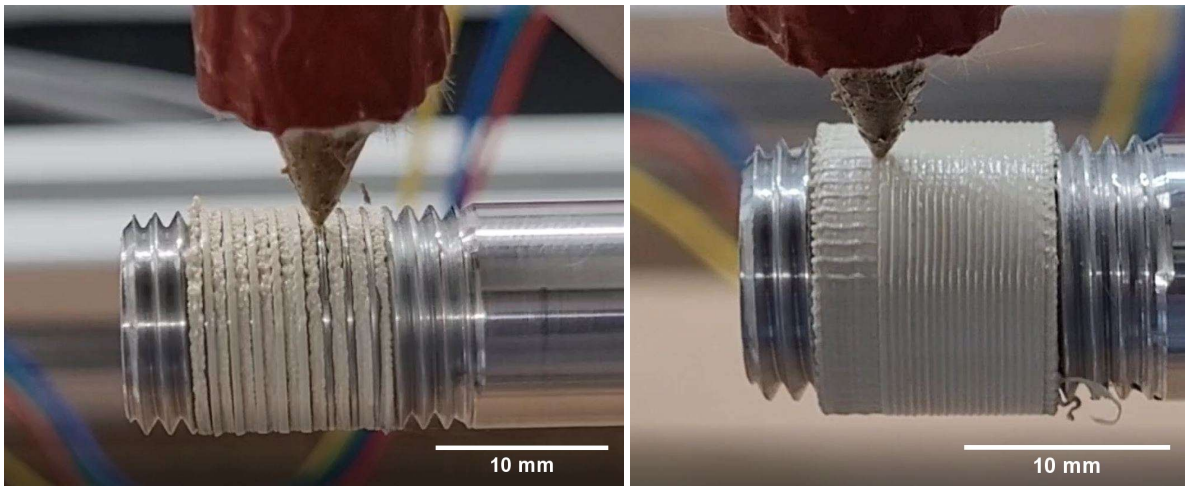

(a) Printing of the second helical on top of the threaded rod. The second helical path is in between the revolutions of the first helical.

(b) Printing of a 90 deg layer on a 0 degree layer on top of the internal thread.

Figure 5.20: Printing of the female threaded base cylinder of the pressure vessels, on top of the threaded rod as support point.

order to have these lines stick to the rotating threaded rod an adhesive spray is used. Care is taken not too apply too much adhesive, as this will interfere with removing a finished print from the thread.

5.3.10. Combined 5-axis FDM of Threaded Base, Liner and Overwrap Layers

Until now all pieces of a full pressure vessel print have been developed independently. In order to manufacture a LCP pressure vessel these must be brought together. The firs step is adding the liner printing (subsection 5.3.5, after the threaded base printing, subsection 5.3.9. As was explained in the subsection 5.3.6 it is important for the overwrap layers that the liner includes a fillet corner between the cylindrical base and the liner bottom endcap. However in the previous liner printing sequence the liner was printed as a continuous spiral including the cylindrical base. When starting with the threaded base printed on the threaded rod it is not possible to start printing the liner tangentially to the outer surface of the threaded base. The liner will have to start printing the bottom endcap normal to the surface of the threaded base. In this sequence the fillet is still not present for the overwraps to be printed on top.

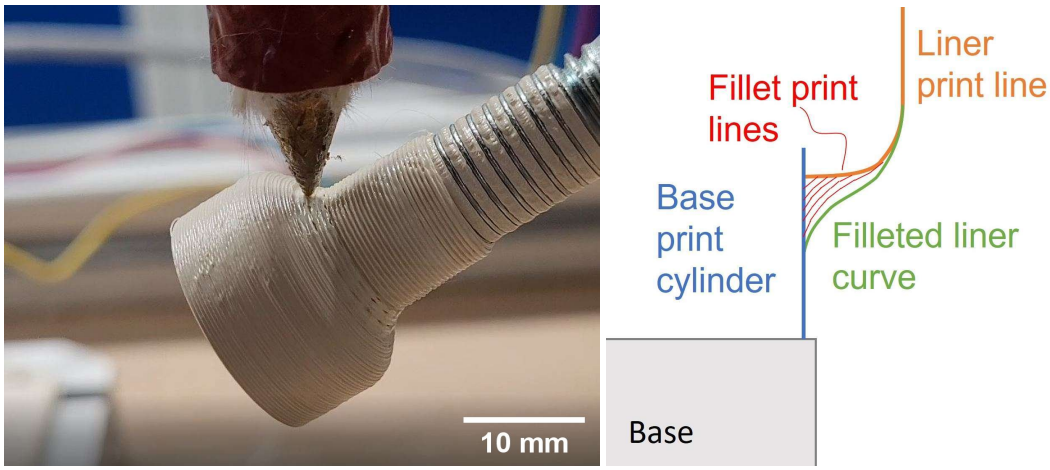

(a) Printing of the fillet between the threaded base and liner, after the liner has been printed. The fillet lines are orientated parallel to the fillet curve.

(b) A schematic of the fillet print lines being placed in the corner to fill up the space of the fillet curve. The fillet is printed after the liner.

Figure 5.21: Fillet printing in the corner between the base cylinder and the liner curve

The fillet can be added after the liner has been printed by filling the corner between the threaded base cylinder and the bottom endcap with lines until the complete fillet curve has been printed. Figure 5.21a shows a threaded base with the bottom half of the liner printed on top of it. In the figure the nozzle is printing the fillet in between the corner of the threaded base and the bottom endcap. The fillet digital geometry is created by taking the curve of the line and outer surface of the cylinder and adding the fillet to the corner. This fillet is then offset multiple time by a distance of one layer height until the new offset curves intersect the corner between the threaded base and bottom endcap. These new offset lines are then clipped at the points where they cross the liner curve and the threaded base curve, resulting in a set of lines building up the cross section of the fillet. These lines are split up into equal distance segments, with lengths as close as possible to the preferred line width. These midpoints of these segments are used to create the base points of revolution for each fillet revolution and the associated normal vectors. In Figure 5.21b this creation of the fillet geometry is presented, the corner between the cylindrical base and the liner is filled with multiple lines following the contour of the fillet liner curve.

An issue with the previous fillet printing method explained is that the entire liner is printed before the fillet is created. When increasing the pressure vessel size beyond the small test specimens, designed only for validating the printing process itself, to the designs of section 6.3 the liner becomes long enough that its own weight and the extrusion force at the top endcap can cause bending forces high enough to break off the liner from the base. An occurrence of this issue is shown in Figure 5.22. This can be solved by adding the fillet before the liner printing in order to give a stronger bending resistance at the base for during the printing of the liner. After the first few overwrap layers have been printed these layers will increase the strength of the print such that this no longer is a problem, but still for when only the liner is being printed it is still weak enough to detach.

This second method of printing the fillet before the liner is achieved by printing the fillet shape with layers printed on the threaded base that are parallel to the surface of the threaded base. The same

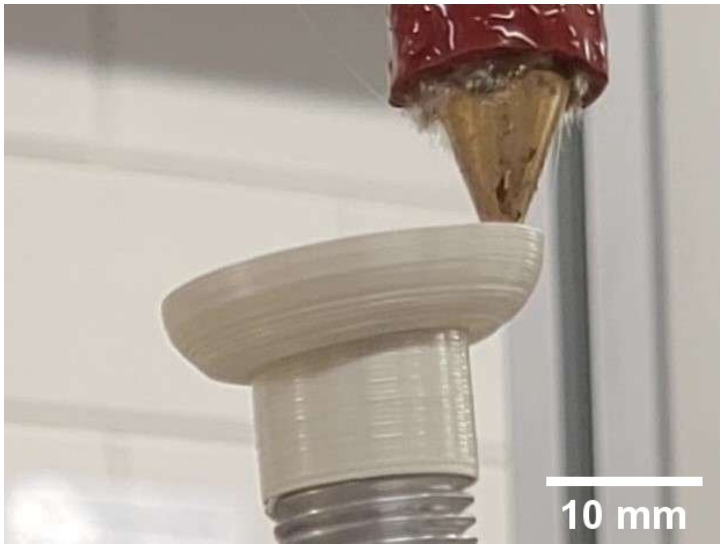

Figure 5.22: In some instances the liner detaches from the base cylinder during printing, when the liner is printed before the fillet.

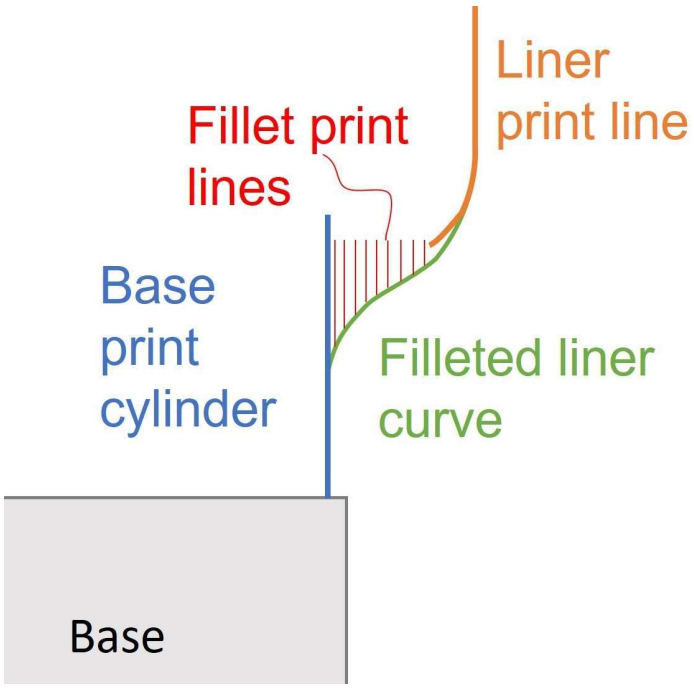

Figure 5.23: Second method of printing the fillet. The fillet lines are printed parallel to the base cylinder, the liner is printed after the fillet.

routine for creating the digital geometry is used as for the first fillet, with the main difference being the orientation of the fillet lines. In Figure 5.23 after this fillet has been printed the liner will start printing from the top of the fillet. Figure 5.24 shows two images, 5.24a shows the fillet itself being printed, built up of layers parallel to the threaded base. Figure 5.24b shows the orientation of the nozzle while it is printing the first line of the liner on top of the fillet.

Once the fillet has been printed in either of the two methods described earlier, the overwrap layers can be added on top. While using the threaded rod as a base for printing it was found that with the entire system of the threaded rod, 3 chuck vice, B and C axis rotating table, and 5-axis printer frame a variety of about $0.1mm$ was present at the end of the threaded rod as compared to the nozzle tip, when rotating it around its axis. This $0.1mm$ variety caused one side of the liner prints to be slightly

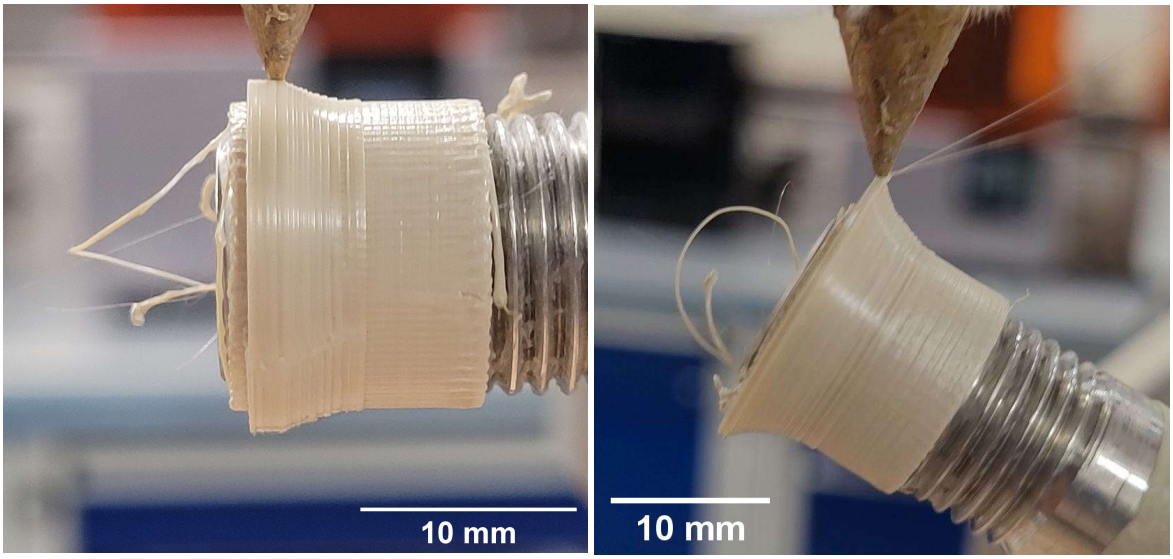

(a) Printing of the fillet between the threaded base and liner. The fillet lines are orientated parallel to the base cylinder

(b) The first lines of the liner being printed on top of the fillet.

Figure 5.24: Second method of printing the fillet and liner, where first the fillet is printed parallel to the threaded base, after which the liner is started on the end of the fillet.

bend away from the digital geometry, and the opposite side bend slightly towards the centre of the liner. When this was then overwrapped by the first 90 degree layer it caused one side to over extrude, and the opposite side to under extrude. This was accepted as it is not possible to improve the accuracy of the current system in the scope of this thesis. However a mitigation strategy could be applied to enforce the digital geometry back into the printed part after the first 90 degree overwrap layer has been printed. This can be achieved by repeating the entire print line of the first overwrap layer without extruding any material, in the FDM world this is called ”Ironing”. This ironing pass will chip away any overextrusions with the heated nozzle and smooth out the underlying layer. This also ensure that the surfaces of the print matches the digital geometry used to generate the ironing pass, which then serves as an accurate base to print the subsequent layers on. In Figure 5.25 an ironing pass is shown. Small areas of the fillet had overextrusions, which are taken away by the ironing pass.

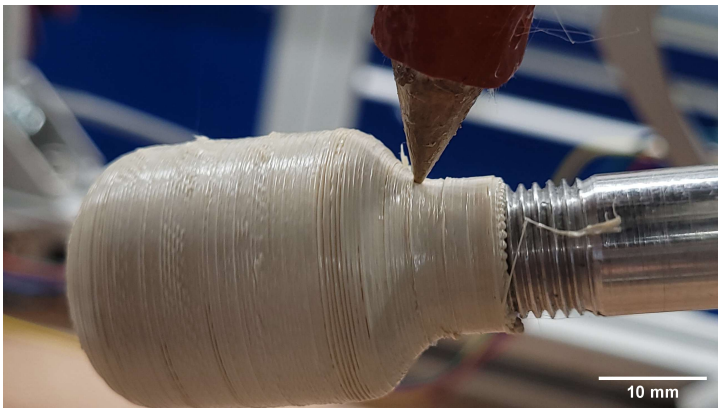

Figure 5.25: An ironing pass is executed, where the nozzle follows the outer contour of the part without extruding. Small chips of overextrusion are removed.

5.3.11. 5-Axis LCP Spin Printing

In subsection 5.1.3 the concept of adding spun lines inside the pressure vessel volume has been introduced. Furthermore the work of C. Mascolo [32] is used as a starting point for integrating the spun lines in the current pressure vessel work. Initially tests were performed on adding spun lines to cylinder printed on a flat base, as can be seen in Figure 5.26. The spun lines are manufactured at a printing speed of $100mm/s$ with a low extrusion rate that is calibrated in order to obtain the optimal spun line quality. For every new extruder, heating block and nozzle combination the minute differences in this system required differently calibrated extrusion values. So a calibration trial and error campaign is executed in order to find the best extrusion rates for printing spun lines. As is seen on the figure the spun lines do not go to the centre point of the cylinder, this was done as to not have all the spun lines coalesce in this centre. As this could degrade their high longitudinal mechanical properties, by heating up the material in the centre of the cylinder which causes the LCP micro structure to slowly return to their isotropic state.

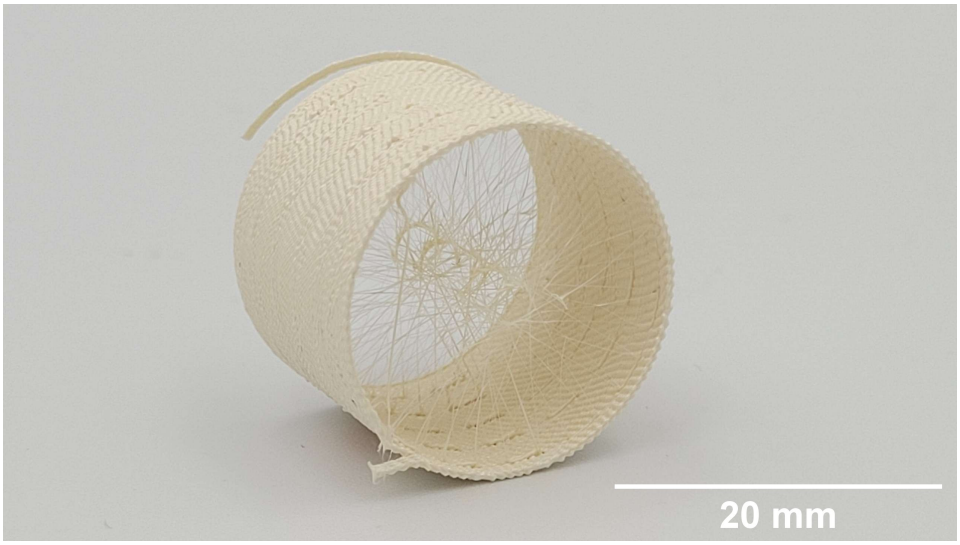

Figure 5.26: Spun LCP lines added in between the layers of a cylinder.

After the integration of the spun lines into cylindrical walls the next step is to take the spun lines and integrate them into the pressure vessel liner print sequence. This is shown in Figure 5.27, where a liner is being printed with integrated spun lines. In terms of spun line printing, the procedure is the same as for the cylinders. The only difference is in the liner with respect to the cylinder. Where the cylinder printing can easily transition to spun line printing, with the liner it is more complicated. As for the sections where the liner is being printed with a certain non zero B axis angle, the liner will have to move back to a vertical position with respect to the nozzle in order to be able to print the spun lines. This means a nozzle move is added between each liner printing sequence and each spun line layer. Finally the spun lines can not be integrated at the bottom of the bottom endcap of the liner. As this will cause interference with the end of the threaded rod, which sticks out from the cylindrical base with respect to the bottom part of the bottom endcap, as can be seen in Figure 5.24b.

5.3.12. Overview of Generating 5-axis Gcode for a Complete Pressure Vessel

In the previous sections all sub components of the printing process of a full additively manufactured LCP pressure vessel have been detailed. Bringing them all together in a single Gcode file is an elaborate process which will be further detailed in this section. Figure 5.28 depicts a flow diagram of the Grashopper file used to generate the pressure vessel Gcodes for the 5-axis printer.

Each sequence in the manufacturing process of a complete pressure vessel is split up into its own block of code, indicated as the blue blocks in Figure 5.28. These sequences are the threaded base, the liner, including the fillet, and the overwrap layers. The overwrap layers are then split up into 90 degree layers, and the variable angle θ layers. Note that the 0 degree layers detailed in subsection 5.3.7 are not used in this code. This is because in the final prints which are discussed in chapter 6 these angles are not present in the designs. Printing the 0 degree lines in the development phase was very useful

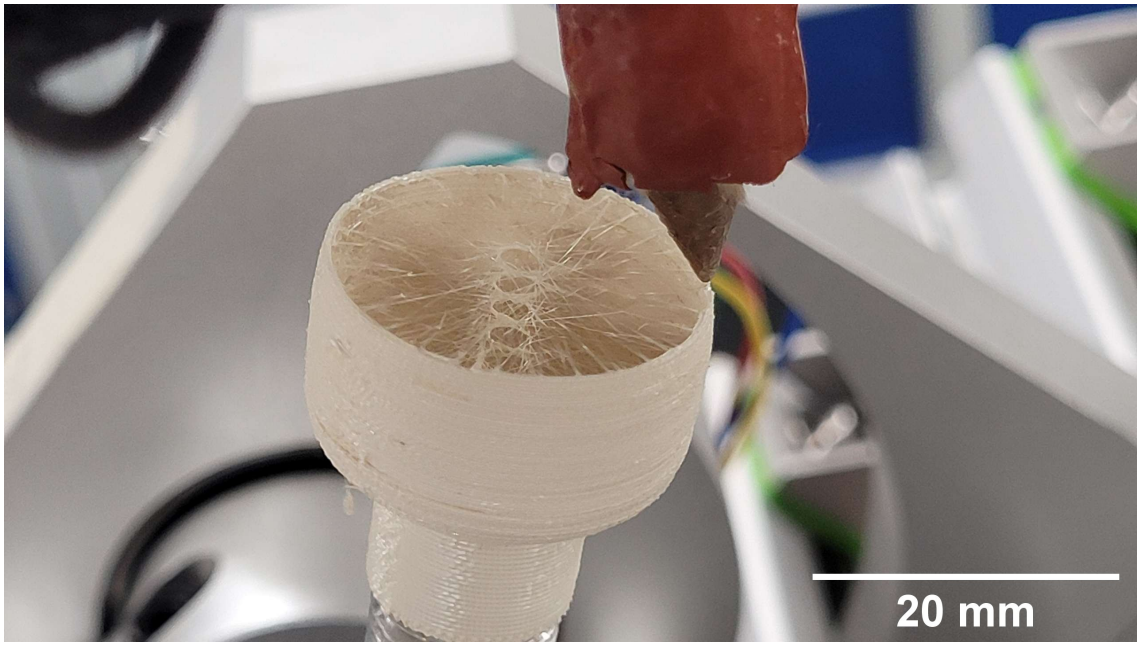

Figure 5.27: Spun LCP lines being printed during the liner wall printing

to uncover missing features in the Gcode and develop the printing process that is also used for the θ degree layers.

Each of the blocks perform a similar process but with different specific features. The similarities are present in the inverse kinematics and post processing modules, which were detailed in subsection 5.3.2. These modules take data from the input parameters like layer width, height, orientation, machine offsets etc, and as main input each inverse kinematics module requires the digital geometry of the current layer. The digital geometry creation is different for each main code block as each layer has different geometry. The base geometry used by all blocks is the pressure vessel base geometry which is created outside of the layer blocks. This base geometry is used to create the liner wall geometry, and afterwards it is used to create the adjusted top endcap geometry (subsection 5.3.6) from which all overwrap layers are created with an offset of one layer height.

The two code blocks used to generate the 90 and θ degree overwrap layers are iteratively used to generate new Gcodes for every subsequent layer in the vessel. An amount of 4 to 8 overwrap layers will be applied in chapter 6 and thus these two overwrap code blocks are iteratively used until all these overwrap layers have generated Gcodes.

Ultimately the Gcodes of the threaded base and the liner are bundled together into one Gcode file. And all the iteratively produced Gcodes of all the overwrap layers are also bundled into one Gcode file. The split of the whole print into these two Gcode files allows for adjustment of the code for the overwrap layers based on the quality of the printed liner, if over or under extrusion is present in the liner or the first overwrap layer the subsequent overwrap layers can be adjusted and a new code is generated for the remaining overwrap layers.

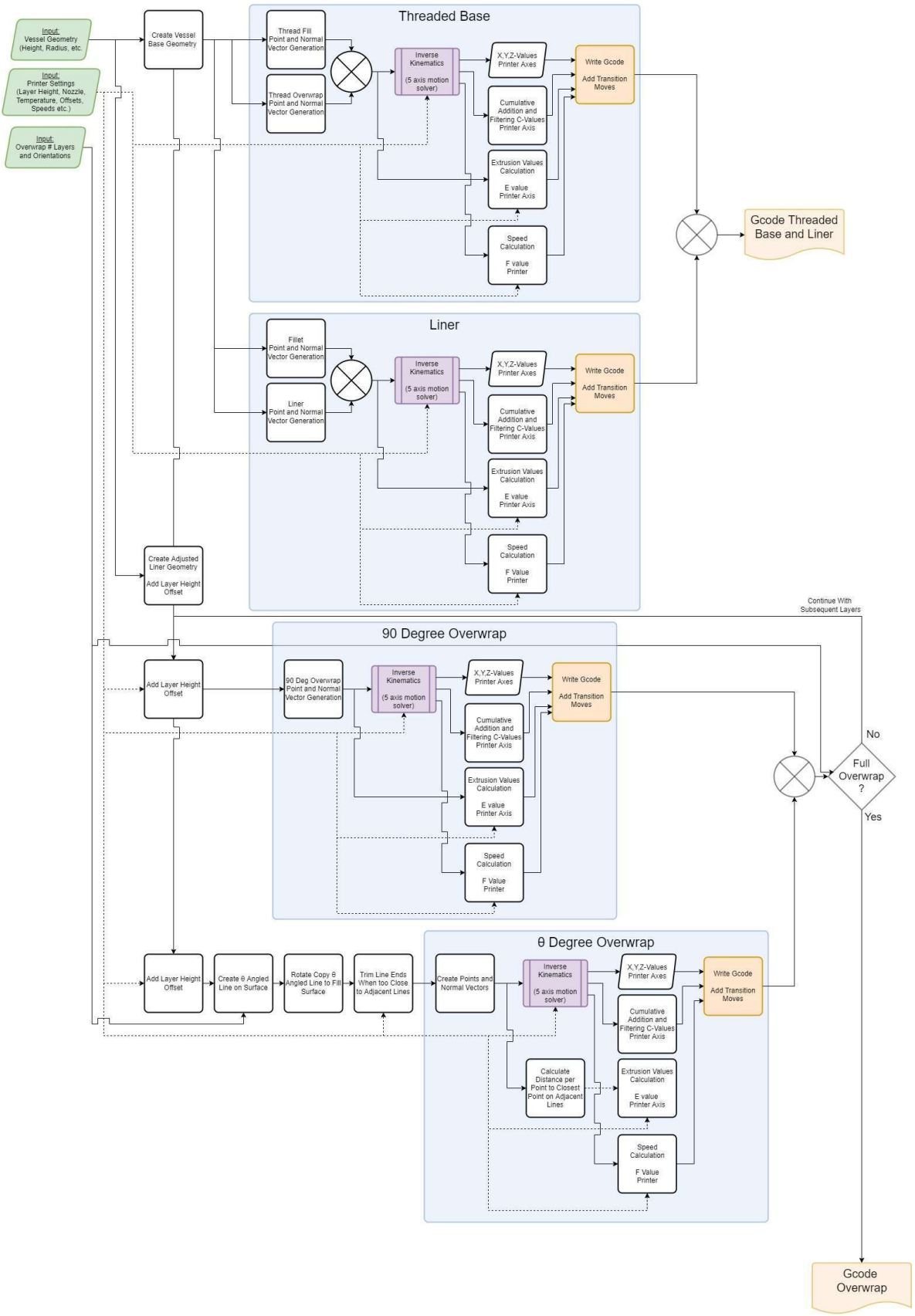

Figure 5.28: High Level Flow Diagram of the Grashopper File to Generate Pressure Vessel Gcodes for the 5-axis printer

6

Pressure Testing of Additively Manufactured Liquid Crystal Polymer Pressure Vessels

To validate the 5-axis Fused Deposition Modelling (FDM) process, established in chapter 5, with Liquid Crystal Polymers (LCP) as a promising material for hydrogen storage, which was investigated in chapter 4, pressure tests are performed on a series of LCP pressure vessels. Initially a small pressure testing campaign is performed to provide proof of basic leak tightness and pressure carrying capability of vessels printed with the methods of chapter 5, this is detailed in section 6.1. After this the test method of the main pressure test campaign is discussed in section 6.2, followed by the design of the pressure testing specimens in section 6.3. In section 6.4 the manufacturing process of the test tanks is presented and any changes with respect to chapter 5 is discussed. The results of these tests are then presented in section 6.5 and discussed in section 6.6.

6.1. Initial Evaluation of Pressure Carrying Capacity of FDM Manufactured LCP Pressure Vessels

The goal of performing the initial pressure testing evaluation is to proof that a simple design LCP pressure vessel manufactured with the 5axismaker can provide a leak tight vessel that can hold a pressure difference. This test can easily be performed by using the high pressure air connection of the Aerospace faculty workshop, making the setup time for this small test campaign short and efficient. The maximum pressure available from this supply is 6 bar, enough to test if the first vessels can hold any pressure at all without leaking.

6.1.1. Initial Evaluation: Sample Design

Four specimens were manufactured for the initial pressure tests. Unfortunately two of the four specimens broke when threading in the pressure connector. The internal thread of the specimens detached from the cylinder around it, rendering it impossible to connect these specimens to the pressure system. These specimens are shown in Figure 6.1. The remaining two specimens did have a good connection between the internal thread and the base cylinder around it.

The specimens shown in Figure 6.1 have the same geometry as the two specimens that were ultimately tested. The threaded base was designed to house a 1/4" thread and has a height of $8mm$. The total specimens are $35mm$ high, and have an internal diameter of $25mm$ with two elliptical endcaps. The two specimens tested have two different laminates, the first specimen has five overwrap layers sequenced as follows:

$$[90/-55/55/90/90]$$

The second specimen has six overwrap layers which are sequenced as follows:

$$[90/-55/55/-55/55/90]$$

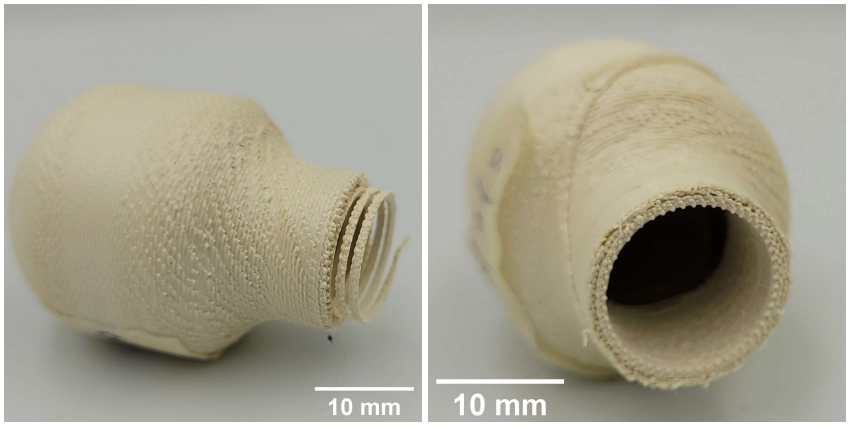

(a) Specimen with partial detached internal thread

(b) Specimen with completely detached thread

Figure 6.1: Two specimens for the initial evaluation with detached internal threads, rendering them impossible to load with pressure.

6.1.2. Initial Evaluation: Test Setup

The test setup for this initial evaluation is based off the compressed air supply present in the workshop of the Aerospace faculty. This air supply provides 6 bars of compressed air and is readily available at a multitude of access points. The test setup is shown in Figure 6.2 and Figure 6.3. A pressure regulator is present, Figure 6.2b to connect the test system to the air supply with control over the applied pressure. This applied pressure is fed through several pressure lines to a valve connecting the test specimen to the pressure system, Figure 6.2a. Additionally a digital pressure sensor is attached to the pressure system via a three way piece. The test specimens are connected to the pressure lines through a 1/4" threaded connection piece, Figure 6.3a. Finally once the testing commences and air pressure is ready to be applied to the test specimen, the test specimen is placed in a plastic container in order to contain any debris from any potential disintegration of the specimen, Figure 6.3b.

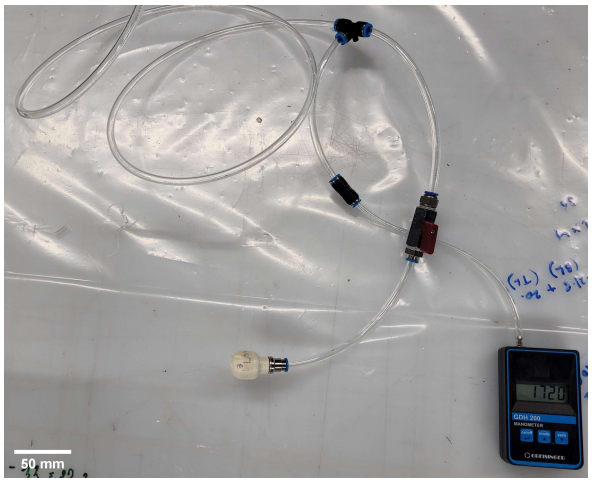

(a) The pressure lines connected to the pressure vessel, the pressure line in the top left feeds to the pressure regulator, figure b, a valve is placed just in front of the pressure vessel. A digital pressure sensor is connected to the system.

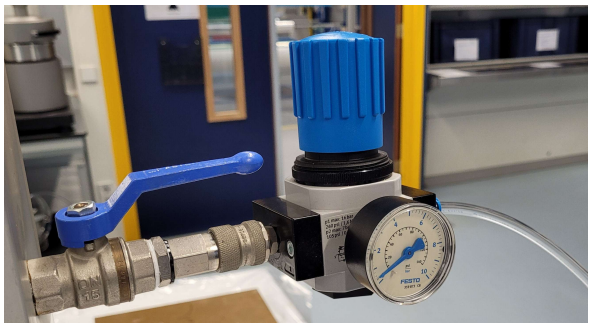

(b) The pressure regulator of the workshop air pressure supply, which feeds to the pressure line system of figure a.

Figure 6.2: Setup of the initial pressure testing

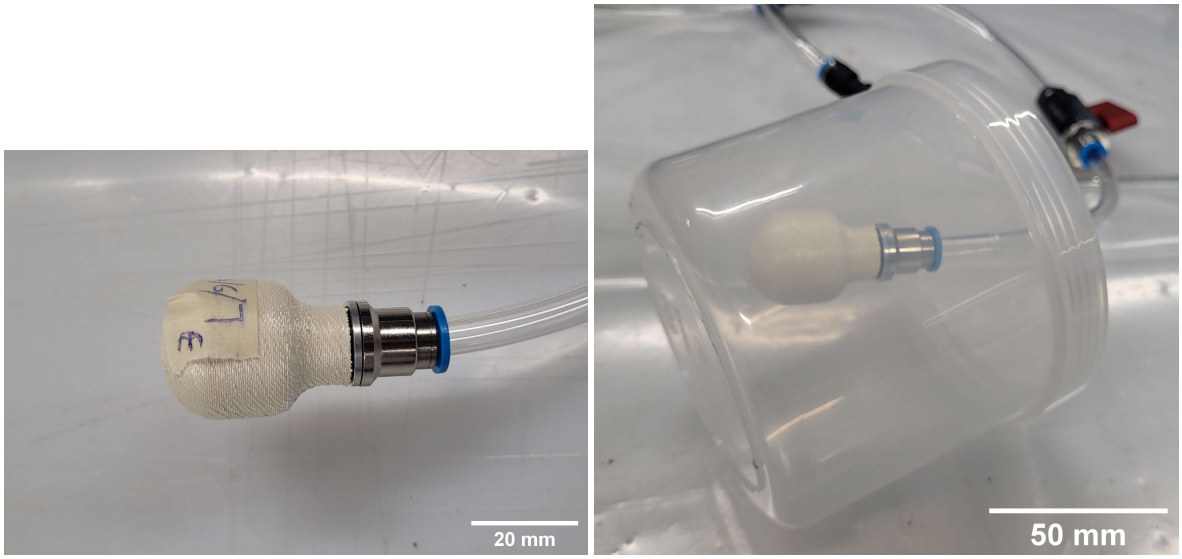

(a) The pressure connection between the pressure tube of the setup and the threaded base of the pressure vessel

(b) The pressure vessel is positioned in a plastic contained in order to contain any debris upon the disintegration of the vessel.

Figure 6.3: Setup of the initial pressure testing, connection of the pressure vessel to the setup

6.1.3. Initial Evaluation: Test Results and Implications

To start the tests the two specimens for the initial pressure tests were connected to the threaded pressure connector. Both these specimens were tested with the workshop high pressure air connection. Specimen one was slowly loaded from atmospheric pressure to higher pressures, until a pressure of roughly 4.4 bar, at which point it broke in the top endcap section. The highest recorded pressure is shown on Figure 6.4b, the failure mode of this specimen is shown in Figure 6.4a.

(a) Failure of the first specimen

(b) The maximum pressure obtained before failure of specimen 1 The pressure on the sensor is absolute pressure, for the applied pressure 1 bar (atmospheric conditions) should be subtracted.

Figure 6.4: Results of the initial specimen pressure testing with workshop compressed air supply.

The second specimen was also slowly loaded from atmospheric pressure to higher pressures, however at a certain point the applied pressure could not be increased anymore. The maximum applied pressure from the workshop supply was reached. At this point the pressure vessel had not failed. An applied pressure of 5.3 bar was reached. With these results it is clear that the specimens show a resistance to pressure loading and can thus be further developed for a higher pressure testing setup. The fact that the second specimen did not fail at 5.3 bar also indicates a higher pressure testing setup is required to fully load specimens with a similar or even stronger design.

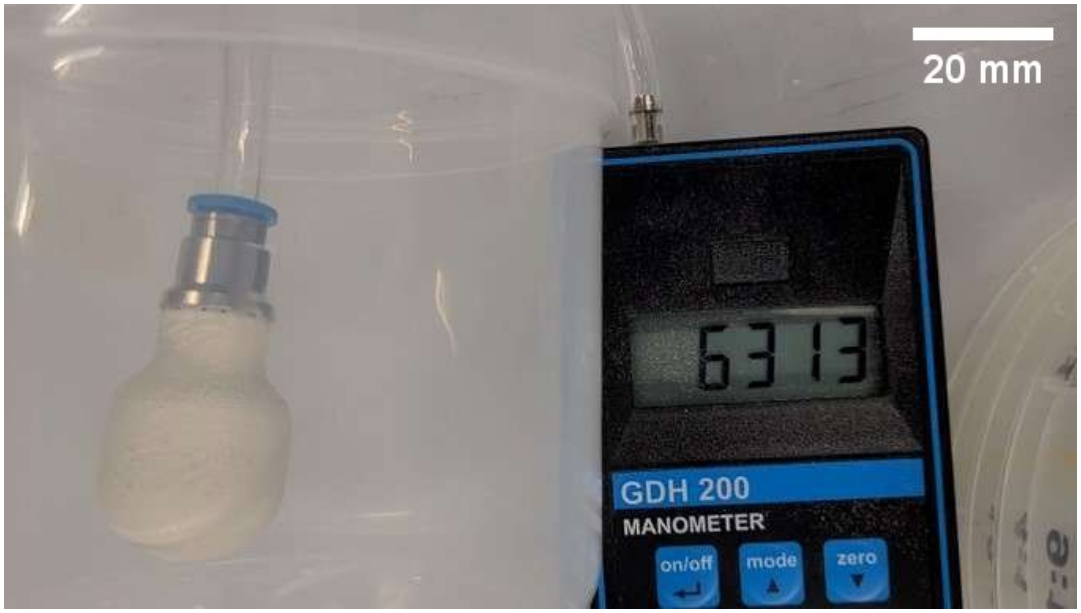

Figure 6.5: The maximum pressure obtained on specimen 2, no failure occurred. The pressure on the sensor is absolute pressure, for the applied pressure 1 bar (atmospheric conditions) should be subtracted. Higher pressures could not be obtained from the workshop air supply.

6.2. Test Method

In order to test the final printed specimens a test setup has to be used that can supply higher pressures than what has been used in the initial pressure tests of section 6.1, as this was limited to a maximum of 5.4 bar. Fortunately within the Delft Aerospace Structures and Materials Laboratory (DASML) a pressurised air vessel of 26 bar is present to supply the autoclave with pressurised air. An additional pressure connection is present on this vessel that could be used for testing the specimens, this pressurised vessel and the used connection are shown in Figure 6.6b. The green tank in the background of the image is the pressurised air vessel, the pressure gauge and valve connect mounted on the tank connect to the grey high pressure air hose used for the test setup. This hose was also fitted with another valve to quickly be able to shut off the air supply to the test system. The test system itself is presented in Figure 6.6a. The grey high pressure air hose connected to the high pressure air vessel comes in on the left of the figure and connects to the specimen and a pressure gauge. The specimen is placed inside a steel cylindrical contained closed off with Plexiglas on the front side for visibility during the test. This container is used to contain any shrapnel and debris from the failed specimens. Specimens that have are connected to a threaded pressure connector similarly to what was done for the initial pressure tests. These pressure connectors allow for a quick swap between specimens during testing.

Specimens are tested until failure by slowly increasing the applied pressure from the valve present on the high pressure vessel in Figure 6.6b. A high speed camera was used to capture the failure event. By placing a pressure gauge in frame of the high speed camera the applied pressure on the vessels can be taken from the high speed footage of this pressure gauge.

(a) The specimens are connected to a high pressure hose inside a steel container, which is covered by Plexiglas on one end for visibility. A pressure gauge is also connected and mounted to the container.

(b) The air supply for the test setup. A maximum of 26 bar compressed air is supplied from this vessel via the grey pressure hose on the left of the figure.

Figure 6.6: High pressure air test setup of printed specimens.

6.3. Test Specimen Design

Ultimately to validate the 5-axis FDM process as viable candidate for pressure vessel manufacturing a testing campaign will be performed. Within this testing campaign the design of the testing samples can be used to showcase and identify specific features of LCP 5-axis FDM printing of pressure vessels. The main features to be tested for are based on utilising the maximum potential of the highly aligned micro-structure of FDM manufactured LCP. The chosen parameters to change between different sets of specimens are the overwrap layer height, overwrap orientations and stacking sequence. Furthermore one set of specimens will be made with spun lines included internally. All of these sets of specimens will be based of a reference design which will also be manufactured. Each type of specimen will be manufactured three times. An overview of all specimen designs is found in Table 6.1, each individual specimen design will be further discussed in Table 6.3 to 6.3. All specimens will have the same liner geometry with a layer height of $0.2mm$ and a threaded base with the following overwrap layers on top of the internal thread: [90/0/90/0], before the fillet is printed on top of it.

Specimen ID:	Layer height Overwrap [mm]	Laminate Overwrap [deg]	Total thickness Overwrap [mm]	Spun lines [Yes/No]	Goal:
R1	0.1	$[90/-55/55/90]_2$	0.8	No	Base design
R2	0.05	$[90/-55/55/90]_2$	0.4	No	Effect of thinner layer height
R3	0.1	$[90/-55/55/90]_1$	0.4	No	Effect of thinner wall
R4	0.1	$[90/-75/75/90]_2$	0.8	No	Effect of anisotropy, less directional optimization
S1	0.1	$[90/-55/55/90]_1$	0.8	Yes	Effect of spun lines

Table 6.1: The designs of all specimens for pressure testing, each specimen is produced three times, with a liner layer height of $0.2mm$. Except S1 which has two liner layers.

Reference design, R1

The reference specimen design, R1, is made up of a standard liner with a print width of $0.4mm$, produced as in chapter 5. This is then covered by eight overwrap layers, with a layer height of $0.1mm$ following the orientation and stacking sequence listed below. The ± 55 degree layers are chosen based on the optimal filament wound laminate design as proposed by Sulaiman et al. [45].

$$[90/-55/55/90]_2$$

This results in an overwrap thickness of $0.8mm$, which adds up to $1.2mm$ nominal wall thickness including the liner. The general dimensions of this reference design are listed below in Table 6.2, and these dimensions are illustrated in Figure 6.7

Parameter:	Value:	Unit:
Internal Diameter Pressure Vessel	25.0	[mm]
Internal Diameter Threaded Base (excl. internal thread)	13.0	[mm]
Length Threaded Base	10.0	[mm]
Length Liner	32.0	[mm]
Thread Pitch	1.34	[mm]
Height Internal Thread	0.89	[mm]
Radius Top Endcap	8.0	[mm]
Radius Bottom Endcap	6.0	[mm]
Radius Fillet	7.0	[mm]

Table 6.2: Reference geometry of the pressure vessels, Figure 6.7 shows the locations of these dimensions

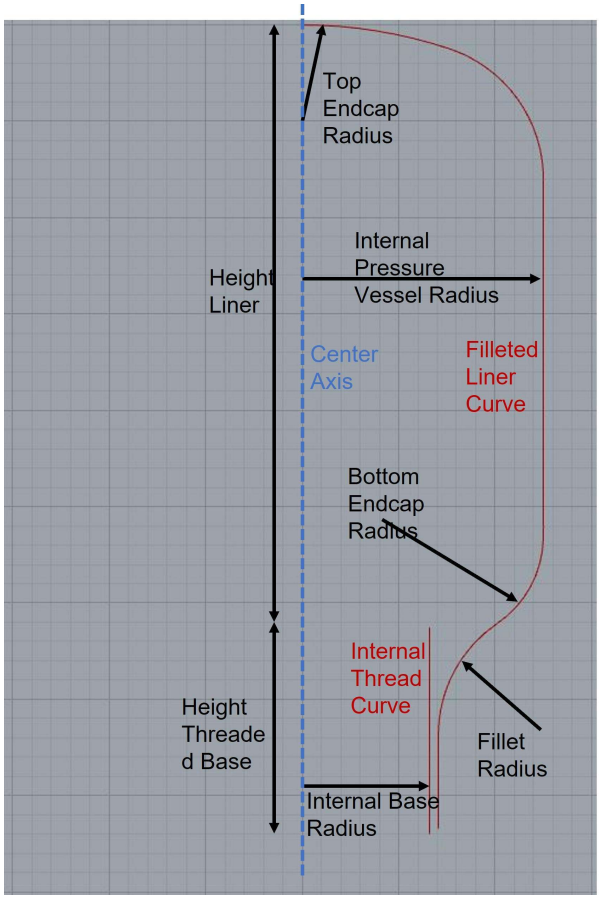

Figure 6.7: Illustration of the reference design

Lower layer height design, R2

Following the references liner geometry of Table 6.3 the main difference of this specimen is the layer height thickness of the overwrap layers. Instead of the $0.1mm$ layer height these overwrap layers will have a layer height of $0.05mm$. This will result in a lower wall thickness, of $0.4mm$, as well which will not make it representable to compare the effect of they layer height with the reference design, R1. However the following specimen, R3, will have the same overall wall thickness as this specimen, as such it will be more representable to compare this specimen to the reduced wall thickness specimen of Figure 6.3. Within this comparison the goal of the reduced layer height specimen is to compare the effect of the layer height on the structural performance of the specimen under pressure loading.

Lower wall thickness design, R3

In order to have a fair comparison specimen design for the thin layer height specimen, R2, this specimen will have the same reduced overwrap thickness of $0.4mm$y. Without changing the layer height with respect to the reference design, R1, this overwrap thickness is achieved by reducing the number of layers from 8 to 4. On top of providing this design in order to compare the lower layer height design, R2, this specimen design also allows to compare the effect of overwrap thickness with the reference design. While still having the same layer height.

Alternate angle design, R4

In order to see the effect of the highly anisotropic LCP print lines a variation in the angled layers of the reference design is made. Instead of ± 55 layer sin the overwrap these angles are changed to ± 75. Otherwise the design and sequence of the layers is the same as the reference design. As such the comparison between these specimen will result in a conclusion about the effect of the angle of the overwrap layers. For an isotropic print material this will have less of a pronounced effect than for a

highly anisotropic print material like LCP. As the ± 55 degree layers are theoretically the best choice for pressure vessels [45], a lower performance of the ± 75 is expected.

Spun lines design, S1

Finally the last specimen design includes spun lines along the liner. A spun line layer is added every $2mm$ in the liner, starting from $3mm$ distance from the end of the threaded base. The last $3mm$ in the length direction in the top endcap does not have a spun lines layer. There are 30 spun lines per layer. Apart from the addition of the spun lines the liner layer is also changed. Due to manufacturing inconsistencies of the liner with the addition of spun lines a second liner layer is added to properly embed the spun line anchors and add stiffness to the liner while still being printed. This means that for every circular liner line being printed a second circle is placed next to it. To still have the same wall thickness the outer overwrap only consists of 4 overwrap layers of $0.1mm$, to obtain a final wall thickness of $1.2mm$ with the two liner layers of $0.4mm$ thick.

6.4. Test Specimen Manufacturing

In this section the manufacturing process for each of the three specimens that are be manufactured per specimen design will be discussed. Any changes with respect to the main process described in chapter 5 will be explained, as well as any discrepancies which occurred during manufacturing of the specimens. The specimens are labelled as follows: R-1-1, where the R-1 indicates reference design 1, following the specimen ID also used in the first column of Table 6.1. The last number indicates the specimen number of that specific design, as each specimen design was manufactured three times.

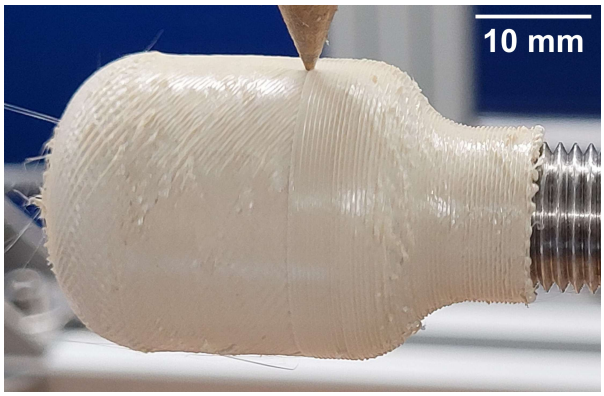

Figure 6.8: Specimen R-1-2 during printing, with a 90 degree layer being printed on top of the 55 layer.

Reference design, R1

Specimen R-1-2 is shown in Figure 6.8, on this figure the specimen is in the middle of the printing of the overwrap layers. The 90 degree layer is being printed, covering the 55 layer below it.

During the printing of the three specimens of the reference design a lot of issues were found with the liner print remaining attached to the threaded base cylinder. Initially the first fillet method presented in subsection 5.3.10 was still used, where the fillet is printed after the liner was completed. For the first specimen of this design, R-1-1, the first method was still used. However for R-1-2 and R-1-3 the second fillet printing method was used, where the fillet is printed parallel to the surface of the threaded base and is printed before the liner. This removed the occurrence of the liner detaching from the threaded base, which occurred a few times during the printing of R-1-1. This meant that this print was started several times.

Other than this, the overwraps were printed following the same sequence as presented in chapter 5. However after the first four overwrap layers quite some overextrusion was present on all three specimens. For these specimens some of these overextrusions were removed by hand with a small knife, before the remainder of the overwrap layers was printed. For the next specimen manufacturing a ironing layer was added halfway through the overwrap layer, to help with removing the overextrusions.

Lower layer height design, R2

For these specimens, apart from the layer height, no changes were made with respect to the printing process of chapter 5. The amount of overextrusion present on these specimens was considerably lower than on the other specimens with the $0.1mm$ layer heights. This could be attributed to the lower layer height, as less material is placed per layer and thus the relative amount of material being extruded with respect to the material already present is reduced. However to support this conclusion dedicated tests should be performed to quantify the amount of overextrusions with varying input parameters for the Gcode generation.

One issue that was present for these specimens was that after the print had finished and when removing the specimen from the threaded base sometimes the internal thread detached at the last revolutions. Because the internal thread is long enough, the end of the cylindrical base can be trimmed in order to still provide sufficient internal thread for connecting the specimen to the pressure test setup.

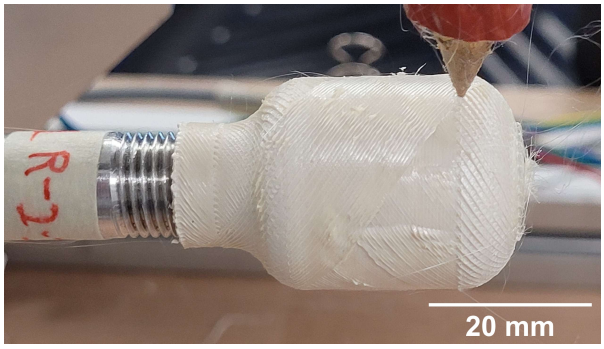

Figure 6.9: Specimen R-2-1 being printed, with the ± 55 layers visible

Lower wall thickness design, R3

In order to solve the issue of the detaching internal threads of the previous specimens, another revolution was added to the start of the internal thread helical. This extra revolution will start and end at the same point and thus create a flat revolution in comparison to the helix. This will ensure that the loose end at the start of the internal thread helical is secured to itself by the flat revolution. This extra revolution has a very small extrusion value compared to the internal thread helical. It just serves to connect the loose end to itself and not fill the entire thread cross section like the internal thread has to do. The extrusion value for this extra revolution is carefully calibrated to be low enough to not interfere with the internal thread itself, but high enough to connect the loose end of the helical to itself. Using this method the specimens detached much better from the threaded rod, without the internal thread detaching from the specimen.

The first specimen of this series, R-3-1, had some issues in the ± 55 layers. What happened was that the pieces of the print lines that are located on the base cylinder detached from this section for about half of the lines of the first -55 layer. This cause underextrusion in these area for the subsequent two layers. To prevent this from happening for future specimens the digital base geometry of these overwrap layers was changed in the Grashopper code. The start of this base curve at the threaded base cylinder was moved inward towards the base cylinder by $0.03mm$. The end point of the base curve on the threaded base was left unchanged, resulting in a slightly lower layer height at the start of the ± 55 layers, but only on the threaded base section. This removed the detaching problem present in R-3-1.

Alternate angle design, R4

The printing sequence of these specimens worked out very well without much issues on the liner or overwrap. However when removing the first specimen, R-4-1, from the threaded rod, the threaded base cylinder detached from the fillet and overwrap layers. This happened because the threaded base was stuck very tightly to the threaded rod, and the torque applied by hang to remove the specimen from the threaded rod was large enough to sever the fillet and overwrap layers from the threaded base cylinder. Afterwards when both parts were removed from the threaded rod, intact but separate, they

were glued back together with structural epoxy. This was done to not waste this specimen, as the fillet, liner and overwrap print came out very good.

The Z height calibration between the nozzle and the threaded rod was changed to include $0.1mm$ more distance between the two at the start of the internal thread printing. This caused the threaded base to have a weaker connection to the threaded rod when removing the specimen from the threaded rod. This worked very well, as both R-4-2 and R-4-3 came off the threaded rod without any issues.

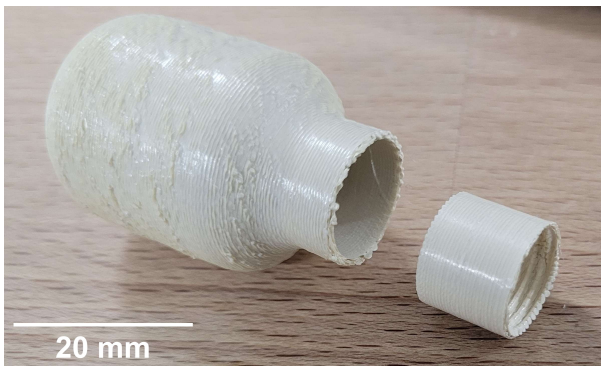

Figure 6.10: Specimen R-4-1 after printing, with the detached inner threaded base cylinder

Spun lines design, S1

As was mentioned in Figure 6.3 the design of the spun lines specimens consists of two adjacent liner walls in order to successfully manufacture the liner including spun lines. Without this addition the high acceleration of the nozzle during spun line printing occasionally causes the force on the lower end of the liner too be too high for the specimen at that point in the print. Which ultimately causes the liner to detach. This failure occurs between two liner layers where a spun line layer is added, indicating that the inter layer strength in these areas is lower than the uninterrupted liner. By adding the second liner layer the liner can survive more loads during printing and therefor be successfully print. In Figure 6.11 specimen S-1-3 is shown during liner printing, the spun lines are clearly visible as well as the double liner wall.

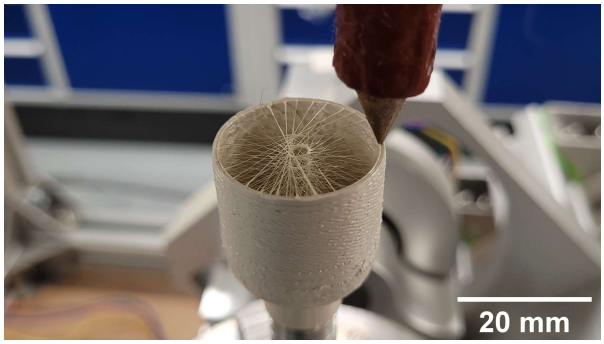

Figure 6.11: Specimen S-1-3 during liner printing, with the double liner wall and spun lines visible

With the addition of the double liner wall specimens S-1-1 and S-1-2 printed without issues. Unfortunately the threaded base detached after printing on specimen S-1-3, in a similar fashion as to what happened in specimen R-4-1, shown in Figure 6.10. The threaded base cylinder was glued back in with structural epoxy.

6.5. Presentation of Pressure Testing Results

Now that all specimens have been manufactured they can be tested following the test method presented in section 6.2. As mentioned before, the specimens are slowly loaded with pressurised air until failure. This is recorded by a high speed camera at 3000 frames per second. The onset of failure for each of

the specimens is shown in Figure 6.12. Apart from the failure of each specimen, this figure also shows the maximum pressure obtained per specimen.

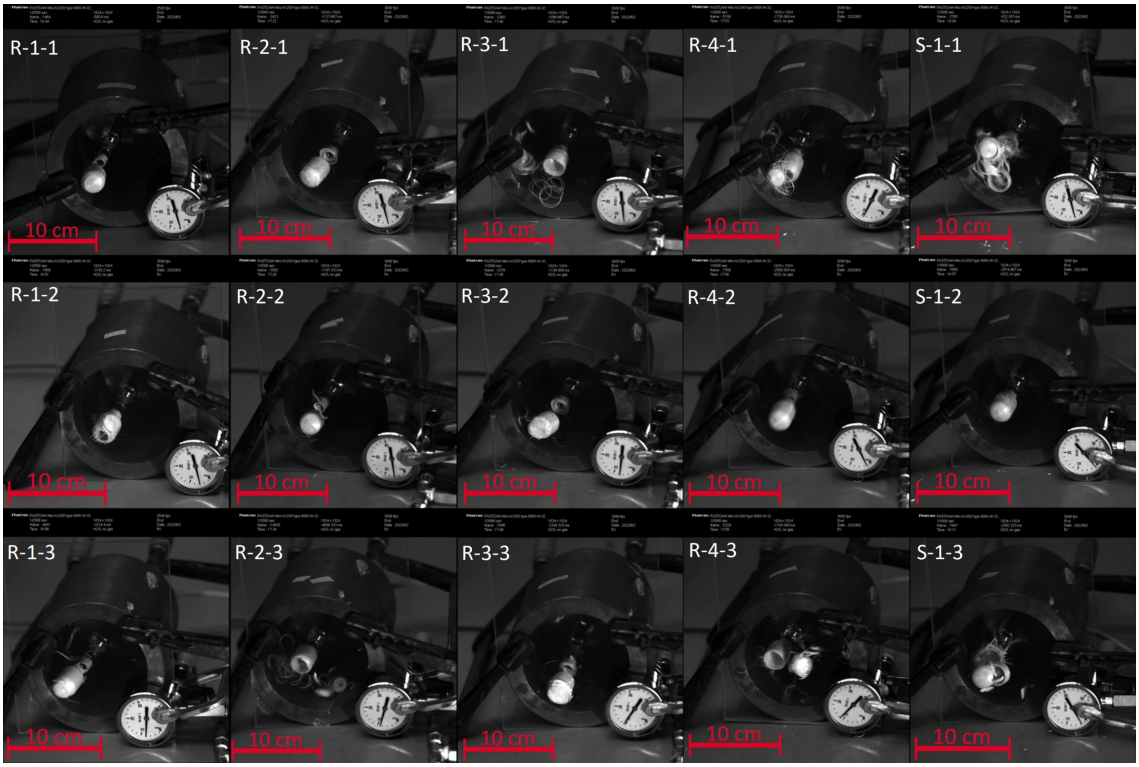

Figure 6.12: Onset of failure of all specimens

Additionally after the tests each specimen was photographed in its failed state, these pictures are shown in Appendix B. These pictures are used together with the pressure results in order to classify the failure mode and use these to assess the printing quality of the specimens in comparison to the obtained pressure. A total of four main failure modes were identified. The four different failure modes are shown in Figure 6.13. The failure modes are (including failure mode abbreviation in brackets): base Cylinder Pull-out [CP], Bottom Endcap failure [BE], Top Endcap failure [TE] and Total Disintegration [TD]. These failure modes and their associated maximum obtained pressures will be discussed further in the following section. Specimen S-1-2 has an unique failure mode that occurred at a low pressure of 2 bar, where a small leak occurred in the centre of the wall. As this failure mode did not occur in any other specimens it was not labelled as a main failure mode, and can be attributed to bad print quality in the overwrap wall.

(a) Specimen threaded cylinder pull-out from the outer overwrap [CP]

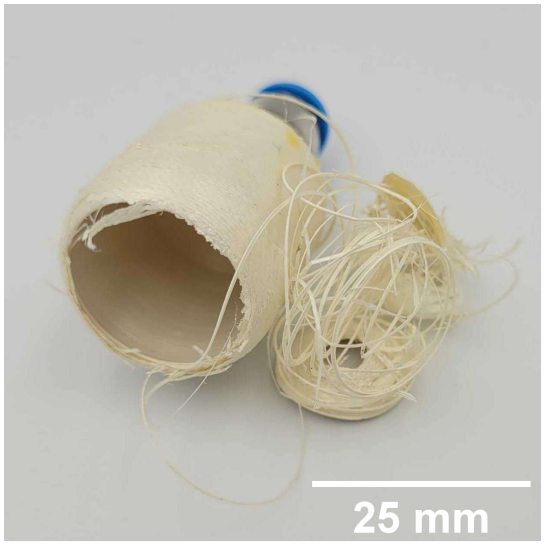

(b) Specimen failed at the top endcap [TE]

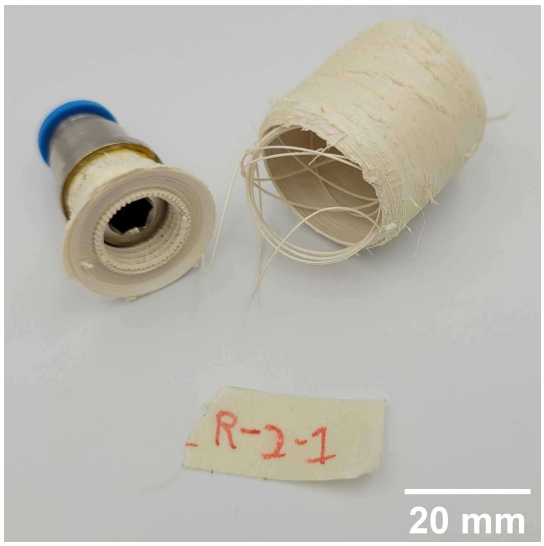

(c) Specimen failed at the bottom endcap [BE]

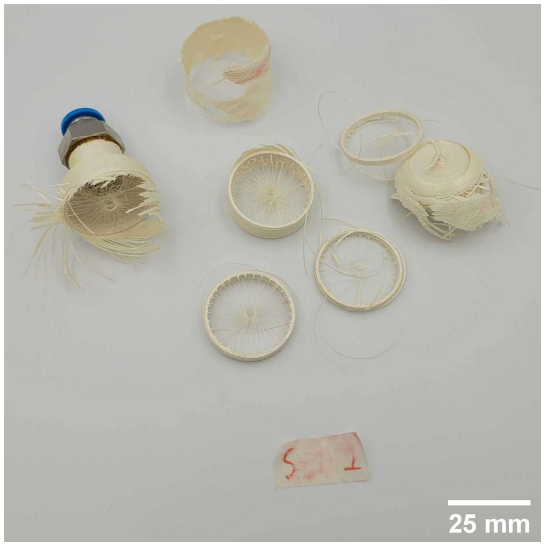

(d) Specimen totally disintegrated upon failure [TD]

Figure 6.13: All identified failure modes

6.6. Discussion of Pressure Testing Results

From Figure 6.12 the maximum pressures are recorded for each specimen and plotted on Figure 6.14 together with a label indicating the failure mode. Furthermore the masses of each specimen, as well as the maximum pressure data are presented in Table 6.3, together with the failure mode labels. The specimens are plotted on this graph in order of manufacturing from left to right, this order also follows the specimen numbering.

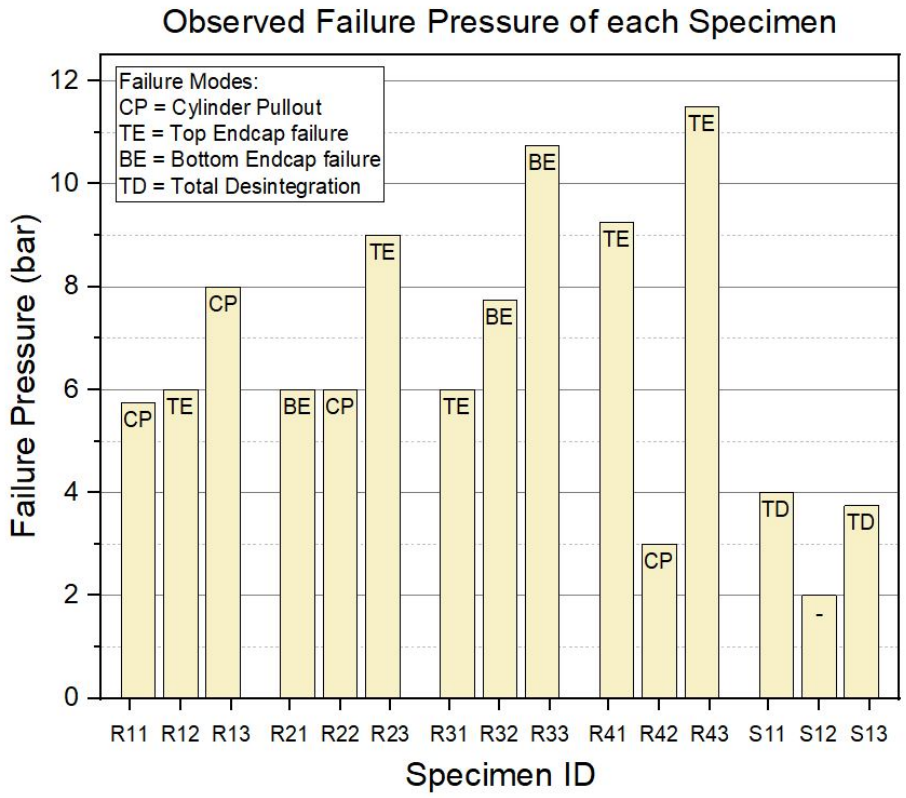

Figure 6.14: Pressure testing results, values indicate observed failure pressure with labels indicating the failure mode

From this data it is clear that all specimens from designs R-1, R-2, R-3 and R-4, except specimen R-4-2, reached maximum pressures between 6 bar and the maximum of 11,5 bar. The specimens with spun lines, S-1, underperfomed compared to the other specimens, reaching only a maximum pressure of 4 bar. The conclusions that can be drawn from this testing campaign will be discussed in the following subsections.

6.6.1. Comparison against theoretical performance

In order to compare the results of the tests to a theoretical estimated performance a netting theory analysis has been performed on the reference design of these specimens. In order to perform this analysis the design is assumed to be for a cylinder under uniform pressure. Furthermore the liner layer is assumed not to take up any load, as it is printed in order to impose the required geometry on the specimen, and the cross sections of these print lines are orientated orthogonal to the cross sections of the overwrap layers. The strength values used for this analysis are taken from the work of Ganteinbein et al. [3]. The maximum tensile strength of the print lines are taken between 260 and 300 MPa, whereas the maximum inter print line shear strength is taken between 25 and 30 MPa. These are reflected in a range of results for the maximum theoretical pressure of the reference design and tabulated in Table 6.4. From this table it is clear that there is about one order of magnitude difference between the

Specimen:	R-1-1	R-1-2	R-1-3	R-2-1	R-2-2	R-2-3	R-3-1	R-3-2	R-3-3
Mass [g]:	5.44	6.30	5.70	4.11	4.07	3.85	4.08	4.07	4.16
Max. Pressure [bar]:	5.75	6	8	6	6	9	6	7.75	10.75
Failure mode:	CP	TE	CP	BE	CP	TE	TE	BE	BE
Specimen:	R-4-1	R-4-2	R-4-3	S-1-1	S-1-2	S-1-2			
Mass [g]:	6.00	6.04	6.07	6.17	6.48	6.31			
Max. Pressure [bar]:	9.25	3	11.5	4	2	3.75			
Failure mode:	TE	CP	TE	TD	-	TD			

Table 6.3: Tabulated mass and maximum pressure results per specimen

failure pressures using tensile strength and shear strength, with the shear strength performing lowest.

	Maximum Pressure Load [bar]	
	Using Print Line Tensile Strength	Using Inter Print Line Shear Strength
Minimum Value:	52	5
Maximum Value:	66	6

Table 6.4: Theoretical failure pressure of the reference design specimens, based on netting theory using tensile strength of single print lines and inter print line shear strength values from the work of Gantebein et al. [3]

Comparing these theoretical failure pressures to the observed failure pressures and failure modes gives an idea of the performance of these vessels as compared to their theoretical capability. Looking at specimens with low failure pressures of 3 to 6 bar, it is clear that these mostly coincide with failure modes engaging in inter print line shear failure. Comparing these failure pressures to the theoretical values of Table 6.4 of 5 - 6 bar these are of comparable value. This shows that the inter print line shear mode is the weak point in such a pressure vessel design, future designs should take this into account and aim to prevent any load case where print layers are loaded in shear. Currently the interface between the threaded base and the overwrap layers are solely loaded in inter print line shear and will thus always form a weak point.

On the other hand the failure modes and pressures of the specimens that obtained the highest pressures did not come close to the theoretical maximum pressures when looking at the print line maximum tensile strength. The most likely cause for this is the fact that the print lines are not sharing the loads between each other as optimally as in a composite. As the netting theory used for these theoretical calculations assume a composite is used wherein the matrix does not carry the load but make sure that the stresses are smoothed out between individual fibres. This does not happen as much in LCP print lines, and therefor the failure pressure could be lower than expected. Furthermore the following sections will discuss additional reasons why the performance of these specimens is lower than expected.

6.6.2. Influence of Variations between Specimen Designs

The five different specimen designs were originally intended to vary parameters in design and asses the effect of these parameters with this pressure testing campaign. Unfortunately no significant trends based on these parameters can be identified, other than the under performance of the spun line specimens. For example the difference in design between the R-1 series and the R-2 series is that R-2 has a lower layer height for the same overwrap design, resulting in half the wall thickness of the overwrap layers. This is also reflected in the masses of these specimens, the R-2 specimens are almost $2g$ lighter than the R-1 specimens. However this is not reflected in the pressure results, as the R-2 specimens performed slightly better than the R-1 specimens. Where it would be expected that the R-1 specimens perform better if the wall thickness difference would have had an effect without anything else being changed. In reality the printing quality difference between these specimens most likely cause

the discrepancy between expected performance and the real performance.

Comparing specimen series R-2 and R-3 to each other should provide insight in the effect of layer height, as these specimens have the same wall thickness but different layer heights. Where R-2 has a layer height of $0.05mm$ and R-3 has a layer height of $0.1mm$. While maintaining the same wall thickness this means that R-3 has half the number of overwrap layers as compared to R-2. The specimens all have a mass of around $4.0g$ indicating the fact that they have the same wall thickness. Looking at the pressure results shows that the specimens of R-3 perform slightly better than R-2, this would indicate that the thicker layer height has an improved effect on the performance of these specimens. Although the difference is not substantial, more specimens should have to be tested in order to accurately asses the effect of layer height.

The parameter that was changed in specimen series R-4 with respect to series R-1 is the angle of the print lines in the overwrap layers. The overwrap design of these two series are identical in stacking and layer heights, however the angles of half of the layers are altered. Where R-1 follows the following sequence:

$$[90/-55/55/90]_2$$

On the other hand R-4 follows the sequence:

$$[90/-75/75/90]_2$$

From literature [45] the theoretical optimal angle for pressure vessels in a filament winding design is 55 degrees. Therefor comparing R-1 to R-4 theoretically means that R-1 will perform better if all else remains equal. This is not what is seen in the results of these tests, as the R-4 series has the highest performance of all specimens, but also one of the lowest performing specimens. This makes it impossible to make any conclusion on the effect of the overwrap angle.

Finally the spun lines series, S-1, can be compared against the reference series R-1, as they have the same wall thickness. The S-1 series has the addition of the spun lines, which were expected to increase the performance of the specimen. Unfortunately the S-1 series performed the worst of all specimen series. Looking at the failure modes that occurred the specimens failed by complete disintegration, where every layer of the specimen has failed and in some cases detached from its adjacent layer. This can be seen especially well in Figure 6.13d where the liner layers with the embedded spun lines are still intact, but they detached from each other on the interface between a liner layer with and without the added spun lines. This indicates that the inter layer adhesion between a liner layer that has spun lines and the subsequent liner layer printed on top is of far lower strength than that of a normal liner on liner layer without spun lines. Due to this poor inter layer adhesion the spun lines might not have been loaded in tension at all, and thus have not alleviated any of the stresses in the wall. Which was the intended goal of these spun lines.

6.6.3. Influence of the Printing Process and Quality

As has been mentioned in the previous subsection some failures of the specimens were caused by poor printing quality. Furthermore no significant trends based on design parameters were observed other than the under-performance of the spun lines specimens. But even this can be attributed due to poor printing quality, although in this case it is more inherent to the printing sequence design. On the other hand a clear trend is seen in the printing sequence of the specimens. Looking at Figure 6.14, where the specimens are plotted left to right in order of being printed, left being the first, right being the last specimen produced. If the outliers of R-4-2 and the S-1 series are ignored then a clear trend of increasing strength along the printing order can be seen. This can be attributed to a learning curve with respect to manufacturing the specimens. Even though the specimens are manufactured by an automated 5 axis printer, this printer does not take into account any printing quality effects and does not adjust for any discrepancies. This adjusting is done by the operator by adjusting extrusion values and calibrations of the printer before a printing file is started. By printing over 15 specimens the calibration of these parameters become more intuitive and therefor led to increased quality of the prints.

Furthermore in most cases when a specimen failed with the cylinder pull out failure mode this occurred at relatively low pressures compared to other specimens in the same series. R-1-3 being the exception, as it reached the highest pressure of its specimen series. But for all other cylinder pull out failures the failure can be attributed to poor inter layer adhesion on the interface where it failed between the cylinder and the overwrap layers on top.

7 Discussion

7.1. Results

With the results presented on the permeability testing and pressure testing comes an end to this thesis. The hydrogen permeability results of the additively manufactured LCP specimens indicate that this material, in its additively manufactured form, is well suited to be used as a hydrogen gas barrier material. Showing only a two to four times increase in the value with respect to the bulk permeability properties provided by the manufacturer. With more research into this topic these values can be further decreased with better understanding of the phenomenon. Furthermore the permeability measured on the additively manufactured specimens outperform all other polymers, commonly used as liner materials, with respect to permeability in their bulk form.

The results from pressure testing validate the potential for using these techniques and material as a method for manufacturing pressure vessels. With the highest pressure obtained reaching 11,5 bar without any structural optimisation having taken place this paves the way for higher pressures resistance in the future. However the large spread in maximum obtained pressure throughout the 15 tested tanks show that the printing quality is not consistent enough at this point for reliable performance. The failure modes indicate clear weak spots in the design and manufacturing that can be accounted for in future iterations.

7.2. Conclusion

From the main research question of this thesis, established in section 3.2, three sub questions were posed that will be reflected upon in the following concluding discussion.

7.2.1. Permeability Study of Additively Manufactured Liquid Crystal Polymers

The first sub question was posed to fill the knowledge gap of the permeability of additively manufactured specimens.

- How can additively manufactured liquid crystal polymers provide sufficient hydrogen gas permeability for the use in a hydrogen gas pressure vessel?

This was investigated with a permeability testing campaign on a set of additively manufactured LCP specimens. The design of the layer sequence of these specimens was obtained from a microscopy study in order to maximise the barrier properties against hydrogen gas. Six specimens were tested for permeability with gaseous hydrogen at an applied pressure of 300 bar. The results show a small decrease in permeability as compared to the bulk LCP permeability properties as provided by the manufacturer. When further comparing the permeability performance against other polymers commonly used as liner materials in Composite Overwrapped Pressure Vessels (COPV) the additively manufactured LCP outperforms all of these polymers. Concluding that the material itself can be used as a barrier material against hydrogen permeation. Combined with the excellent mechanical properties in its anisotropic printed form this provides a unique opportunity to combine the function of the separate liner and composite overwrap materials in a COPV into one material when manufacturing pressure vessels with LCP.

7.2.2. Development Study of Additive Manufacturing of Liquid Crystal Polymer Pressure Vessels

The second sub question of this thesis was related to bridging the gap between state of the art 5-axis Fused Deposition Modelling (FDM) and printing of LCP pressure vessels in a single process.

- How can 5 axis fused deposition modelling be used with liquid crystal polymers in order to manufacture linerless pressure vessels in a one step process?

The work in this thesis proves it is possible to manufacture pressure vessels form LCP with 5-axis FDM. The process of creating such a vessel is broken down into separate printing sequences in order to manufacture a pressure vessel, starting with a threaded connection as a base point, followed by an internal wall to provide the first shape and ultimately topped of by overwrap layers of any desired orientation and stacking sequence of print lines. To end up with such pressure vessels with the printing equipment used in this thesis requires many calibration steps and even then this can still lead to a failed print. This failure prone printing sequence asks for constant observation by the operator, which is a very time intensive task for the operator.

A series of 15 test pressure vessels were manufactured in order to validate the proposed manufacturing method for pressure vessels. With varying designs the pressure vessel with the highest performance reached a failure pressure of 11,5 bar. Compared to the theoretical expected performance these vessels do not reach the maximum potential when considering the tensile strength of the print lines. However when looking at the failure modes at low failure pressures, based on inter print line shear failures these occur at pressures expected from the theoretical analysis. These specimens were lacking the required printing quality between the failed layers, which resulted in a weak point of the pressure vessels that prevented the main vessel walls from being optimally loaded. If such drops in quality can be circumvented the failure pressures of these pressure vessels can be more consistent and at higher levels.

7.2.3. Development Study of novel Structural Improvements with 5-axis Fused Deposition Modelling

From the initial literature study and research planning the aim was to test the 5-axis printing method on novel pressure vessel geometries and structural improvements, as stated in the research question below. However due to time constraints this ended up only being tested for structural improvements and not the geometrical improvements.

- Is it possible to manufacture novel pressure vessel geometries, including new structural strengthening elements, that have a higher structural performance than conventional pressure vessels?

Three of the 15 pressure vessels that were tested included spun lines internally. The aim of these three specimens was too show the effectiveness of using internal structures to carry the stresses induced by the pressure load. These spun lines are very effective in tension and will therefore theoretically take up a lot of the stress if positioned internally in the pressure vessel walls. Unfortunately the results of the pressure tests on these three specimens showed a large drop in performance as compared to the pressure vessels without spun lines. When analysing the failure modes of the spun line pressure vessels it was clear that the vessels disintegrated in the liner wall on the interface between layers that contain a spun line layer. This indicates that the inter layer adhesion between liner layers with spun lines added is of a reduced quality compared to liner layers that do not include spun lines. If this inter layer adhesion is improved and thus the anchoring of the spun lines is better integrated into the pressure vessel walls, then the spun lines could proof to substantially increase the performance of these vessels.

As mentioned previously due to time constraints it was not possible to test geometrical optimisations of the pressure vessel designs. A great potential of this manufacturing method is to manufacture pressure vessel designs with maximised use of the available geometry in the location where it will be installed. With the printing procedures developed for cylindrical pressure vessels in this thesis it is also possible to manufacture unconventional pressure vessel geometries, however working this out in creating the gcode for such pressure vessels proved too be too much work to fit inside the scope of this thesis.

7.3. Significance of Current Work

With the permeability research performed in this thesis a start is made into the understanding of permeability of additive manufactured parts. To the writer's knowledge no research has been performed on this topic until now. The results presented for the hydrogen permeability of additively manufactured LCP show the possibility of using this material in its additively manufactured form as a barrier material for hydrogen permeation in pressure vessel applications. The specimens used for this analysis are limited to a single design of layer orientations and sequence, which means that the permeability results are solely applicable to this design. Further permeability results on additively manufactured specimens can be performed with the results of this thesis as a starting point.

The printing process for pressure vessels developed in this thesis provides a first of a kind process for manufacturing pressure vessels in a single process. Starting with the threaded base the full pressure vessel can be printed in a single process. Something which can not be done for metallic vessels, which require fabrication and assembly of several parts, or composite vessels, which required the fabrication of a liner followed by filament winding of the laminate. This new additive manufacturing process can be further developed for larger scale pressure vessels in order to save on manufacturing steps and costs as compared to state of the art pressure vessels. Furthermore by using additive manufacturing pressure vessel can be designed and manufactured on an individual basis, not required specific tooling or moulds for a series production. This allows tailor made pressure vessels to be produced in low volumes while not loosing out on any start up costs present in traditional manufacturing methods.

As was mentioned earlier, the aim of this thesis was to also test geometrical optimisation of pressure vessels, but this wasn't possible due to time constraints. However this aim does touch upon a very promising feature of this manufacturing technique. State of the are manufacturing methods for COPV are limited to axis symmetric shapes like cylinder or spheres. Whereas with 5-axis additive manufacturing shapes can be created that are not axis symmetric, or even symmetric at all, that can still be strong enough to withstand the pressure in all critical areas. As long as the geometrical optimisation goes hand in hand with the structural design, such that stress constraints due to an asymmetric geometry can be taken up by adding extra layers or print lines. The possibility of printing unconventional pressure vessel geometries are large, especially for gasses with low volumetric density like hydrogen. By using more of the available volume inside the vehicle in which the pressure vessel is placed, like for example an aircraft hull or wing, the volume of gas carried on board can be increased without needing to add extra pressure vessels or increase the shape of the vehicle. The work in this thesis provides a promising starting point for the development of such non conventional pressure vessel geometries.

8 Outlook

In this chapter both the limitations of the current work, section 8.1, and the recommendations to future work,section 8.2, will be presented.

8.1. Limitations of Current Work

The limitations of the current work can be split up into three main areas, the 5-axis Fused Deposition Modelling (FDM) printer setup (subsection 8.1.1), the FDM manufactured Liquid Crystal Polymers (LCP) specimens tested for hydrogen permeability (subsection 8.1.3), and the 5-axis FDM manufactured LCP pressures vessel specimens tested under pressure (subsection 8.1.2).

8.1.1. Limitations of the 5-axis FDM Printer Setup

With the current setup the parts printed for this thesis are at the edge of what is possible in terms of precision. With layer heights of $0.1mm$ the required spatial resolution of the printer movements is in the same order of magnitude. The $0.1mm$ variations originate mainly in the combination of the B and C axis being placed on the baseplate instead of the print head, as well as the global stiffness of the 5axismaker frame and Z axis gantry. The combination of these elements, together with the use of a metallic threaded rod for the printing of the threaded pressure vessels leads to a positional variation of about $0.1mm$. This value is only reached after careful calibration of all rotation axes and carefully zeroing in the X, Y and Z axes by eye.

Furthermore the nozzle and print head setup used in the work of this thesis is severely limited in possible maximum temperatures. With the printing of LCP temperatures of up to $340°$C can be used. However with this long nozzle a significant portion of the input heat generated by the heating block in the print head is lost in the relatively large mass of the nozzle. Ultimately leading to a $10°$C to $20°$C drop in temperature between the heating block and nozzle. Initially this was solved by increasing the heating block temperature by $20°$C, however when print temperatures in the range of $330°$C or $340°$C are desired the maximum heating capacity of the heating block is reached. With the current setup the heating block does not go beyond $340°$,C resulting in a $320°$C to $330°$C temperature at the tip of the nozzle.

As mentioned in subsection 5.3.2 the range of motion of the B axis is limited to only 180 degrees. This causes issues at both ends of the range when either printing the top endcap of the liner or when printing normal to the fillet in an overwrap mode. In both cases the ideal nozzle angle with respect to the workpiece is larger than what the B axis range can provide, as such the nozzle angle does not follow the ideal orientation for these print layers. Within this thesis this is solved by continuing to print with an offset angle nozzle, as these offset angles are always smaller than 45 degrees it is still possible to print these sections without the use of support material. However as was seen in subsection 5.3.6 the liner print with an offset angle nozzle causes the printed geometry to be offset from the intended digital geometry. By increasing the range of motion of the B-axis this could be solved, thereby increasing the accuracy of the printed parts and decreasing the processing work to account for these inconsistencies in the current Gcodes.

8.1.2. Limitations of the 5-axis FDM Manufactured LCP Pressure Vessel Specimens

Due to the focus of this thesis on developing the setup and process of 5-axis printing of pressure vessels, there was no work spent on optimising the design of the pressure vessel design printed for testing. This resulted in sub optimal designs that were focused on manufacturability but not structural or geometric performance. This was reflected in the results of the pressure tests on the 15 specimens. None of the specimens came close to the theoretical maximum failure pressure due to sub optimal printing quality and an un-optimised design. Looking at the performance of the specimens including internal spun lines, further shows the effect of low print quality on the structural performance. By adding the spun lines in the wall of the pressure vessels, this reduced the strength of the wall itself. Ultimately creating a weak point. Due to time constraints this could not be further improved in order to effectively load the spun lines without weakening the pressure vessel wall.

8.1.3. Limitations of the FDM Manufactured LCP Specimens Tested for Hydrogen Permeability

Due to the available resources for this thesis project it was not possible to perform extensive permeability tests. Therefor only one design specimen was tested, which did validate the use of additively manufactured LCP as a gaseous hydrogen barrier material. However this design was only limited to a specific set of chosen manufacturing parameters, including, layer height, layer width, layer stacking orientations and sequence, printing temperature and annealing program. Through the microscopy analysis of the effects of these parameters the most optimal combinations of these parameters was selected and used for the permeability testing. However the individual effects, that any of these individual parameters had, was lost in this testing plan. Therefore it is not possible at this stage to attribute the permeability value of these specimens to any specific manufacturing parameters that were used in the design of these specimens. It could be the case that only a subset of the chosen parameters affect permeability while the others do not.

8.2. Recommendations for Future Work on this Topic

Similarly as in the previous section, the recommendations to the work in this thesis can be split up into three areas, the 5-axis FDM setup, subsection 8.2.1, the improvements and possibilities to the design of parts manufactured on the 5-axis FDM printer, subsection 8.2.2 and finally recommendations on the hydrogen permeability testing of additively manufactured LCP, subsection 8.2.3. Many of these recommended improvements were already considered during the execution of the practical work of this thesis, however due to either time or resource constraints they were not feasible to be implemented in the work of this thesis.

8.2.1. Recommended Improvements to the 5-axis FDM printer

In subsection 8.1.1 the limitations in terms of accuracy, precision and calibration process of the current 5-axis FDM setup are presented and discussed. Fortunately a multitude of ways exist to improve the precision, accuracy and calibration process of the current 5-axis FDM setup. First of all, the X,Y and Z axes all have a zero probe point to which they can return and trigger a switch which sends a signal to the controller that the axes has reached the zero point. However for the X axis the switch itself is occasionally bent out of place by the movement of the X axis. Furthermore, the B and C axis in the baseplate setup do not have such switches, therefor they need manual zeroing every time the printer is turned off. Improving the mechanical quality of the X axis switch and adding zero switches to the B and C axis will greatly improve the speed and accuracy of the calibration process of the printer.

Furthermore by placing the threaded rod in the three chuck vice of the C axis, or any other bracket or baseplate support for that matter, the zero point of this part will always need to be calibrated independently of the machine zero point. Currently the only way to this is again by hand and visual confirmation. Human precision in such a scenario can only go so far, thus it would be beneficial for the precision of the printer to add a probing system. This probing system would be able to accurately measure the location and orientation of a workpiece with respect to the machine or the nozzle for example. Measuring the orientation of a workpiece, the threaded rod of this thesis for example, would also allow to measure the angular misalignment of its fit in the three chuck vice of the C axis. This misalignment data can then be used to offset the geometry when generating the Gcode. As such any offset and variation while

rotating the C axis can digitally be accounted for. This would greatly decrease the amount of under and overextrusion that occurred while printing on the threaded base.

Finally a major upgrade that can be made to the printer and printing process to improve the quality of printing and reducing the required input of the operator is to use in-situ process monitoring and control. By monitoring the print lines after they have been put down and comparing these to the expected digital geometry this allows the printer to correct any inconsistencies at a later pass. For example print lines that have been under extruded can be filled up by extra print lines that are generated for this purpose. Or the adjacent print lines can intentionally be over extruded in order to fill the gap between the new print line and the old under extruded print lines. The same process can also be applied for layer heights and the general geometrical inconsistencies. This process monitoring can be achieved by optically visualising the print lines. Or by using non destructive techniques that penetrate into the part and detect discrepancies into the part, not just the surface layer. Furthermore the nozzle exerted in the nozzle on the exiting print line can be monitored to finely adjust the extrusion parameters in real time and print lines that are exactly matching the intended dimensions.

8.2.2. Recommended Improvements and Possibilities of the Design of 5-Axis FDM Manufactured Pressure Vessels

Because the practical work in thesis on developing the printing setup and procedures of 5-axis FDM took more time than anticipated, there was no time left to include any work on the structural design and optimisation of the printed pressure vessels. However the potential of 5-axis FDM printing in terms structural optimisation is far greater than what is shown among the results of this thesis. This potential can be split up into two parts, improvements to the current pressure vessel designs and manufacturing approach, and the possibilities of printing highly optimised and novel structural designs.

In the design of the pressure vessels tested for this thesis not much time could be spent on the structural design of these specimens. Developing the manufacturing process was the priority. As such many improvements can be made to increase the structural efficiency of these pressure vessels. First of all the angled overwrap layers do not form the most optimal paths over the endcaps.

Another issue that was encountered often on these pressure vessels were related to the way the threaded connection was used to pressurise the vessels. The threads themselves detached partially or completely on several prints. Furthermore the industry standard methods of sealing such threaded connections could not be applied here. As these threads were non tapered, normally an O-ring or dowty seal is applied to seal against a flat surface. However the bottom of the threaded cylinder of the printed pressure vessels did not provide such a flat surface for sealing. Alternatively a tapered thread is an option to seal against, however as the threaded rod which was used as mould did not have a tapered thread this could not be included in the design. If the threaded rod includes a tapered thread, and if it is carefully aligned with the start of the print then the digital geometry can easily be printed for such a tapered thread. Another way of solving this issue is by removing the threaded connection from the printed part, and instead place a threaded insert into the print. This insert can be custom made in order to have additional features for mechanical interlocking and maximum adhesion between the insert and the printed material. With a 5-axis FDM setup it is possible to print over this insert on all sides except the side on which it is supported. This allows for great accessibility of the nozzle to mechanical interlocking features on all sides. Using such an insert would remove the issues with threaded sealing, as it can follow industry standard regulations for sealing.

In the final specimen series spin printing was included to increase the structural efficiency of the pressure tanks. However due to time constraints it was not possible to fully integrate these spun lines into the structure effectively. More time can be spent into calibrating the spinning process and anchoring the line into the pressure vessel walls. This will greatly increase the effect of these lines, such that the overall structural performance of these pressure vessels will be improved significantly.

With the Gcode generation workflow that was used for this thesis it will also be possible to adapt the software to include point or vector clouds of a highly optimised structure. These structures could be optimised for specific pressure loading cases with the material properties and anisotropy of FDM printed LCP in mind. With the high effective steering radius of 5-axis FDM printing the possibility of optimising pressure loaded structures are very large. Instead of the limited winding angles in COPVs, additively manufactured pressure vessels could have optimised wall structures of variable angles and thickness at any point in the geometry. This allows a structure to be designed with all material being loaded equally and thus increase the structural efficiency.

Similarly the geometries of printed pressure vessels can also be further optimised. In this thesis a simple axis-symmetric structure was designed and printed, also in order to simplify some of the processes in the Gcode generation. However with the 5-axis FDM printer it is possible to print any shape pressure vessel, within the motion ranges of the printer axes of course. This allows pressure vessel geometries to be optimised for its available enclosing volume and be manufactured in one process. Possible geometries could be for example, internal tanks in aircraft wings or fuselage sections, tanks in compartments of cars, trucks or trains and many more.

8.2.3. Recommended Improvements on Design and Testing of Gaseous Hydrogen Permeability of FDM Manufactured LCP

In subsection 8.1.3 the limitations of the current investigation into the hydrogen permeability of additively manufactured LCP is presented. From these limitation it will be greatly beneficial in the future development and design of additively manufactured LCP to understand the effect of its micro and macro structure on its gaseous hydrogen barrier properties. Many possible parameters affecting the permeability should independently be tested in order to further validate and understand the use of additively manufactured LCP as a hydrogen gas barrier material. This would allow to further tailor the micro structure to increase the permeability properties, while also understanding the effect that changing parameters for structural efficiency has on the permeability. Potentially the research in the permeability of additively manufactured LCP could also be used to characterise and validate other common additive manufacturing materials as gas barrier materials.

In the current permeability testing campaign only one specimen was tested that has not been annealed. Because of the great potential of creating hydrogen storage vessels with LCP without annealing, it would be beneficial to increase the knowledge on the effect of annealing on the permeability of additively manufactured LCP. Without annealing the energy requirements during manufacturing are greatly reduced as a prolonged high temperature annealing process is not required. The energy requirements for such a process can become very high when the parts increase in size and wall thickness. Furthermore leaving out annealing in LCP parts allows for greater recyclability, something that is very important in a future circular economy.

Bibliography

[1] L. Ulke-Winter and L. Kroll, “Holistic criteria-based optimization of filament wound high pressure vessels,” *CIRP Journal of Manufacturing Science and Technology*, vol. 18, pp. 173–178, 2017, ISSN: 1755-5817. DOI: https://doi.org/10.1016/j.cirpj.2017.01.002. [Online]. Available: https://www.sciencedirect.com/science/article/pii/S1755581717300032.

[2] CompositesWorld, *Carbon fiber in pressure vessels for hydrogen*, https://www.compositesworld.com/articles/cfrp-pressure-vessels-for-hydrogen, Accessed: June 2022, 2020.

[3] S. Gantenbein, K. Masania, W. Woigk, J. P. Sesseg, T. A. Tervoort, and A. R. Studart, “Three-dimensional printing of hierarchical liquid-crystal-polymer structures,” *Nature*, vol. 561, no. 7722, pp. 226–230, 2018, ISSN: 14764687. DOI: 10.1038/s41586-018-0474-7.

[4] H. Zhao, Q. Wang, and L. Fulton, “A Comparison of Zero-Emission Highway Trucking Technologies,” *UC Office of the President: University of California Institute of Transportation Studies*, 2018. DOI: 10.7922/G2FQ9TS7.

[5] Clean Sky 2 Joint Undertaking and Fuel Cells and Hydrogen 2 Joint Undertaking, *Hydrogen-powered aviation - A fact-based study of hydrogen technology, economics, and climate impact by 2050*, May. 2020, ISBN: 9789292463427. DOI: 10.2843/766989.

[6] S. T. Pribyl and J. M. Haines, “Future Fuels in the Maritime Sector – Building the Bridge to Hydrogen,” *Holland & Knight Energy and Natural Resources Blog*, 2021. [Online]. Available: https://www.hklaw.com/en/insights/publications/2021/04/future-fuels-in-the-maritime-sector-building-the-bridge-to-hydrogen.

[7] B. R. Murray, “Characterisation of rotationally moulded polymer liners for low permeability cryogenic applications in composite overwrapped pressure vessels,” Ph.D. dissertation, 2016, p. 301. [Online]. Available: http://hdl.handle.net/10379/6036.

[8] R. Barth, K. Simmons, and C. San Marchi, “Polymers for Hydrogen Infrastructure and Vehicle Fuel Systems : Applications , Properties , and Gap Analysis,” Tech. Rep. October, 2013, p. 52.

[9] B. Flaconnèche, J. Martin, and M. Klopffer, “Permeability, Diffusion and Solubility of Gases in Polyethylene, Polyamide 11 and Poly(vinylidene fluoride),” *Oil & Gas Science and Technology*, vol. 63, no. 1, pp. 9–19, 2008. DOI: 10.2516/ogst:2001023. [Online]. Available: http://ogst.ifpenergiesnouvelles.fr/articles/ogst/abs/2008/01/ogst07042/ogst07042.html.

[10] A. F. Ismail, K. C. Khulbe, and T. Matsuura, *Gas separation membranes: Polymeric and inorganic*. 2015, p. 340, ISBN: 9783319010953. DOI: 10.1007/978-3-319-01095-3.

[11] T. Graham, “XVIII. On the absorption and dialytic separation of gases by colloid septa,” *Philosophical Transactions of the Royal Society of London*, vol. 156, pp. 399–439, 1866. DOI: 10.1098/rstl.1866.0018.

[12] H. Fujiwara, H. Ono, K. Onoue, and S. Nishimura, “High-pressure gaseous hydrogen permeation test method -property of polymeric materials for high-pressure hydrogen devices (1)-,” *International Journal of Hydrogen Energy*, vol. 45, no. 53, pp. 29 082–29 094, 2020, ISSN: 03603199. DOI: 10.1016/j.ijhydene.2020.07.215. [Online]. Available: https://doi.org/10.1016/j.ijhydene.2020.07.215.

[13] Y. Su, H. Lv, W. Zhou, and C. Zhang, “Review of the Hydrogen Permeability of the Liner Material of Type IV On-Board Hydrogen Storage Tank,” *World Electric Vehicle Journal*, vol. 12, no. 3, p. 130, 2021, ISSN: 20326653. DOI: 10.3390/wevj12030130.

[14] *ASTM D1434-82. Standard Test Method for Determining Gas Permeability Characteristics of Plastic Film and Sheeting*, West Conshohocken, PA, USA, 2009. DOI: 10.1520/D1434-82R09E01.

[15] B. Flaconnèche and M. Klopffer, "Transport Properties of Gases in Polymers: Experimental Methods," *Oil & Gas Science and Technology*, vol. 56, no. 3, pp. 245–259, 2001. DOI: 10.2516/ogst:2001022. [Online]. Available: http://ogst.ifpenergiesnouvelles.fr/articles/ogst/abs/2008/01/ogst07042/ogst07042.html.

[16] P. Adams, A. Bengaouer, B. Cariteau, V. Molkov, and A. G. Venetsanos, "Allowable hydrogen permeation rate from road vehicle compressed gaseous storage systems in garages; part 1 - introduction, scenarios and estimation of an allowable permeation rate," p. 15, 2011.

[17] M. J. Robinson, "Determination of allowable hydrogen permeation rates for launch vehicle propellant tanks," *Journal of Spacecraft and Rockets*, vol. 45, no. 1, pp. 82–89, 2008, ISSN: 15336794. DOI: 10.2514/1.29709.

[18] S. K. Mital, J. Z. Gyekenyesi, S. M. Arnold, R. M. Sullivan, J. M. Manderscheid, and P. L. Murthy, "Review of Current State of the Art and Key Design Issues With Potential Solutions for Liquid Hydrogen Cryogenic Storage Tank Structures for Aircraft Applications," *Nasa-Tm-2006-214346*, no. October, pp. 3–21, 2006.

[19] Celanese, *Vectra LCP Design Guide*, 2013.

[20] C. Houriet, "Additive Manufacturing of Liquid Crystal Polymers," Master's Thesis, TU Delft, 2019, p. 111.

[21] R. J. Young and P. A. Lovell, *Introduction to Polymers*, Third. CRC Press, 2011, pp. 421–424, ISBN: 9781439894156. DOI: 10.1201/b15405-5.

[22] A. A. Handlos and D. G. Baird, "Processing and Associated Properties of In Situ Composites Based on Thermotropic Liquid Crystalline Polymers and Thermoplastics," *Journal of Macromolecular Science, Part C*, vol. 35, no. 2, pp. 183–238, 1995, ISSN: 15205746. DOI: 10.1080/15321799508009637.

[23] A. I. Isayev, "Self-Reinforced Composites Involving Liquid-Crystalline Polymers: Overview of Development and Applications," *ACS Symposium Series*, vol. 632, pp. 1–20, 1996, ISSN: 00976156.

[24] E. A. Sabol, A. A. Handlos, and D. G. Baird, "Composites based on drawn strands of thermotropic liquid crystalline polymer reinforced polypropylene," *Polymer Composites*, vol. 16, no. 4, pp. 330–345, 1995, ISSN: 15480569. DOI: 10.1002/pc.750160411.

[25] R. W. Gray IV, D. G. Baird, and J. H. Bøhn, "Effects of processing conditions on short TLCP fiber reinforced FDM parts," *Rapid Prototyping Journal*, vol. 4, no. 1, pp. 14–25, 1998, ISSN: 13552546. DOI: 10.1108/13552549810197514.

[26] R. W. Gray IV, "The Effects of Processing Conditions on Thermoplastic Prototypes Reinforced with Thermotropic Liquid Crystalline Polymers," Master's Thesis, Virginia Polytechnic Institute and State University, 1997, p. 165.

[27] B. Smith and L. M. Anovitz, "Lifecycle Verification of Polymeric Storage Liners," Oak Ridge National Laboratory, Tech. Rep., 2013, pp. 154–159.

[28] S. Ando, S. Sato, and K. Nagai, "Gas Permeation and Barrier Properties of Liquid Crystalline Polymers," *Polymers and Polymeric Composites: A Reference Series*, pp. 523–547, 2019. DOI: 10.1007/978-3-642-37179-0_67-1.

[29] B. W. Grimsley, R. J. Cano, N. J. Johnston, A. C. Loos, and W. M. McMahon, "Hybrid composites for LH2 fuel tank structure," *International SAMPE Technical Conference*, vol. 33, no. September, p. 13, 2001.

[30] E. G. Gordeev, A. S. Galushko, and V. P. Ananikov, "Improvement of quality of 3D printed objects by elimination of microscopic structural defects in fused deposition modeling," *PLoS ONE*, vol. 13, no. 6, 2018, ISSN: 19326203. DOI: 10.1371/journal.pone.0198370.

[31] J. Mireles, A. Adame, D. Espalin, *et al.*, "Analysis of sealing methods for FDM-fabricated parts," *22nd Annual International Solid Freeform Fabrication Symposium - An Additive Manufacturing Conference, SFF 2011*, no. January, pp. 185–196, 2011.

[32] S. Gantenbein, C. Mascolo, C. Houriet, *et al.*, “Spin-Printing of Liquid Crystal Polymer into Recyclable and Strong All-Fibre Materials,” 2021.

[33] Ø. K. Grutle, “Designing a 5-axis 3D Printer,” *Department of Informatics*, vol. Masters, p. 96, 2015.

[34] G. Fang, T. Zhang, S. Zhong, X. Chen, Z. Zhong, and C. C. Wang, “Reinforced FDM: Multi-axis filament alignment with controlled anisotropic strength,” *ACM Transactions on Graphics*, vol. 39, no. 6, 2020, ISSN: 15577368. DOI: 10.1145/3414685.3417834.

[35] Y. Li, K. Tang, D. He, and X. Wang, “Multi-Axis Support-Free Printing of Freeform Parts with Lattice Infill Structures,” *CAD Computer Aided Design*, vol. 133, no. July, 2021, ISSN: 00104485. DOI: 10.1016/j.cad.2020.102986.

[36] H. Shen, H. Diao, S. Yue, and J. Fu, “Fused deposition modeling five-axis additive manufacturing: machine design, fundamental printing methods and critical process characteristics,” *Rapid Prototyping Journal*, vol. 24, no. 3, pp. 548–561, 2018, ISSN: 13552546. DOI: 10.1108/RPJ-05-2017-0096.

[37] M. A. Isa and I. Lazoglu, “Five-axis additive manufacturing of freeform models through buildup of transition layers,” *Journal of Manufacturing Systems*, vol. 50, no. October 2018, p. 12, 2019, ISSN: 0278-6125. DOI: 10.1016/j.jmsy.2018.12.002. [Online]. Available: https://doi.org/10.1016/j.jmsy.2018.12.002.

[38] J. A. Gardner, T. Nethercott-Garabet, N. Kaill, *et al.*, “Aligning material extrusion direction with mechanical stress via 5-axis tool paths,” *Solid Freeform Fabrication 2018: Proceedings of the 29th Annual International Solid Freeform Fabrication Symposium - An Additive Manufacturing Conference, SFF 2018*, pp. 2005–2019, 2020.

[39] T. Zhang, X. Chen, G. Fang, Y. Tian, and C. C. Wang, “Singularity-Aware Motion Planning for Multi-Axis Additive Manufacturing,” *IEEE Robotics and Automation Letters*, vol. 6, no. 4, pp. 6172–6179, 2021, ISSN: 23773766. DOI: 10.1109/LRA.2021.3091109. arXiv: 2103.00273.

[40] D. Chakraborty, B. Aneesh Reddy, and A. Roy Choudhury, “Extruder path generation for Curved Layer Fused Deposition Modeling,” *CAD Computer Aided Design*, vol. 40, no. 2, pp. 235–243, 2008, ISSN: 00104485. DOI: 10.1016/j.cad.2007.10.014.

[41] Netherlands Organisation for Applied Scientific Research (TNO), *Hydrogen permeability test facilities*, Facility Location: Ypenburg, The Netherlands, 2022.

[42] E3D, *Hemera direct kit*, https://e3d-online.com/products/e3d-hemera-direct-kit-1-75mm, 2022.

[43] Non-Palanr XYZ by Kupol Inc., *Elongated nozzles*, https://www.nonplanar.xyz/nozzles, 2022.

[44] Linux CNC, *5-axis kinematics*, http://linuxcnc.org/docs/devel/html/motion/5-axis-kinematics.html, Accessed: November 2021, 2022.

[45] S. Sulaiman, S. Borazjani, and S. H. Tang, “Finite element analysis of filament-wound composite pressure vessel under internal pressure,” *IOP Conference Series: Materials Science and Engineering*, vol. 50, no. 1, 2013, ISSN: 17578981. DOI: 10.1088/1757-899X/50/1/012061.

A

Extended Data Permeability Testing

A.1. Pictures of Permeability Testing Specimens After Testing

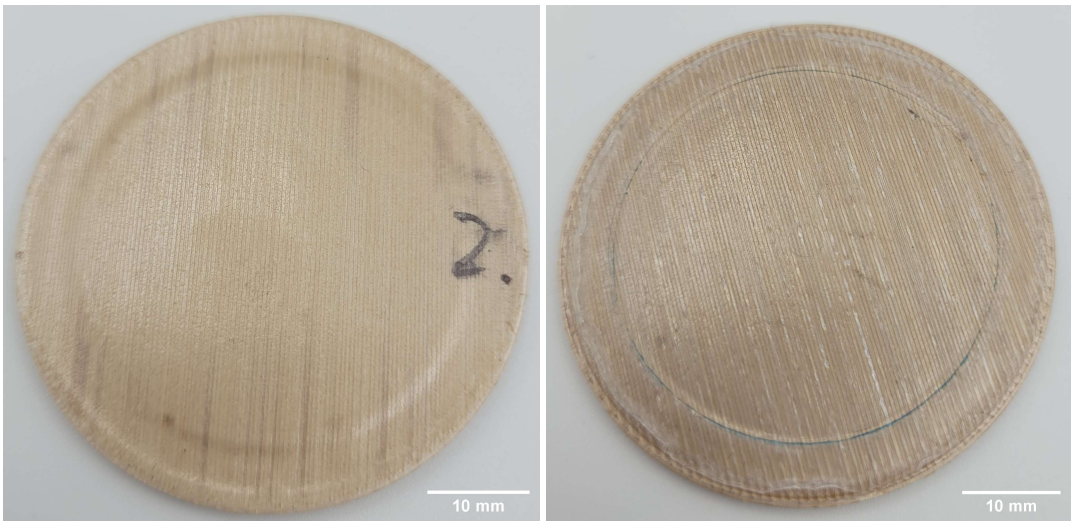

(a) Front side (b) Back side

Figure A.1: Permeability specimen number 2

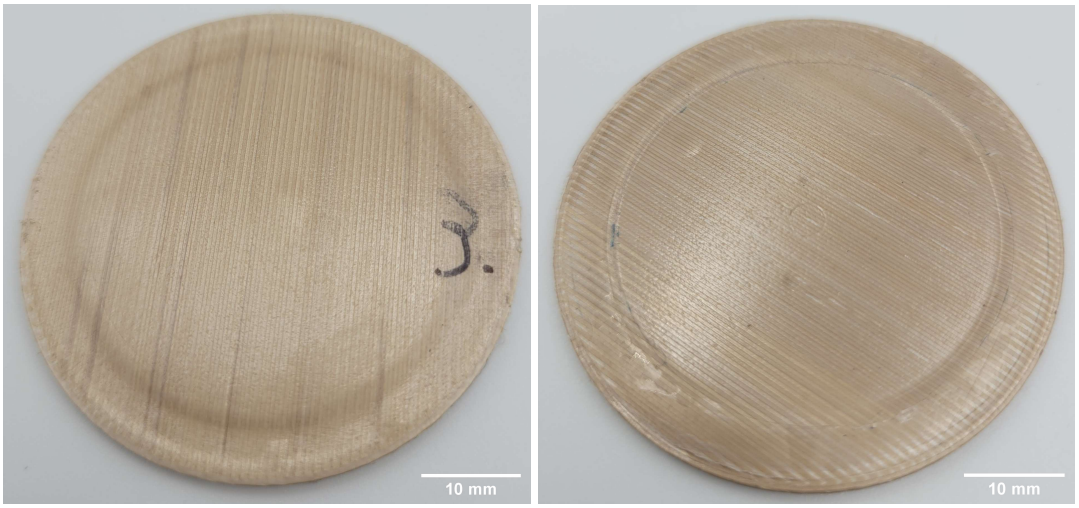

(a) Front side (b) Back side

Figure A.2: Permeability specimen number 3

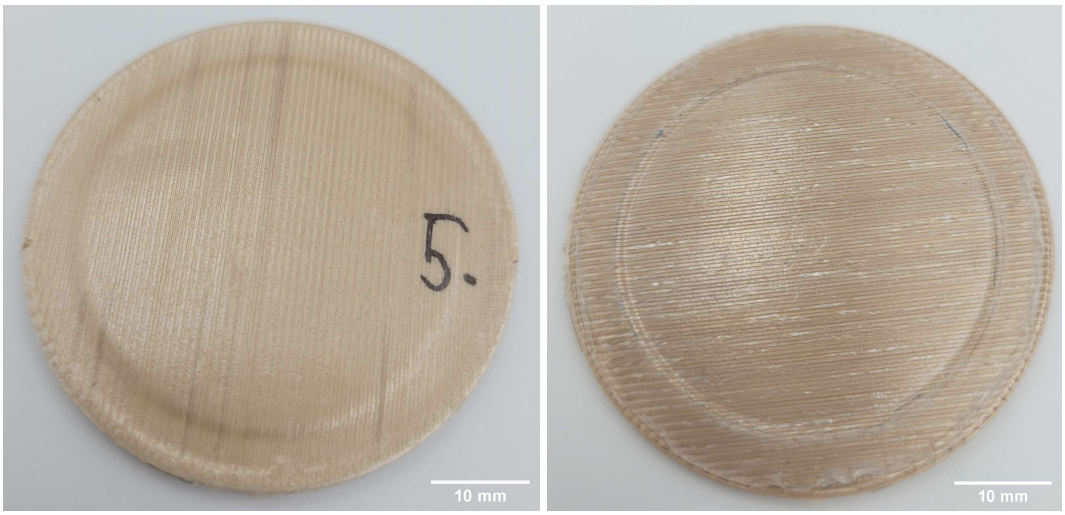

(a) Front side (b) Back side

Figure A.3: Permeability specimen number 5

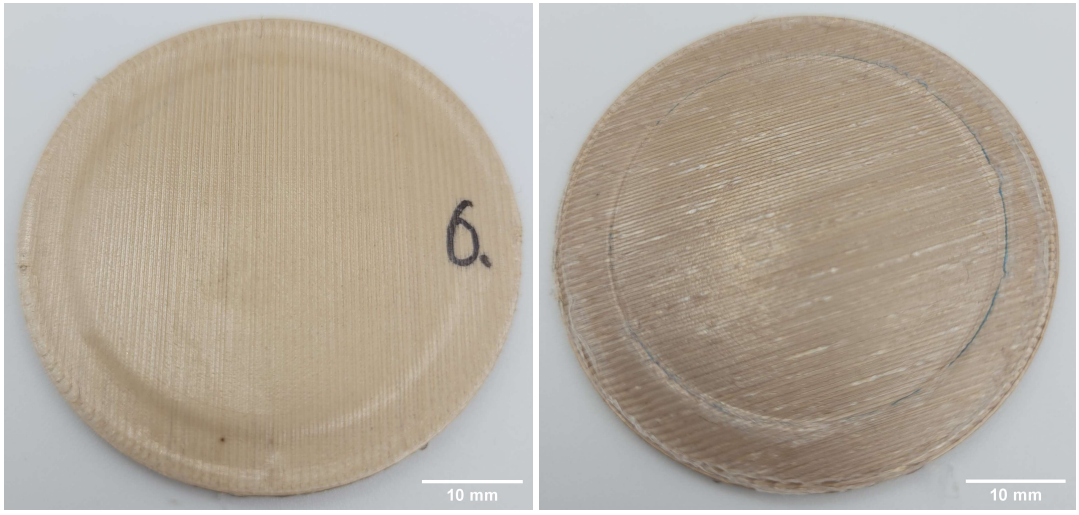

(a) Front side (b) Back side

Figure A.4: Permeability specimen number 6

(a) Front side (b) Back side

Figure A.5: Permeability specimen number 8

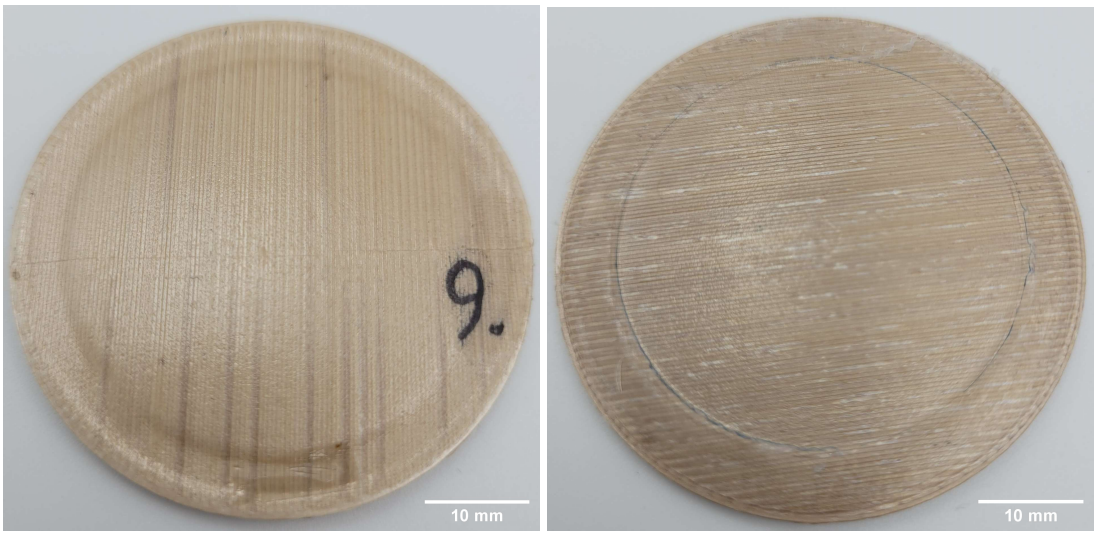

(a) Front side (b) Back side

Figure A.6: Permeability specimen number 9

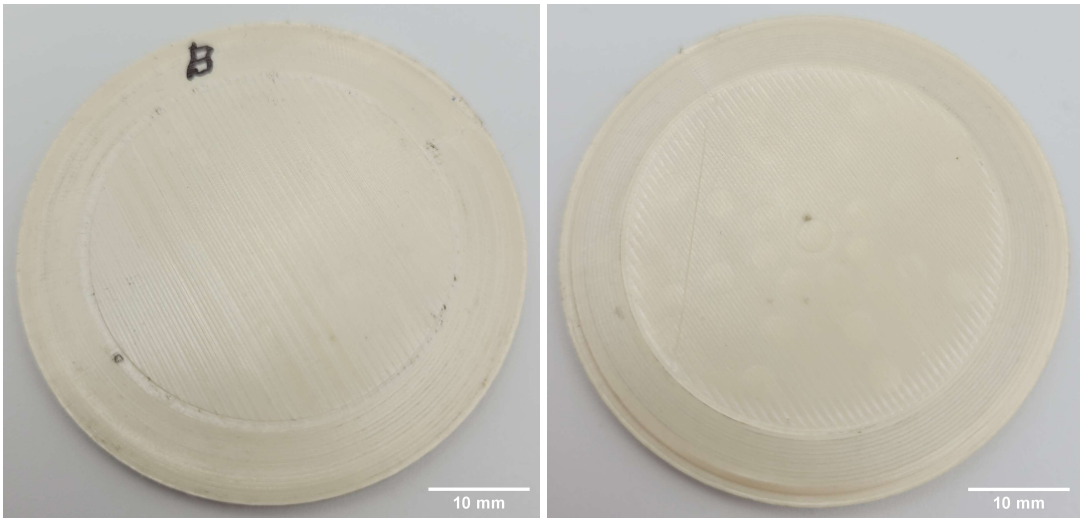

(a) Front side (b) Back side

Figure A.7: Permeability specimen B, the single unannealed specimen successfully tested

A.2. Unprocessed Results of Permeability Tests

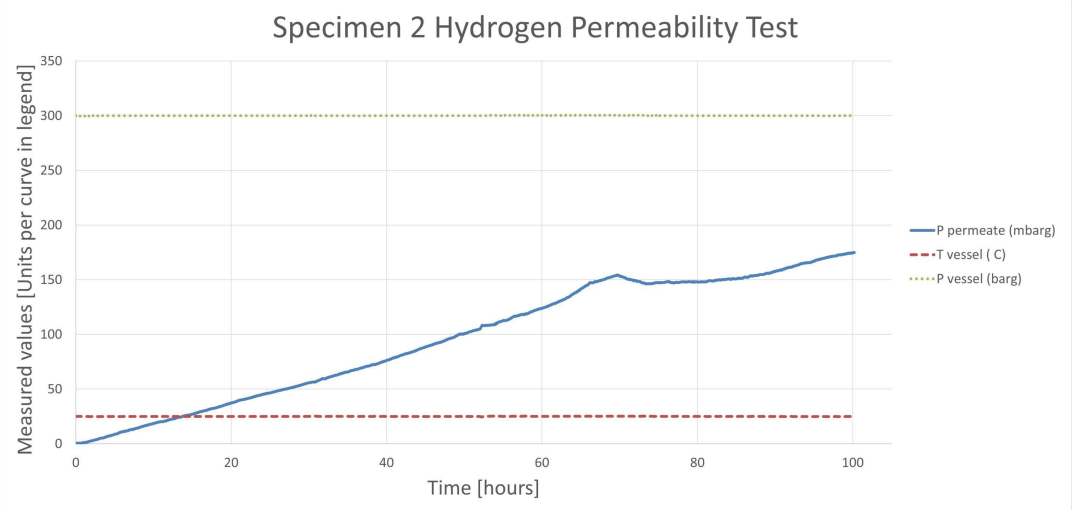

Figure A.8: Unprocessed Results of Gaseous Hydrogen Permeability Test of Specimen 2

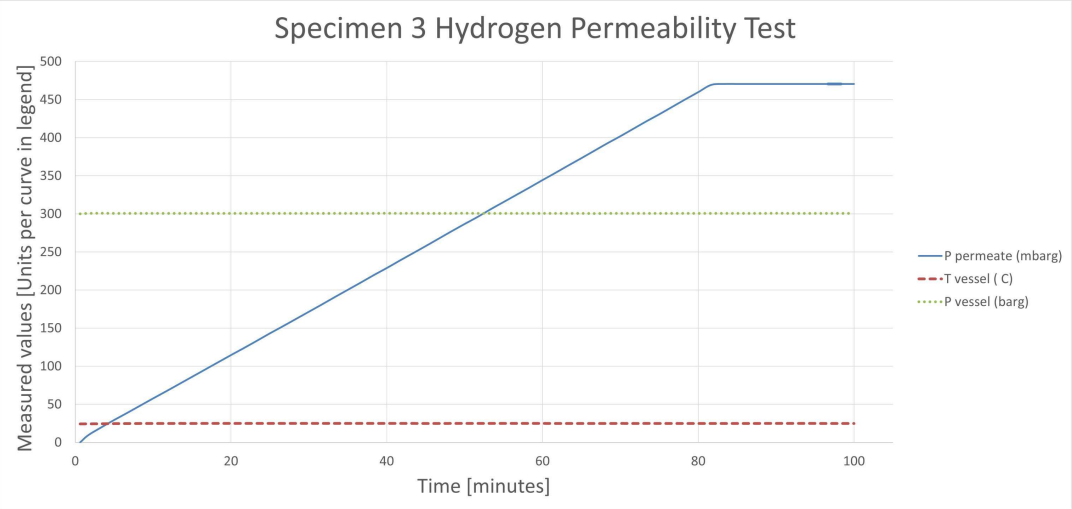

Figure A.9: Unprocessed Results of Gaseous Hydrogen Permeability Test of Specimen 3

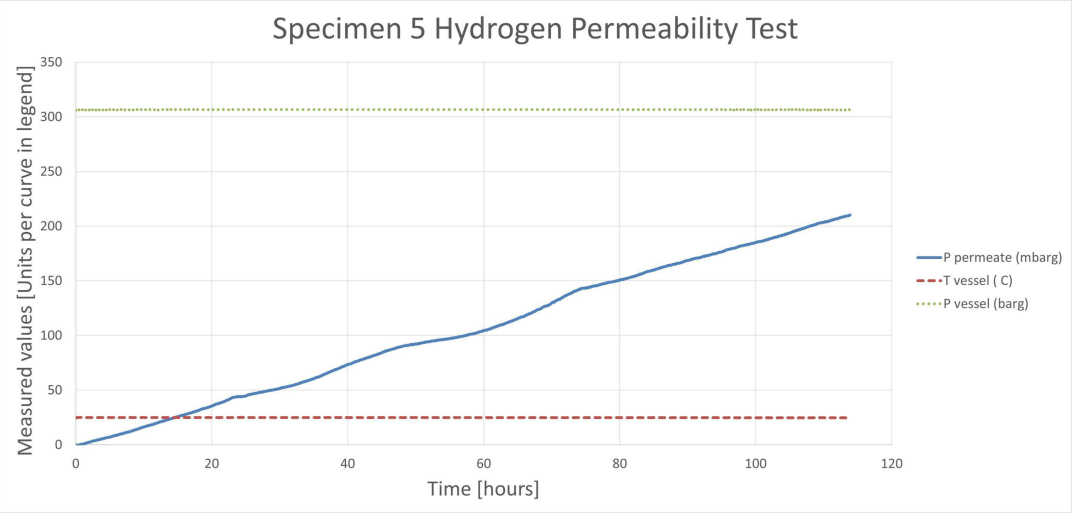

Figure A.10: Unprocessed Results of Gaseous Hydrogen Permeability Test of Specimen 5

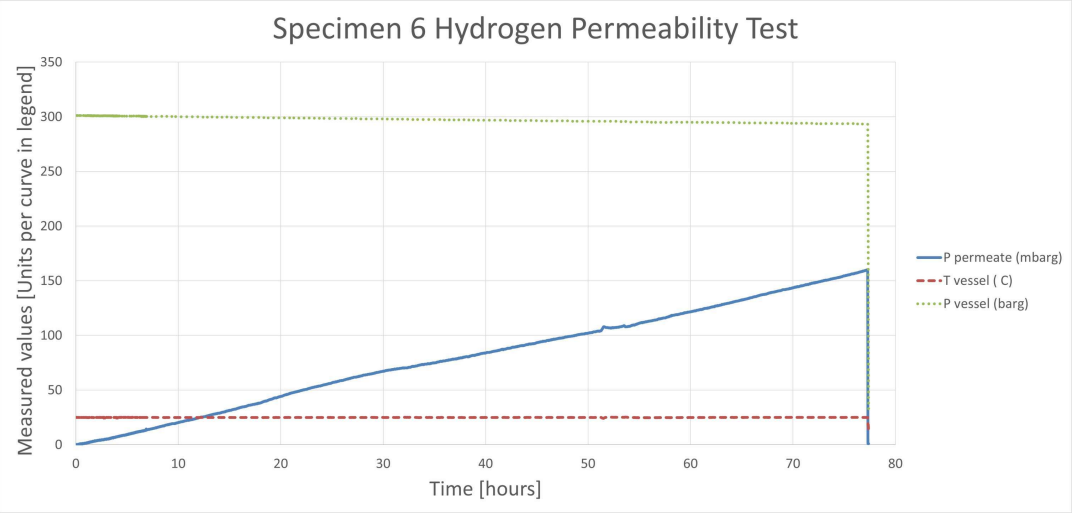

Figure A.11: Unprocessed Results of Gaseous Hydrogen Permeability Test of Specimen 6

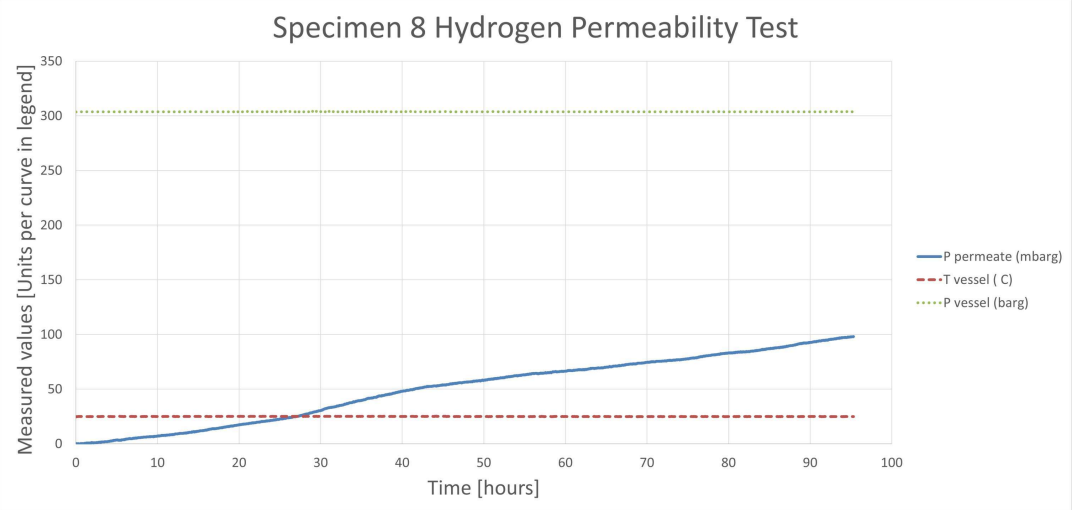

Figure A.12: Unprocessed Results of Gaseous Hydrogen Permeability Test of Specimen 8

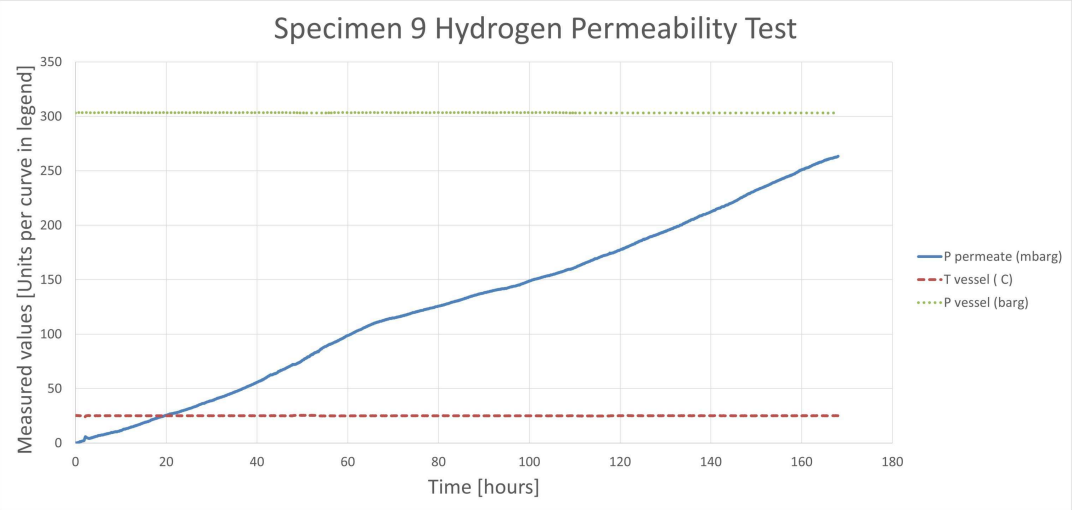

Figure A.13: Unprocessed Results of Gaseous Hydrogen Permeability Test of Specimen 9

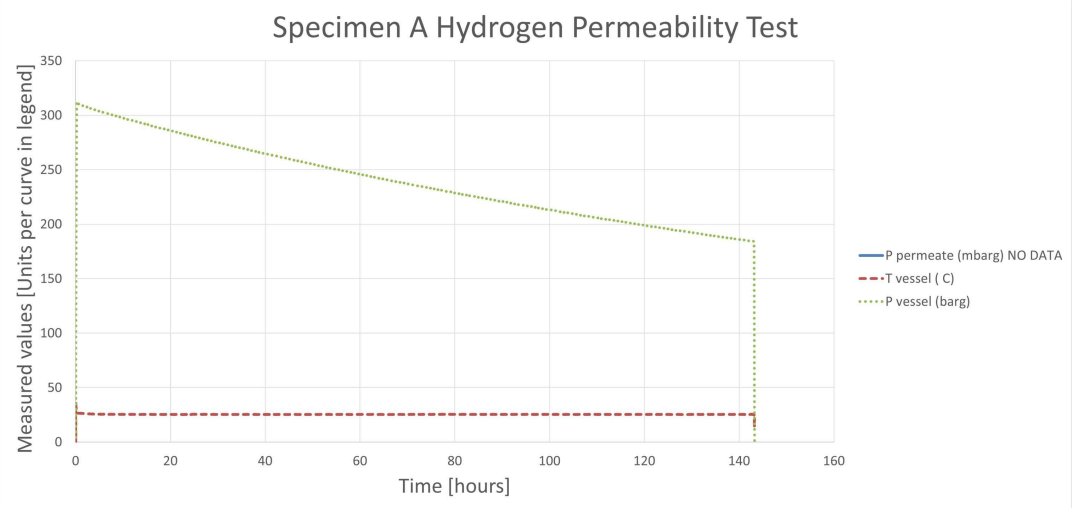

Figure A.14: Unprocessed Results of Gaseous Hydrogen Permeability Test of Specimen A. Note that due to the sharp drop in applied pressure (P vessel) due to leaking, no stable test could be performed and as such no data was recorded for permeate pressure.

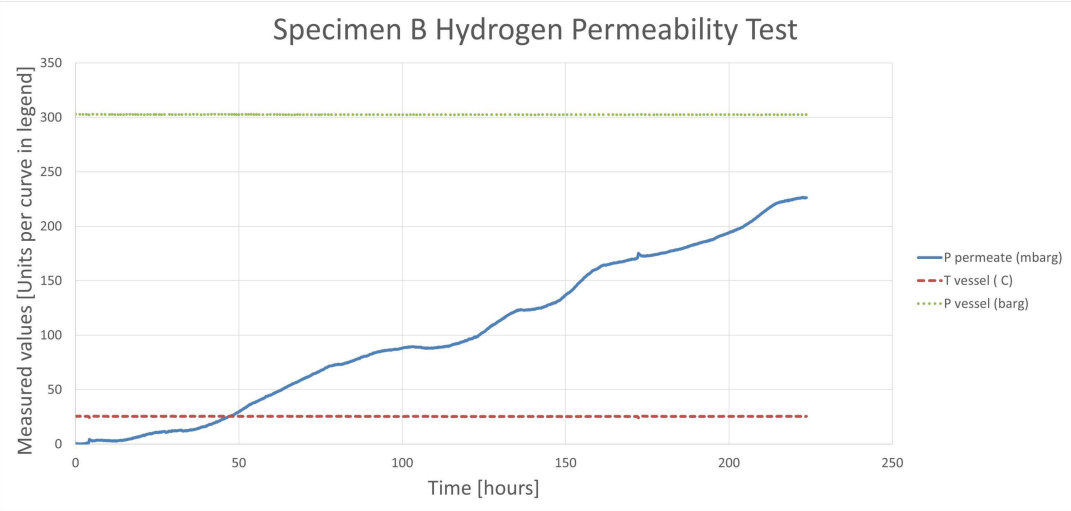

Figure A.15: Unprocessed Results of Gaseous Hydrogen Permeability Test of Specimen B

B

Extended data pressure testing

(a) R11

(b) R12

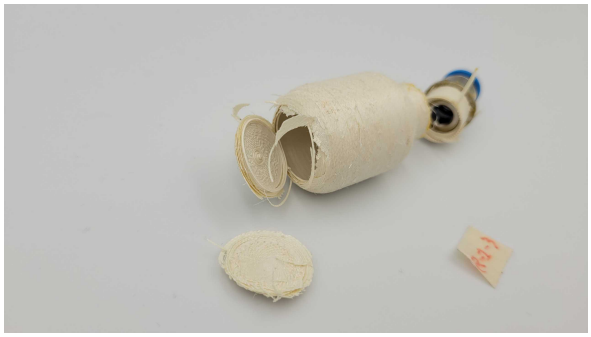

(c) R13

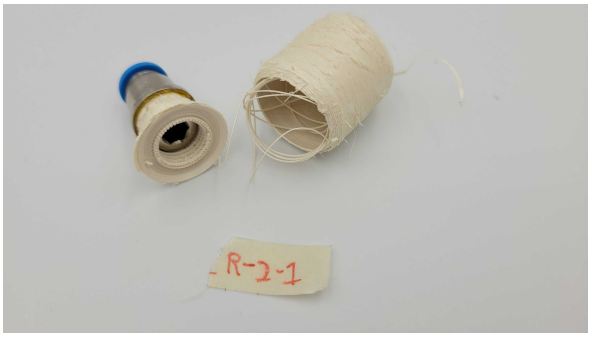

(d) R21

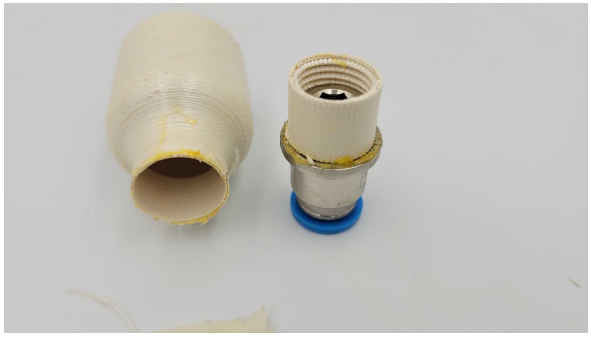

(e) R22

(f) R23

Figure B.1: Specimens after pressure testing

(a) R31

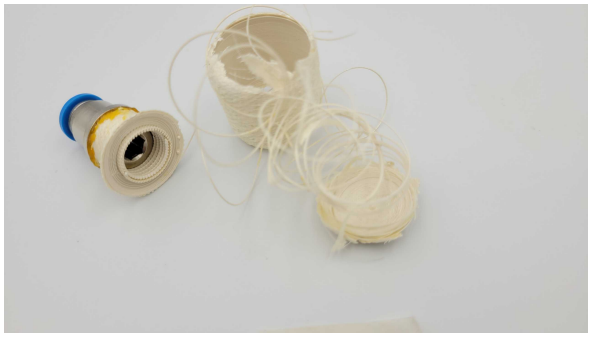

(b) R32

(c) R33

(d) R41

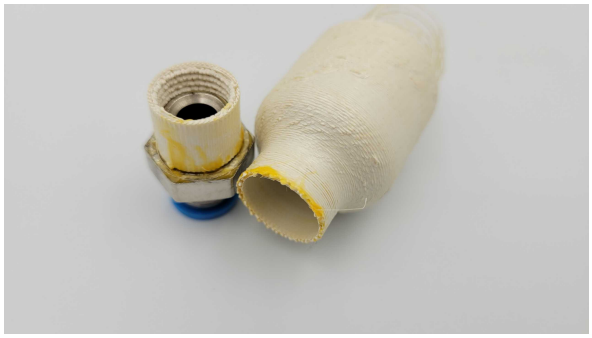

(e) R42

(f) R43

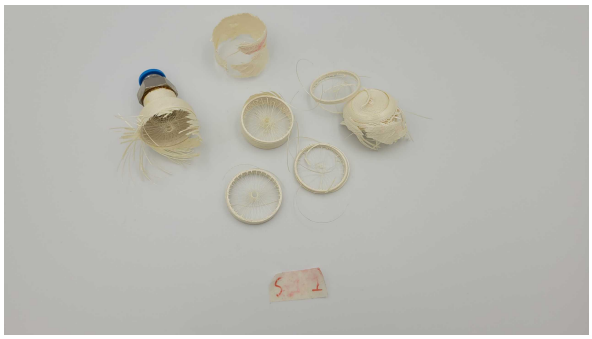

(g) S11

(h) S12

(i) S13

Figure B.2: Specimens after pressure testing